UNIVERSITY OF SOUTHAMPTON

FACULTY OF ENGINEERING AND THE ENVIRONMENT

Mechatronics Research Group

Design and Characterization of Nanocrystalline Graphite/Graphene based Environmental Sensors

by

Ling Ting Yang

Ph.D. Thesis

April 2019

Supervisors:

Assoc. Prof. Pu Suan Hui

Prof. Harold M. H. Chong

Prof. John W. McBride

UNIVERSITY OF SOUTHAMPTON

ABSTRACT

FACULTY OF ENGINEERING AND THE ENVIRONMENT

Ph.D. in Engineering and the Environment

Design and Characterization of Nanocrystalline Graphite/Graphene based Environmental Sensors

Ling Ting Yang

Carbon based thin films, such as graphene and graphite are promising materials for environmental sensing due to their chemical and mechanical stability, low-toxicity and selectivity towards certain environmental parameters. The scope of environmental sensing for this project will be limited to sensing of humidity and oxidizing gases for environmental monitoring applications. The most widely used methods to fabricate carbon based thin films rely on either physical transfer of CVD grown graphene films, or the deposition of graphene flakes onto substrates. However, such methods are less compatible with standard semi-conductor manufacturing processes. The variations caused by the film transfer (wrinkling, defects, different flake sizes etc) could cause variance in sensing performance which is not ideal. Therefore, we proposed the use of nanocrystalline graphite/graphene (NCG) films deposited with plasma-enhanced CVD (PECVD) onto large area substrate as a potential solution. The PECVD deposited NCG has high grain boundary concentrations, which makes it ideal for sensing applications as the sensing effect is thought to lie in the grain boundaries. At the boundaries, charge transport barrier is formed between two or more conductive nanocrystals. Interactions between elements in the environment may alter the charge transport barrier significantly, thus, causing a measurable change in the conductivity of the film.

The PECVD method for NCG deposition was studied with NCG deposited at different substrate temperature to obtain the Arrhenius deposition rate. Electrical characterization and surface characterization were done on each sample to study the effect of deposition temperature on the fabrication of the film. The deposition rate between wafer scale

deposition and sample scale deposition was studied, and it was found that on sample scale deposition, the deposition rate is slower than the wafer scale process due to the temperature difference introduced by a carrier wafer in the sample scale production process. The uniformity of the deposition was investigated using ellipsometry. AFM and FESEM images of the deposited films shown that the films consists of graphitic grains which are about 20-40 nm.

Here, the sensing behaviour of PECVD NCG towards different gas type is reported for the first time. The sensitivity of NCG towards 3 different gases, NO_2, NH_3, and CO was shown. The resistance of a strip (30 µm by 3000 µm, with thickness of 34 nm) decreases by 0.663% upon exposure to 10 ppm of NO_2, increases by 0.14% upon exposure to CO and increases by 0.1% upon exposure to NH_3. The desorption rate for the gas is observed to be slow. The characteristics of resistance change matches that of a p-type semiconducting gas sensor. Using Hall effect measurements, the majority carrier was found to be holes instead of electrons.

The humidity sensing performance of PECVD NCG was also demonstrated for the first time in this thesis. Upon exposure to humid air (95% relative humidity), the resistance of the sensor drops 3% (Sensor dimensions 10 µm by 20 mm meandered strip, with thickness of 200 nm). The effect of different geometrical designs on the sensing performance of the NCG humidity sensor was also investigated.

A potential application of this device is to incorporate such a sensor in a smart breath monitoring mask which monitors the wearer's respiration patterns continuously for applications such as health monitoring during physical activities or rest. Tests were carried out to investigate the effects of bodily fluids such as human perspiration and saliva on the reliability of the sensor. The sensor shows great recovery and virtually no degradation to its sensing performance after exposure to KCl solutions.

Table of Contents

List of Tables

List of Figures

DECLARATION OF AUTHORSHIP

I, Ling Ting Yang declare that this thesis and the work presented in it are my own and has been generated by me as the result of my own original research.

I confirm that:

1. This work was done wholly or mainly while in candidature for a research degree at this University;
2. Where any part of this thesis has previously been submitted for a degree or any other qualification at this University or any other institution, this has been clearly stated;
3. Where I have consulted the published work of others, this is always clearly attributed;
4. Where I have quoted from the work of others, the source is always given. Except for such quotations, this thesis is entirely my own work;
5. I have acknowledged all main sources of help;
6. Where the thesis is based on work done by myself jointly with others, I have made clear exactly what was done by others and what I have contributed myself;
7. Parts of this work have been published as:
    1. T. Y. Ling, S. H. Pu, H. M. H. Chong, J. W. McBride, "Design and characterization of nanocrystalline graphene/graphite based gas sensor", presented at University of Southampton Engineering Sciences Postgraduate Conference, Southampton, UK, 2016.
    2. T. Y. Ling, M. S. Shamsudin, S. M. Sultan, J. W. McBride, H. M. H Chong, S. H. Pu, "Fabrication and characterization of thin film nanocrystalline graphite for resistive sensing application", 43rd International Conference on Micro and Nano Engineering (MNE2017), Braga, Portugal, 2017.
    3. J. D. Reynolds, S. Rana, T.Y. Ling, L.A. Boodhoo, S. H. Pu, D. Pamunuwa, H.M.H. Chong, "Nanocrystalline graphite coatings for lateral silicon MEMS transistors", 43rd International Conference on Micro and Nano Engineering (MNE2017), Braga, Portugal, 2017.
    4. T.Y. Ling, S.J. Fishlock, M.S. Shamsudin, S.M. Sultan, H.M.H Chong, S.H. Pu, "Design and fabrication of a nanocrystalline graphite thin-film sensor for in situ ionic concentration monitoring", IEEE Sensors Conference 2017, Glasgow, UK, 2017.

5. T. Y. Ling, M. S. Shamsudin, S. M. Sultan, J. W. McBride, H. M. H Chong, S. H. Pu, “Design and characterization of nanocrystalline graphite-based humidity sensor”, presented at 8th International Conference on Nanoscience and Nanotechnology (NANO-SciTech), Selangor, Malaysia, 2017.
6. S. Rana, J.D. Reynolds, T.Y. Ling, M.S. Shamsudin, S.H. Pu, H.M.H. Chong, D. Pamunuwa “Nano-crystalline graphite for reliability improvement in MEM relay contacts,” Carbon, vol. 133, pp. 193–199, DOI:10.1016/J.CARBON.2018.03.011, 2018.
7. T.Y. Ling, S. H. Pu, S. J. Fishlock, Y. Han, J. D. Reynolds, J. W. McBride, H. M. H. Chong, “Sensing performance of Nanocrystalline Graphite Based Humidity Sensors”, IEEE Sensors Journal, DOI:10.1109/JSEN.2019.2905719, 2019.
8. T.Y. Ling, S.H. Pu, H.W. Lee, J.W. McBride, H.M.H Chong, “Sensing performance of nanocrystalline graphite humidity sensors for wearable breath monitoring applications”, IEEE International Conference on Sensors and Nanotechnology, Pulau Pinang, Malaysia, 2019.

Signed:

Date:

Acknowledgements

I would like to extend my deepest gratitude to my supervisors, Dr Pu Suan Hui, Prof. Harold Chong and Prof. John McBride for their kind guidance, help and support for the whole duration of my PhD. This work would not have been possible without their constant input and advice. Admittedly, without their patience and guidance, I would not have made it to where I am today. Special thanks to Dr Pu Suan Hui, who gave me full support and patience despite my slow progress. Thank you for giving me strong encouragements along the way! My gratitude also goes to Prof. Harold Chong who took great effort teaching me, and to get me acclimatized the UK. Thanks are due to my collaborators, Dr Suhana, Dr Sam Fishlock, Dr Lee Hing Wah and Mr Salleh Shamsudin, who contributed advice and resources that helped me in the completion of this work.

The support I received from my close friends, students and flatmates will not be forgotten. I would like to thank all the members of the UoSM IET OnCampus (Previously USMC IET OnCampus) and Southampton IET OnCampus, UoSM Robotics club, my roommates at ISV in Malaysia, and my flatmates in Glen Eyre, Southampton for coping with my somewhat eccentric lifestyle. Not to forget the staffs at UoSM for all the support and advices given!

I would also like to thank the members of Nanogroup (now Sustainable Electronic Technologies), Jamie, Liam, Rafidah, Azlin, Ioannis, Zhen Cheng, and Swee Zin who assisted me greatly during my time in the UK, in terms of fabrication, characterization and giving me general tips on research and report writing. Also, not to forget the ECS cleanroom staffs, Kian Kiang, Xiang Jun, Zondy, Richard and Sun Kai who gave me advice and helped in finalizing my fabrication process flow. Let's not forget my awesome office mates in the UK, Moisse, Daniel, Nikos, Harada, Dr Ma, Dr Du, YiChi, HeFei, FaYong, DaMing and FengYu, without whom the office would be a boring place!

Most of all, I would like to thank my parents and siblings for their whole-hearted support. I hope this work will inspire my brothers, Gabriel and Peter, to reach greater heights. Finally, I would like to thank Doreen for her patience, love, and being my strongest motivator to complete this work.

This work is sponsored by the MyBrain15 scholarship by the Ministry of Education of Malaysia, with support from the Faculty of Engineering and Environment. My access to the Nanofabrication facility is sponsored by the Southampton Nanofabrication Centre.

Definitions and Abbreviations

AFM – Atomic force microscope

CMOS – Complementary metal oxide semiconductor

CNT – Carbon nanotubes

CVD – Chemical vapour deposition

GC – Gas chromatography

IR – Infrared

MEMS – Microelectromechanical Systems

NC-Graphite – Nanocrystalline Graphite

NC-Graphene – Nanocrystalline Graphene

NEMS – Nanoelectromechanical Systems

PECVD – Plasma Enhanced Chemical Vapour Deposition

QCM – Quartz Crystal Microbalance

Redox – Reduction and Oxidation

RF – Radio frequency

SAW – Surface Acoustic Wave

SAED – Selected Area Electron Diffraction

SMU – Source measurement unit

SEM – Scanning Electron Microscope

TEM – Tunnelling electron microscope

UV – Ultraviolet

VOC – Volatile Organic Compound

Chapter 1: Introduction

1.1 Introduction

A sensor, in a broad sense, is a device which responds to a certain stimulus and generates an output. To a human, senses, which comprises of sight, smell, sound, touch, and taste comes naturally, humans are simply born with it. For electronic sensors, a certain sensing element is often needed to transduce the environmental variables into usable signals. Often, designing an accurate sensor could be challenging. Environmental sensors refer to a subset of the available electronic sensors. As its name suggests, environmental sensors are sensors which transduces environmental parameters into electronic signals in most cases. Recently, there is an increasing demand for gas sensors in various fields, such as industrial production, automotive industry, healthcare, and environmental monitoring. Due to the variations in measurement conditions, a variety of different gas sensors are required for different applications.

1.2 Background

There are many gases of interest in the field of environmental sensing. For example, to gauge the severity of air pollution, one can monitor the concentration of NO_2 in the atmosphere, to detect gas leakage, one measure the concentration of volatile organic compounds (VOCs), and to predict the weather, one could measure the humidity in the atmosphere. For this thesis, nitrogen dioxide (NO_2), carbon monoxide (CO), and ammonia (NH_3) and water vapour is chosen as the main target gases for sensing.

Nitrogen dioxide (NO_2) and nitrogen monoxide (NO) are pollutants which are produced because of fossil fuel combustion. NO_2 alone is a noxious gas that adversely affect the health of living organisms. It is also highly reactive in the presence of ultraviolet (UV) light from the sun, reacting with water vapour and hydrocarbons to form photochemical smog [1]. The European Commission has set the maximum average exposure limit for NO_2 to be 40 $\mu g/m^3$ over the period of a year, and an absolute maximum of 200 $\mu g/m^3$ in an hour [2]. Apart from its intrinsic harmful effects, NO_2 concentrations in the atmosphere correlates strongly to the presence of other pollutants, such as ozone and particulate matters [3], making a good indicator for air pollution monitoring. Figure 1 shows the severity of NO_2 pollution in the world. NO_2 comes mainly from man-made sources, causing various respiratory related health problems.

Figure 1 shows the NO_2 distribution obtained via satellite imagery. The Heat map correlates strongly with pollution hotspots.

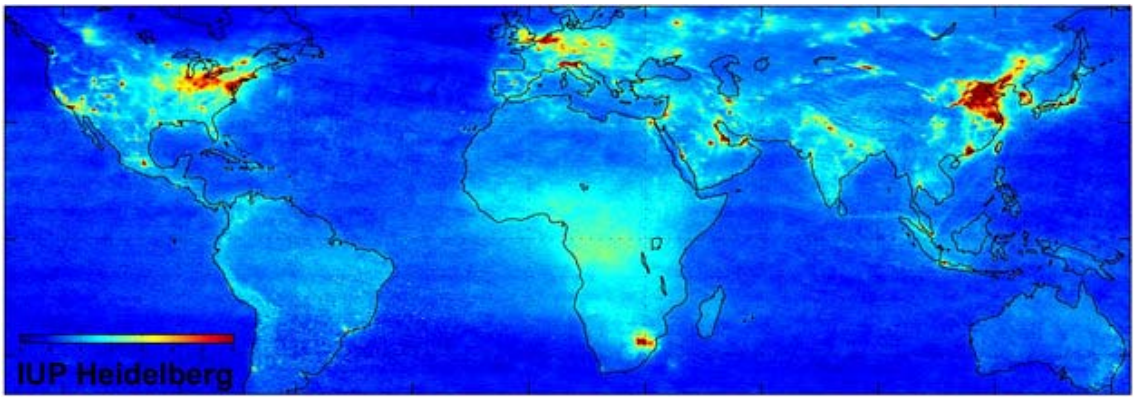

Figure 1: NO2 density heat map obtained via ENVISAT by the European Space Agency (ESA) [4]

Carbon monoxide (CO) and ammonia (NH_3) were also chosen because they could be used as indicators of indoor air quality. CO forms due to incomplete combustion, and is commonly produced in kitchen, or in coal fire heating in rural areas. Like NO_2, it is also harmful to the human health. When inhaled, CO combines with oxygen in the blood stream to form CO_2, preventing it from absorbing oxygen. Hence, prolonged exposure to CO is hazardous to the human life. On the other hand, NH_3 is also a common indoor pollutant. NH_3 is a pungent gas which creates discomfort and is hazardous if exposed long term. NH_3 is commonly released by volatilization of urea, which are excreted from the human body as urine. NH_3 can also be released by building materials or plant fertilizers containing urea. Both CO and NH_3 levels are important metric for indoor air quality and can be correlated to the level of comfort in the indoor environment.

However, previous work done on CNT based redox sensors has also shown notable respond towards humidity, with the relative humidity level of the environment severely affecting the sensitivity of CNT-based ammonia sensors [5]. The interfering effect of humidity on carbon based gas sensors, could in fact be exploited as a sensor for humidity in closed systems, where the concentrations of redox gasses are known to be low or constant [6]–[9]. In this work, both the effect of redox gases and humidity on NCG sensors will be explored.

1.3 Motivation

As technology progresses, the development of smaller, power-efficient sensors is preferred. Currently, metal oxide sensors are widely used in developing gas sensors due to the simplicity

of usage, large spectrum of detectable gases, low cost and flexibility in production. However, the use of metal oxides as sensing materials require the sensors to work at an elevated temperature. This is favourable in conditions where high-temperature is the norm, for example, NO_x monitoring in a combustion engine exhaust. In other applications, a suitable heater needs to be integrated into the design. Recently, conductive polymers are also investigated as gas sensors, as they have the potential to carry out detection at a much lower temperature. Nonetheless, polymers are known to suffer from degradation after prolonged usage.

Carbon exists in various physical forms, known as allotropes. These allotropes exhibit a high number of useful properties, such as high hardness (diamond), low coefficient of friction (graphite), chemical inertness, varying optical properties, and thermal conductivity. Since carbon is the basic building block of living organism, it is relatively harmless to the environment, with the added advantage of being biocompatible. In certain forms, carbon functions as an electrical conductor, while in others, it functions as an insulator. This property makes carbon a very interesting material for designing electronics. After the discovery of graphene by Geim and Novoselov won the Noble Prize in 2010, the research community started looking into the feasibility of incorporating graphene into electronics. One of the applications being investigated, is of course, environmental sensing.

Although graphene promises fantastic mechanical and chemical properties, the synthesis of large mono-crystalline graphene remains a challenge. Hence, CVD graphene was investigated as an alternative. In fact, work done on graphitic materials [10]–[12] have shown promise in the use of nanocrystalline carbon materials with high grain boundary concentrations in chemical sensing applications.

In Southampton, a catalyst-free technique for plasma-enhanced CVD graphene deposition on SiO_2 substrate was demonstrated by [13]. The work was further developed by [14] to deposit nanocrystalline graphite film for gas separation. Currently, no work has been done to evaluate the sensing characteristics of the catalysts-free, plasma enhanced CVD nanocrystalline graphene/graphite material for sensing application. In this study, the gas sensing properties of nanocrystalline graphene/graphite (NCG) was investigated.

This project aims to investigate the feasibility of utilizing nanocrystalline graphene/graphite (NCG), which is a hybrid form of carbon-based thin film, as a rugged sensor for environmental sensing in harsh environments. Like other solid state sensors, such as conductive polymers [15]–[20], metal oxide films [21]–[23], and other carbon based materials [5], [6], [24], [25], we

believe NCG has the potential to fill the gap as a robust sensor, with the potential to be integrated in smart wearable electronic devices.

1.4 Objectives

In this thesis the application of carbon thin films as an environmental sensor for sensing oxidizing gasses and humidity was studied. The goal of this research is to gauge the feasibility of using this material in a wearable sensor which would estimate the air quality based on NO_2 concentration, and the wearer's respiration patterns by monitoring the humidity change in each breath cycle. The main objectives of this research include the following:

1. To develop a repeatable fabrication method for NCG based sensor.
2. To explore and develop an understanding of the sensing mechanism of NCG under exposure to redox gases and different humidity levels.
3. To investigate the effect of the film characteristics on its sensitivity towards humidity levels and redox gases.

1.5 Structure of Thesis

First, a general review of current sensor technologies is presented in chapter 2. The different sensing mechanisms will be compared, and their strengths and weaknesses will be discussed. Next, various deposition methods for carbon-based nanomaterial will be presented. Also, a review on published literature concerning the use of nanocrystalline graphene/graphite is done to compare the deposition parameters and the resulting characteristics of the films. Then, the stability of carbon-based films towards environmental conditions and the effect of grain boundaries on carbon-based films is discussed.

In chapter 3, the fabrication and characterization process of the sensor is presented. Here, the general procedure for device fabrication, from design to characterization is discussed. Chapter 4, on the other hand, contains more in-depth explanation on the large area deposition of NCG film using the metal-free PECVD method developed by [13], and the improvements made. The Arrhenius rate of NCG deposition and the resulting film characteristics are also presented in this chapter.

Both chapters 5 and 6 discussed the experimental procedure and results obtained by the sensors. In chapter 5, the gas sensing performance of the sensor is discussed, while in chapter 6, the humidity sensing performance of the sensor is presented. Parts of chapter 6 were published separately as a journal paper in IEEE Sensors Journal.

Finally, the thesis is summarized in chapter 7 with suggestions for future work provided.

Chapter 2: Literature Review

In the following sections, a short review on currently available solid-state sensors is presented. The review will demonstrate how carbon-based thin films may potentially be superior to other solid-state films in the proposed application. Subsequently, a deeper review into other solid-state technologies and thin film materials used in humidity sensing and oxidizing gas sensing is presented. Finally, a short review on other non-solid-state sensors, such as MEMS and optical sensors are presented.

2.1 Sensing Mechanisms

2.1.1 Catalytic Sensors

Catalytic sensors are commonly used to monitor the concentration of combustible gases. A basic catalytic sensor consists of a temperature sensor, a solid catalyst, and a heater. This method is also known as the catalytic microcalorimetry, as it is designed to detect the change of temperature on the catalyst due to the exothermic reaction of combustible gases on the surface of the catalyst. Most of the sensors are designed with porous structure to maximize the surface area available for the catalytic reactions to take place. Figure 2 shows the typical structure of a catalytic gas sensor.

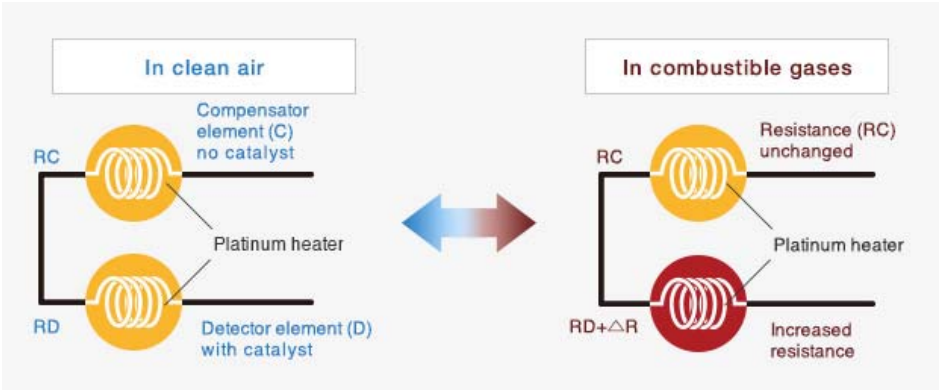

Figure 2: Operating principles of a catalytic type gas sensor [26]

The sensors are usually mounted in a Wheatstone bridge configuration for temperature compensation. In the Wheatstone bridge, both sensing element and the reference elements will have the same resistance in clean air. However, the reference element is shielded from the environment, and thus, will not change its resistance upon exposure to combustible gasses.

2.1.2 Charge transfer

The resistant of carbon-based films, such as NCG could be affected by molecules adsorbed on its surface. The change in resistance is believed to be a consequence of charge transfer between the adsorbed gas molecules and the sensing material. Charge transfer is the process where charge carriers from the analyte gas is transferred to the sensor material upon adsorption. In semiconducting sensors, such as metal oxide sensors, some carbon-based films and polymer films, electron transfer will increase the conductivity of n-type semiconducting sensors and decrease the conductivity of p-type semiconducting sensors. Figure 3 illustrates the sensing mechanism of typical a metal oxide sensor, which relies on charge transfer for sensing. Under normal circumstances, oxygen adsorbed on the surface of the metal grain creates a depletion region around its grain boundaries [27][28]. Upon interaction with an oxidizing or reducing gas, the surface stoichiometry of the grains will be changed, causing a change in the thickness of the space-charge region. The thinner space charge region around the grains would, in turn, modulate the inter-grain potential barriers, causing a variation in bulk resistivity.

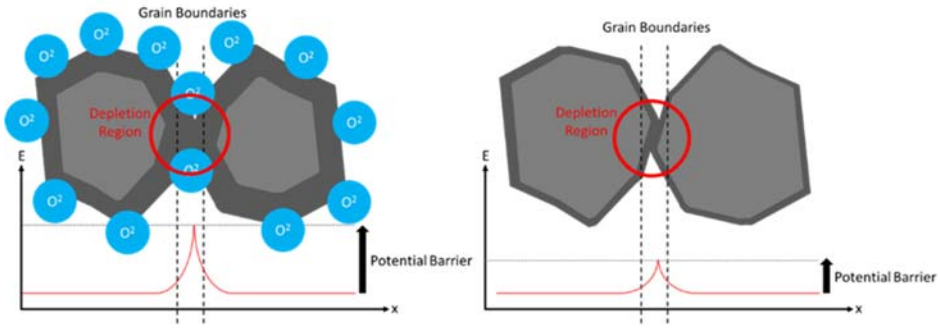

Figure 3: An Illustration of the effect of charge depletion caused by adsorbed oxygen molecules (blue circle) on the metal oxide grains (grey region)

In the case of adsorption of redox gases, one could assume that the reaction between adsorbed gases and surface oxygen is the main contributor to the observed change in conductivity. However, in the case of water adsorption, no such electron exchange is conceivable. Seiyama et al. [29] suspects that electrons trapped in surface defects, such as ionized oxygen vacancies, could play a significant role. A H_2O adsorption event on such defect area could potentially free the trapped electrons, resulting in enhanced carrier concentration, causing a change in the measured resistance.

2.1.3 Grotthuss Mechanism

In a polycrystalline film, such as in the case of NCG, adsorption of water molecules across the material's surface could cause a further reduction in resistivity. The Grotthuss mechanism, where charge is conducted by the adsorbed water via proton hopping, is believed to be the main sensing mechanism in carbon-based humidity sensors [9], [30]–[32]. The theory of protonic transfer in chains of hydrogen bonded water molecules was first proposed in 1804 by Theodor von Grotthuss (hence the namesake). The proton transfer process is thought to involve the exchange of covalent OH^- bonds with the hydrogen bonds of the neighbouring water molecules [33], [34]. During the transfer process, a more stable "Eigen" cation (H_3O^+) containing the extra proton forms a transition "Zundel" complex ($H_5O_2^+$) with a neighbouring water molecule, under the influence of an electric field gradient, before decaying back into H_2O, turning the neighbouring water molecule into the "Eigen" form, thus transmitting the proton to the next molecule [33][35] (See Figure 4).

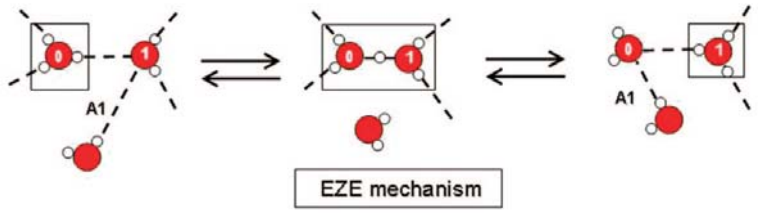

Figure 4: Eigen-Zundel-Eigen (EZE) protonic conduction [33][35]

Since energy is required to overcome the barriers in forming the Zundel complex, protonic conductivity can be likened to the mobility of charge carriers in solid state semiconductors. The mobility of the protonic conduction can be described as [33]:

$$\mu \propto \frac{1}{T}\, e^{-\frac{E_a}{k_b T}} \quad \text{------ Eq. 1}$$

where E_a is the activation energy for proton hopping, k_b is the Boltzmann's constant, and T is the temperature of the system. Typically, the value of E_a lies around 0.1 eV, which is the energy required to break a hydrogen bond in the second solvation shell [34]. Due to the amphoteric nature of water, the presence of Eigen complex is almost certain when water adsorbs onto the surface of a film from its gaseous (water vapour) state.

In mesoporous solid-state humidity sensors, adsorption of water molecules on the sensor's surface form conduction chains which reduces the overall resistivity of the films, hence, allowing the transduction of relative humidity into electrical signals [30]. In high relative humidity levels, the adsorbed water may form a continuous layer of water, thus, causing a

drastic drop in resistance. In multi-grain, multi-crystal, or nanocrystalline structures, such as those described by [32], [36], [37], the adsorbed water may form shunts between conductive grains, thus causing further decrease in the film's resistance.

2.2 State of The Art

When it comes to solid state electronic sensors, metal oxide is, no doubt, an industrial favourite. The fact that a metal oxide sensor is easy to design and implement [23] makes it attractive for commercialization and research. Whilst much research focuses on implementing new and improved metal oxide sensors [22], [38]–[44], some researchers prefer to use existing metal oxide technologies to implement smart sensing systems [45]–[47]. However, most metal oxide gas sensors require elevated temperatures, typically ranging from 200 ºC to 600 ºC [22], [40]–[44], [48]. Conductive polymer and carbon-based sensors are promising candidates for potential room temperature gas sensing application. In fact, work done on conductive polymer and carbon compound was even recognized by the Nobel Prize committee, awarding the Nobel Prize for Chemistry for 2000 to Heeger, MacDiarmid and Shirakawa for the discovery and synthesis of conductive polymer and the Nobel Prize for Physics in 2010 to Geim and Novoselov for ground-breaking work on graphene. Nonetheless, it is useful to note that, although the prize is awarded based on work done on the material *per se*, the award generated much interest in the research community to develop conductive polymer and carbon (notably graphene) based devices. In the following sub sections, we will analyse and discuss the proposed working principles of different solid-state gas sensors mentioned here.

2.2.1 Semiconducting Metal Oxide

In general, metal oxide sensors are used to detect oxidizing and reducing gases. As their name suggest, metal oxide sensors are formed using oxidized metals, and typically have polycrystalline structures. These sensors usually operate based on charge transfer (See section 2.1.2).

Tin oxide (SnO_2) is one of the most commonly used metal oxide sensor, with the ability to detect NO_2 at temperature as low as 150ºC [39]. One of the earliest monolithic SnO_2 sensor produced by a commercial CMOS foundry was reported by Suehle et. al. [22]. The gas sensor can detect H_2 and O_2 at 350 ºC using sputter deposited SnO_2, although the exact limit of detection was not stated. Bari et al. [39] report a Zn doped SnO_2 thin film sensor which operates at 150ºC with detection range of ~100ppm, and recovery times of about 3-10 seconds. Comini

et. al [40] report a SnO_2 nano-belt sensor which consists of SnO_2 nano-belts measuring, on average, 200 nm in width, running up to few millimetres in length. The nano-belts are synthesized by thermal evaporation of SnO_2 powder under controlled conditions in a tube furnace. The resulting sensor shows weak positive response to ethanol vapour and CO, but strong negative response to NO_2. The authors reported response to 0.5 ppm of NO_2 at 400ºC, but due to the strong sensitivity of the sensor towards NO_2, it could theoretically sense down to few ppb of NO_2 .

Zinc oxide (ZnO) is another popular material for gas sensing. It exhibits n-type semiconductor behaviour. In its early days, thick film ZnO sensors were used in thick film sensors for combustion control [49]. The thick films sensors could be fabricated easily by using film printing (gravure) technique and benefit greatly from the elevated temperature of its working environment. Kwon et. al.[49] shows that at temperature range of 500 ºC to 700 ºC, the resistance of the film increases upon exposure to O_2 and decreases when exposed to CO. Rao [50] on the other hand, reported that the sensitivity and selectivity of ZnO sensor towards ethanol vapour could be improved by introducing lanthanum oxide and palladium. The optimum sensing temperature lies in between 200 ºC and 250 ºC. However, the limit of detection for the sensor is only 1000 ppm. ZnO could also be used as an ammonia sensor with high sensitivity and selectivity. Nanto et. al. [51] reported one such sensor, using sputtered ZnO thin film as the sensing layer. The limit of detection is 1 ppm of ammonia at a working temperature of 350 ºC. Chou et. al. [41] worked on using ZnO nano particles instead. ZnO nano particles are deposited as a film across interdigitated electrodes as a potential gas sensor. Their devices show good NO_2 sensing responses at about 5ppm in NO_2/air mixture, at about 200 ºC. The limit of detection for the sensor is calculated to be around 10 ppb, which is much better that the earlier literature. Apart from thin and thick ZnO films, ZnO deposited in the form of nanowires could be used as a humidity sensor [52].

Tungsten oxide (WO_3) is another popular metal oxide material, notably due to its use in NO_2 sensors. WO_3 nanoplates, powders, nanowires, nanosheets, thin films and even nanocrystals have been used for NO_2 sensing with differing detection range and operating temperature [53]–[57]. Kim et. al. [54] reported a gas sensor using nanoplates prepared by acidification of $Na_2WO_4{:}2H_2O$. The sensor was manufactured using standard thick film processing techniques with Au electrodes. The sensor detects 0.5 – 5ppm of NO_2 at 300 ºC. Zhang et. al. worked on a similar sensor by spraying molten WO_3 particles on an interdigitated electrode sheet via atmospheric plasma spraying [57]. The coating process involves heating WO_3 powder with plasma and spraying the molten material onto the substrate. The resulting

film is porous, exhibiting response towards NO_2 in the range of 0-450 ppb at about 240 ºC. Qin et. al. [56] reported their work on tungsten nanowire bundles and nanosheets. Their sensor has a range between 1 to 20 ppm and has an optimum temperature of about 150 ºC. They noticed that nanowires showed a higher response value and faster response recovery. In another publication, Qin et. al. [58] reported a room temperature NO_2 sensor using Ti-added non-stoichiometric tungsten oxide ($W_{18}O_{49}$) nanowires. The addition of Ti via physical impregnation lowered the overall operating temperature to room temperature (25 ºC).

In this section, various work involving metal oxide sensors are compiled and compared. It is worth noting that most metal oxide sensors require elevated temperatures to work, apart from [58]. However, in that work, complicated chemical processes are required to synthesize the 1-dimensional $W_{18}O_{49}$ nanowires, and subsequently impregnate the wires with Ti additives. The lowest limit of detection for gasses among the recent literature is 10 ppb for NO_2, reported by Chou et. al [41]. NO_2 is also a popular choice for gas sensing as it exhibits high correlation with various pollutants in the atmosphere [59], and the fact that it is a strong oxidizer.

2.2.2 Conductive Polymers

Conductive polymers provide an alternative form of environmental sensing. They exhibit both electrical and optical changes upon exposure to oxidizing or reducing agents. In pure forms, the polymers are usually non-conductive, however, their conductivity could be significantly increased by doping. Doping with oxidizing and reducing agents allows conducting polymers to be used as gas sensors and pH sensors. An initially un-doped conductive polymer film could be used to sense reducing agents, while a doped film could be used to sense oxidizing agent. The most commonly used forms of conductive polymers are polyaniline (PAni), polypyrrole (PPy), and polythiophene (PTh).

PAni is one of the most popular because it is more environmentally stable, easily synthesized, and could react with chemical species at room temperature [60]. The main sensing mechanisms of PAni consists of protonation and redox reactions [61]. Virji et. al. [60] noted two additional sensing mechanism when PAni was used as nano-fibres, i.e. fibre swelling and conformational alignment. The key factor that affect the first two sensing mechanism is the ability of the polymer backbone of PAni to transport charge. Upon exposure to acidic substances, protonation of the nitrogen imine in the PAni chain occurs, causing it to switch from its normal non-conducting form to the conducting form. The process can be reversed by chemical species that takes away the hydrogen atom from the PAni chain, causing deprotonation to occur.

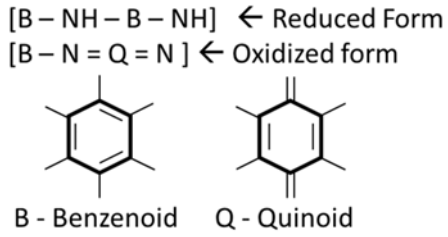

Figure 5: PAni monomer in reduced and oxidized form [62]

Reduction and oxidation of PAni is a similar process, upon exposure to oxidizing or reducing gasses, the conductivity of PAni is reduced or enhanced accordingly. The conductivity of the backbone is explained by the presence of delocalized electrons in the benzenoid rings in the PAni backbone (Refer to Figure 5). The ratio of benzenoid – quinoid content in the film determines the conductivity of the film. PAni also changes its colour upon switching between the two forms, being transparent or blue in its reduced form, and green in its oxidized form [63]. In PAni nano-fibres, geometrical factors, such as swelling of nanofibers and conformational alignment of fibres affects carrier hoping between PAni chains. Virji et. al. reported sensing of various chemicals, such as ammonia, hydrazine, chloroform and methanol, and classified them based on the sensing mechanisms, i.e. ammonia causes protonation to occur, hydrazine is sensed via redox reactions, chloroform is sensed via swelling, of nanofibers, while methanol causes the nanofiber to linearize [63].

Kukla et. al. [64] reports an ammonia sensor based on PAni films with an effective sensing range from 1- 2000 ppm at a temperature of 25 ^{o}C. They also noticed that the sensitivity of the sensor decreases as temperature was increased, which could be attributed to the fact that desorption is more favourable to adsorption in conducting polymer films. Sira et.al. [65] reported an NO_2 and NH_3 sensor using polyaniline nanofilms of about 9-20 nm in thickness. The sensor was fabricated by electro polymerizing the conductive polymer onto a silicon substrate with pre-fabricated gold electrodes. The resulting sensor shows high response (~3760 % change per ppm) to NO_2 and some response to NH_3 (~ 20% change per ppm).

Ppy can be synthesized with electrochemical deposition and Langmuir-Blodgett technique like PAni. It is a yellow coloured film in its usual form but turns blue or black when oxidized. Ppy is non-conductive in its reduced form and is conductive when oxidized. Chougule et. al. [66] studied the sensing behaviour of Ppy towards NH_3, C_2H_5OH and CH_3OH at room temperature. The film used in Chougule et. al.'s study was deposited using electrochemical deposition and exhibits linear response in the range of 5 to 100 ppm of ammonia (NH_3) at room temperature. Amongst the 3 gases tested, the film was selective towards ammonia. Carquigny

et. al. [15] reported a similar sensor with linear response in the range of 0 to 500 ppm of ammonia at room temperature. Su et. al. [67] reported a self-assembled Ppy film on polyester (PET) substrate to form flexible sensors. The resulting sensor exhibits acceptable linear response in the range of 5 to 50 ppm of ammonia.

Pth is another conductive polymer with the potential to be used as a room temperature gas sensor. Chang et. al. [18] demonstrated a method of printing Pth based gas sensor array for electronic nose applications using conventional inkjet printers. They compared their printed devices array with a spin-coated Pth device array, and obtain similar sensing results, albeit with degraded sensitivity. Liao et. al. [19], on the other hand, reported a rather unconventional method of detecting gas vapours using changes in Pth film thickness. The changes in thickness was measured using an in-situ X-ray reflectivity measurement. They observed an unambiguous increase in film thickness of about 4 – 6 Å upon exposure to analyte gasses. However, the increase of thickness does not correlate to the concentration nor the type of analyte used. The use of X-ray reflectivity severely limits the real-life application of this technology.

It is also helpful to note that hybrid sensors utilizing both conductive polymer/metal oxide and conductive polymer/carbon allotropes have been reported. For example, Kong et. al. [68] described a Pth/SnO_2 composite sensor which exhibits superior sensing performance at room temperature when compared to pure SnO_2. The sensor was able to detect NO_2 concentrations as low as 10ppm. Lin et. al. [31] reported a Ppy/graphene composite for humidity sensing. The composite humidity sensor has a sensing range of 12 – 90 % RH and have response/recovery time of about 15 to 20s.

2.3 Application of Carbon-Based sensors as oxidizing gas sensors

Atoms of carbon can bond together in different ways. These forms are known as the allotropes of carbon and have vastly different properties. Diamond, which is an allotrope of carbon, is extremely tough, transparent, and not electrically conductive. Graphite, on the other hand, is soft, black and electrically conductive. Of course, many other carbon-based materials, such as amorphous carbons, carbon nanotubes (CNT) and graphene have unique properties that lies between that of diamond and graphite.

Carbon based sensors have risen in popularity in the recent years, due to its potential as a room-temperature gas sensor. In the case of graphene-based sensors, the exceptional sensitivity at room temperature stems from the de-localized pi-electrons in the graphene lattice. In fact, due to the two-dimensional monolayer structure of graphene, it could detect gas at the molecular

level [69], despite needing extremely accurate read-out mechanism. Nonetheless, such sensors remain in the realms of labs, as large-scaled production of perfect, monocrystalline graphene remains a challenge. The "gold standard" for graphene quality in the scientific community is the mechanically exfoliated graphene (ME-Gr), which is a monolayer graphene obtained by mechanical exfoliation from highly ordered pyrolytic graphite (HOPG). Since then, other routes of graphene production have been explored, such as thermal decomposition of SiC, liquid phase exfoliation (LPE), and chemical vapour deposition (CVD). These techniques allow for large area deposition of monolayer, bilayer and multi-layer graphene thin films [70]–[72]. The trade-off, however, is the quality of the deposited films [73], [74]. Typically, graphene films deposited using mechanical exfoliation will have significantly lower defects when compared to the other methods. Even so, higher defect density does not necessarily translate to disadvantages in the field of gas sensing. From a theoretical point of view, defects and impurities in graphene films has been reviewed extensively [75], and has been studied experimentally [12], [76].

Graphene consists of mainly sp^2 bonded carbon atoms, arranged in a hexagonal lattice. Graphene has an ambipolar electric field effect due to its thin, one atom-thick structure [77]. Also, due to graphene's unique electronic band, where the valence and conduction bands touch at a dirac point in k-space (instead of overlapping, like most semi-metal, or having a small gap, like most semiconductors), charge carriers in graphene mimics relativistic particles instead of quantum particles [77]. Graphene has conjugated pi electrons like CNT as well, which contributes to its high conductivity. Due to graphene's unique charge transport properties, Sun et. al. were able to make a room temperature CO_2 sensor that can detect individual molecular physisorption. The sensor utilizes doubly clamped bilayer graphene on Ti/Au electrodes [78]. Due to the extremely high carrier mobility present in pristine bilayer graphene, any adsorption event will create an adsorption-induced Coulomb impurity scattering. These events are detected as step-like changes to the conductivity of the graphene sheet. However, the yield of such devices is low, as it requires mechanical exfoliation of graphene on the substrate or using a transfer process where graphene is transferred from growth substrate to the device substrate, and subsequently patterning the contact electrodes onto the exfoliated or transferred sheet using electron beam lithography. These processes could potentially introduce wrinkles, tears and other defects on the graphene film.

In fact, using pristine graphene as a gas sensor for normal, environmental monitoring might not be feasible, due to its less-than favourable adsorption mechanics [79][80]. In a defected graphene lattice, dangling bonds makes the crystal more reactive, and could subsequently be

doped with foreign atoms, causing a change in its electronic properties via doping [80]. Liu et. al. [81] presented a review on the possible chemical doping of graphene. In the review, NO_2 is classified as a p-type dopant, while NH_3 is been classified as an n-type dopant. Ko et. al. [82] demonstrated that graphene could adsorb and desorb NO_2 at room temperature by measuring the resistance across a single layer graphene obtained by mechanical exfoliation of Highly Ordered Pyrolytic Graphite (HOPG). Their sensor showed good response when 100 ppm of NO_2 was introduced. However, the adsorption rate was higher than desorption, prompting the group to investigate the use of UV-LEDs to facilitate desorption. Chung et. al. [83] enhanced the chemical sensing properties of graphene by introducing oxygen functional groups on a CVD deposited graphene film. The functional group was introduced onto the graphene film by ozone treatment. The resulting sensor has an estimated LOD of 1.3 ppb based on the signal to noise ratio, which is an improvement over prior work. Interestingly, in Chung et. al.'s [83] work, when temperature was increased, the sensor response decreased, but the recovery time of the sensor was improved. This could mean that a controlled heater may be used to expedite desorption, while keeping the sensor in room temperature during each sensing cycle. Pearce et. al. [84] reported an epitaxially grown graphene NO_2 sensor. Single layer and multilayer graphene sheets were grown on a SiC substrate by annealing the SiC at 2000 ^oC under 1 atm of Ar. Pearce et. al. note that the graphene exhibits n-type conductivity initially but undergoes n – p transition upon exposure to higher NO_2 concentrations. The initial n-type doping may be attributed to charge transfer from the SiC substrate, while prolonged exposure to NO_2 might cause the n – p transition due to surface transfer doping. An interesting study to note, is Ricciardella et. al's recent work, which investigated the sensing characteristics of ME-Gr, LPE-Gr and CVD-Gr [12]. The study reveals that although ME-Gr has superior response characteristics, CVD-Gr provides a comparable result, despite having slower response time, while LPE-Gr has the worst performance. In that sense, CVD-Gr provides a promising route to large-scaled production of gas sensors.

On the other hand, CNTs are also studied extensively by various research groups due to their interesting properties and ease of synthesis following its discovery by Ijima [85]. Due to its long tubular structure, CNT has an extremely high surface area to volume ratio, which translates to higher surface area for gaseous interaction when exposed to the atmosphere. The conjugated pi electrons on the outer surface of the CNT means that carrier transport is possible parallel to the CNT growth direction, and along any CNTs which are in contact with each other. Upon interaction with oxidizing or reducing gasses, the conductance of CNT films could be significantly affected [86][87]. Kong et. al. [86] demonstrates this by exposing single-walled

carbon nanotubes (SWCNT) to NO_2 and NH_3. The exposed CNTs increased in conductance upon exposure to NO_2 but decreases in conductance when exposed to NH_3. The study strongly suggests the presence of substantial hole as carriers in the nanotube, and thus, when exposed to NH_3 which depletes the holes in the SWCNTs, the conductance was greatly reduced. This is consistent with Tans et. al.'s [88] observation, where a positive gate voltage on a semiconducting CNT FET causes hole depletion in the CNT, creating a region with lower conductance. Sayago et. al. [87] also reported a CNT based gas sensor using mainly multi walled CNT (MWCNT). In their experiment, Sayago et. al. tested NO_2, H_2, toluene, and octane, but only NO_2 produced a response in the sensor. The reported limit of detection (LOD) of the sensor is 0.1 ppm of NO_2 at temperatures ranging from 100 ºC to 250 ºC for sensor recovery. It is helpful to note that Sayago et. al. did not grow the MWCNTs directly on their substrate, but instead, sprayed commercially purchased MWCNT onto the substrate after ultrasonically dispersing the MWCNT in ethanol. Han et. al. [89][6] reported a SWCNT based NH_3 and humidity sensors implemented on cellulose paper. The low-cost sensor utilizes similar chemiresistor approach, where the change in resistivity of the CNT strips are monitored to detect the presence of NH_3 or water vapour. The LOD for the CNT paper based NH_3 sensor is 5 ppm, while the detection range for the humidity sensor is between 0 to 75% RH, after which the condensed water affects the mechanical integrity of the paper substrate.

NCG have some interesting electronic and mechanical properties which distinguishes it from normal Highly Ordered Pyrolytic Graphite (HOPG) and graphene. One such difference is the high grain boundary (GB) concentration in nanocrystalline graphite films which leads to degradation in its electron transport properties. However, work done by several research groups [10], [90]–[92] shows that the grain boundaries could potentially act as sensing hotspots for adsorption. Chandrasekar reported the fabrication of thermally decomposed NC-graphite films from SiC substrates at 2000 ºC, and investigated its sensitivity towards polar molecules [10]. Interestingly, the fabrication method was similar to those reported by Pearce et. al. [84], however, the term 'graphite' was used, possibly due to the number of layers deposited. The resulting film shows sensitivity to NO_2 concentrations as low as 600 ppb when measured using scanning Kelvin probe microscope. Serra et. al. [91] show another type of nanographite film, fabricated by self-assembly of nanographite particles on a substrate from a carbon nano colloid fluid using chemical bath deposition. This results in a graphite film of 200 nm with nanocrystals size ranging from 20 nm to 120 nm (modal size: ~80 nm). The resulting film shows response to 1 ppm of NO_2 at temperatures as low as 20 ºC, but the optimum temperature of the film was shown to be at about 100 ºC. At higher temperatures, the sensitivity degrades. Lu et. al. [92]

demonstrated another method which, like Serra et al.'s method, involves water based deposition. The difference, however, is that Lu et. al. first oxidize the graphite nanoparticles to form graphite oxide, which is subsequently dispersed into graphene oxide upon suspension in water. The separation occurs due to the hydrophilic nature of the oxide bond formed on both sides of the graphene's basal planes. The graphene oxide solution is then spread across a substrate with gold interdigitated electrodes, dried, and thermally treated to form NC-graphene. The reduced graphene oxide sensor is shown to detect NO_2 at concentration as low as 2 ppm. Schmidt et. al. [13] demonstrated a plasma enhanced chemical vapour deposition (PECVD) method for large area NC- graphene deposition at temperature ranging from 750ºC to 900ºC. The film could be patterned using O_2 reactive ion etching. Fishlock et. al. [93] provided additional insights to the gas permeance of the PECVD NCG using membranes. Work has not yet been done to evaluate the chemical sensing properties of the PECVD NCG film reported by [13].

A large portion of the carbon materials related literature reported p-type like behaviour for carbon based sensors, ranging from CNT, surface-treated graphene and NC-graphite [10], [83], [86], [87], [91], [92]. One possible explanation is that oxygen adsorption upon exposure to the environment might play a role in generating holes in the carbon thin films [94]. Careful investigation needs to be done to re-evaluate the constituents of the carbon films deposited to verify the actual mechanism contributing to this behaviour.

2.4 Application of Carbon-Based Materials as Humidity Sensors

In this section, a review of humidity sensors will be presented. As the one of the main aims of this project is to demonstrate the response of NCG towards humidity, this section provides a benchmark for our project to compare against existing work. It is believed that the dominant sensing mechanism behind NCG is the Grotthuss mechanism as opposed to charge transfer, which is evident in some graphene or CNT based sensors.

As NCG is a p-type semiconducting like material, its resistance would increase when exposed to water vapour if charge transport is the main sensing mechanism. In a p-type material, like those reported in [6], the majority carriers are holes, instead of electrons. Upon adsorption, electrons from the water molecule would fill these holes, thus, reducing the carrier concentration, causing a reduction of conductivity. A separate study done by [95] on single layer graphene shown that when charge transfer occurs, the resistance increases upon exposure to water vapour. Their experimental results were supported by charge density simulation, showing that water molecules adsorbed on the graphene surface creates a region with higher electron density, allowing the electrons to recombine with current carrying holes.

However, even though the Hall effect characterization in NCG (See Section 4.4) shows p-type like semiconducting behaviour, the NCG film experiences a reduction of resistance upon exposure to higher relative humidity. This is similar to work done on CVD graphene films reported by [96] and graphene oxide films reported by [97]. In both works, the decrease in resistance is attributed to the Grotthuss mechanism.

In Table 1, a summary of work done in carbon-based humidity sensors is shown. It is observed that various methods result in sensitivity values which varies by degrees of magnitudes. The sensors reported were characterized in humidity-controlled environments like the ones used in this work. The short-hand “%RH” refers to the percentage of relative humidity used for characterization.

Table 1: Comparison with other published works on carbon-based humidity sensors

Sensing Material	Method of detection	Figure of Merit S = (ΔR/R/%RH)×100% unless stated otherwise	Tested Range	Ref
Graphene oxide and amine modified graphene oxide	Capacitance and conductance	S_{max} = 9.67% (capacitance) S_{max} = 0.0463% (conductance)	5% RH – 95% RH	[32]
CVD Graphene	Resistance	S = 0.31%	1% RH – 96% RH	[95]
Multilayer graphene (MLG) and Graphene	Resistance	S = 0.1% - 0.17% Response is non-linear, reported as [(ΔR/Rx100%)/%RH] × 100% = 10% Work shows various strip with alternating resistance change to explore the origins of such change.	15% RH – 80% RH	[8]
Bilayer Graphene	Resistance	S = 0.181% Sensitivity calculated in terms of current instead of resistance	35% RH – 98% RH	[96]
Black phosphorus (BP) – Graphene hybrid	Resistance	S = 0.62% (as fabricated) S < 0.14% (after 4 weeks)	15% RH – 70% RH	[98]
Carbon nanotube on cellulose paper	Resistance	S = 6% Sensitivity calculated in terms of conductance	10% RH – 70% RH After 70% sensor loses linearity due to degradation of cellulose paper.	[6]
Poly-diallyldimethylammoniumchloride (PDDA)/Reduced graphene oxide (RGO)	Resistance	S = 8.69–37.43%	11% RH - 97% RH	[9]
Multiwall carbon nanotube/polyimide composite	Resistance	S = 0.0047%	10% RH – 95% RH	[99]
Nanocrystalline Graphite (This work)	Resistance	S = 0.0334%	15% RH – 85% RH	[100]

PDDA/RGO films reported by [9] appears to have a much higher sensitivity in orders of magnitude when compared to the others. However, the author believed that the sensing capabilities of the PDDA/RGO films is attributed to the swelling of the film rather than ionic conduction across the film. The resistance of the PDDA/RGO film increases due to the increased interlayer distance experienced by the hybrid layer upon adsorption of water vapour. The graphene oxide and amine-modified graphene oxide sensors reported by [32] also provide a much higher sensitivity, however, the author also noted the higher hysteresis induced errors in sensors with higher sensitivity. This was attributed to the ionization of surface functional groups, especially in the positively charged amine group during measurement. Carbon nanotube

is also highly sensitive, the surface area of the tubes allows the adsorbed molecules to transfer its charge to the nanotubes. Since the carbon nanotubes behaves like a p-type semiconductor, the resistance of the film increases upon water adsorption [6]. However, at higher relative humidity, the proximity of the nanotubes will induce condensation, creating an ionic conduction path which, in turn, reduces the resistance, causing the carbon nanotube sensors to lose linearity at higher humidity reading. In the case of [6], the substrate choice also plays a role in limiting the operational humidity of the sensor. Despite having a smaller sensing magnitude, NCG has a much simpler fabrication process when compared to other forms of graphene sensors, such as those reported by [95], [96] and [98].

2.5 Other Air Quality Sensor Technologies

2.5.1 Gravimetric Sensors

2.5.1.1 NEMS/MEMS Gas Sensors

NEMS and MEMS sensors are robust. They can be used to sense force, acceleration, and even chemical concentration. Due to the small mass of the resonator, adsorption of any gaseous molecules on the NEMS or MEMS device will cause a shift in resonant frequency [101]. When used in sensing concentration of gasses in environment, however, NEMS and MEMS sensors lack intrinsic selectivity. This means that NEMS and MEMS sensors require an additional functionalization layer to work as a gas sensor. In certain cases, such as in a multi-gas detection system, low selectivity is preferred, as chemical separation will be handled by an additional component, such as filters or gas chromatography columns. Gas chromatography column uses a long narrow tube filled with a certain chemical (known as stationary phase) to separate a mixture of gasses (mobile phase) into their separate components. The stationary phase is chosen based on the type of gas that needs to be separated. As different gas travels with different speed down the gas chromatography column, they reach the sensor at different time.

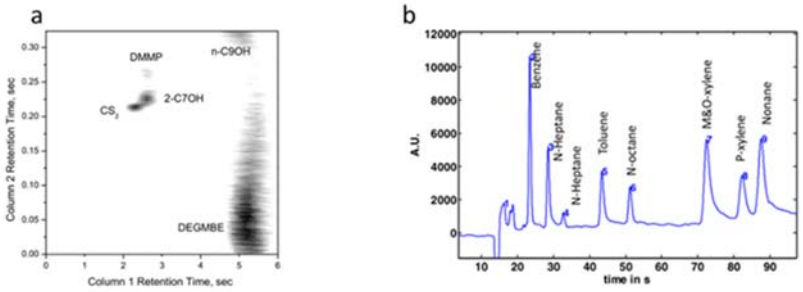

Figure 6: (a) 2D density plot on retention time on polar and non-polar GC-columns (b) 1D Frequency shift to gas flow time plot on single channel GC-column [102]

One such system was reported by [102], where NEMS array resonators were used to detect mass concentration of gas flowing through the gas chromatography column (Refer to Figure 6). In their work, cantilevers of dimension 300 nm (width) by 160 nm (thick) of various length were investigated. The length of the devices is not reported, but the authors note that they are a few microns long. Piezo resistive gauges were used for signal transduction. The NEMS cantilevers are actuated between 30-70 MHz. Gasses are detected based on shifts in resonant frequency experienced by the cantilever. With this set-up, the group has managed to detect BTEX (Benzene, Toluene, Ethylbenzene and Xylene) mixtures from 500 ppb to 50 ppb (shown

in Figure 6(b). A similar technology was reported by [103], using 2 different gas chromatography columns, one with polar stationary phase, and the other with a non-polar stationary phase. This results in a 2-dimensional dataset, shown in Figure 6(a) which could be used to identify the gas species passing through the column more accurately.

Humidity sensors based entirely on MEMS technology are rare. This could probably be attributed to the fact that most polymer sensor and ceramic sensor have a much better performance at sensing humidity than MEMS sensors. Lee et. al. [104] report a MEMS based humidity sensor which uses polyimide coated nitride/silicon cantilever as the humidity transducer. Upon exposure to water vapour, the polyimide film expands, causing an internal tensile stress which bends the cantilever. A gold coated metal plate placed at the end of the cantilever and the substrate was used as electrodes to carry out capacitive measurement. As the cantilever bends, the distance between the gold plate and the substrate is reduced, causing a change in capacitance which can be measured. Unlike earlier literature, the cantilever was not actuated, by external force. Many literature reports MEMS based humidity sensors are actually hybrid sensors or integrated sensors which includes humidity sensing functions. For example, Lazarus et. al. [105] report a CMOS-MEMS capacitive humidity sensor, however, the sensing mechanism does not involve mechanical actuation of the device. Rather, the device was released to increase the exposed surface of the polymer film used in sensing. Some other papers, such as [106] and [107] reported MEMS humidity sensors, but the sensing mechanism is not based on MEMS. These sensors, however, are fabricated on suspended plates released using MEMS fabrication techniques.

2.5.1.2 Surface Acoustic Wave (SAW) Devices

Surface acoustic wave (SAW) devices and thin film bulk acoustic resonators (FBAR) are mechanical sensors which operates based on change in acoustic wave properties as it interacts with the environment. Typically, an SAW sensor consists of a functional layer, which attracts and binds with the target gas, and a piezoelectric transducer, which converts the electrical input signal into mechanical acoustic waves. The input and output electrodes are usually placed at the opposite ends of the sensing film. Wang et. al.'s [108] work is a classic demonstration of a SAW based gravimetric gas sensor. They used a 300 MHz SAW sensor coated with molecularly imprinted polymer (MIP) for dimethyl methyl phosphonate (DMMP) detection. The sensitivity of this sensor is about 18.9 Hz/ppm for DMMP concentrations from 1-100 mg/m^3 (0.20 – 20 ppm). Lee et. al. [109] demonstrated the sensing of environmental pollutants with a SAW SO_2 sensor. The SAW sensor is actuated with a $LiTaO_3$ piezoelectric crystal, operated at 54 MHz.

The functional layer is made up of CdS thin film, which selectively adsorbs and desorbs SO_2. The sensor can measure down to 200 ppb of SO_2 at a substrate temperature of 160 ºC under laboratory condition.

FBAR sensors are essentially miniaturized version of the SAW sensor. Its smaller dimension allows it to resonate at a higher frequency, i.e. GHz range compared to MHz range for SAW. Zhang et. al. [110] reported a highly sensitive gas sensor which responds to water and ethanol vapour. The resulting FBAR experiences a shift of 11 kHz per percentage of change in relative humidity and 1.55 kHz change per ppm of ethanol. Chen et. al. [111] demonstrated the use of a functional layer to improve selectivity of an FBAR nerve gas sensor. In this project, a CU^{2+}/11-mercaptoundecanoic acid bilayer is used as a functional layer to trap DMMP. Both [110] and [111] rely on mass loading effect to shift the resonant frequency of the FBAR sensor for read-out. FBAR and SAW sensors are thus suitable for sensing heavier organic molecules via mass loading effect.

Most gravimetric sensors target heavier gas, with particulate matters being the heaviest, to organic molecules, such as BTEX, DMMP and ethanol. Humidity sensing can also be carried out with gravimetric sensors, although in most cases, it is not directly measured as a frequency shift, but instead, relying on functional layers, such as the expansion on polymer films. Lighter and chemically active gasses are often sensed with solid state sensors, such as the metal oxide sensors discussed in the previous section.

2.5.2 Optical Sensors

Detection of environmental variables using light is not really a new field. The use of light in atmospheric gas detection ranges from detecting the concentration of specific gas with higher degree of accuracy, to detecting the types of gas present in a given mixture. Most optical environmental sensors rely on either UV absorption spectra or IR absorption spectra of gasses for detection. The UV absorption spectra generally relates to the electronic transition of the gasses, while IR spectrum relates to the molecular vibration and rotation of the gasses [112]. In each case, different chemical species exhibits different absorption lines for UV and IR, hence forming a ‘fingerprint’ which can be used to determine the chemical species. The use of optical based method allows satellites to estimate the concentration of gaseous components in the atmosphere, such as those reported by [4]. The spectral lines of known atmospheric gasses can be found easily on the HITRAN [113] database, making it easy for researchers to map results to known chemical species. Edner et. al. [114] described a differential optical absorption spectroscopy system (DOAS) using strong illumination sources and detectors attached on roof

tops. Such techniques are usually costly and large-scaled, hence, will be excluded from this report.

Somesfalean et. al. [115] monitor NO_2 emissions using long path absorption spectroscopy, with a detection limit of 5 ppb, which is better than most solid state sensors. The set up was also tested on actual road condition to verify its function in a real-life situation. However, the sensor requires a high-power laser diode, operated at about 635 nm in order to work. The path length (distance needed to be travelled by the light ray across the gas sample) for this sensor is 160 m. For a smaller set up, Xu et. al. [116] utilized a broad spectrum blue LED, with a peak emission at 465nm. The path length of the setup is significantly shorter than Somesfalean et al's work, but the sensor has a LOD at 3ppm, which is 3 orders of magnitude worse, when compared to the latter's work. Gao et. al. [117] report a similar sensing scheme, with external modulation diode laser instead of LEDs. The diode lasers are operated at 435 nm, and the absorption signal was extracted after passing the light through a 20 cm gas cell. The limit of detection is found to be 5 ppm. Langridge et. al. [118], reported the use of a broadband absorption spectrometer with LEDs for gas detection. The absorption wavelength of water vapour was approximately 652 nm, with a detection range like that of a commercial hygrometer. The exact LOD for water vapour was not reported. However, it's useful to note that the response time for this sensor is approximately 10 seconds, making it slower than most solid-state sensors.

The main sensing principles of these sensors remains the same: i.e. exploiting the absorption spectra of chemicals to determine the concentration of the said chemical in a sample. The same technique could be utilized for both gas and liquid sensing, with spectrometers and spectrofluorometers. The main advantages of optical based sensing scheme are accuracy, ability to carry out remote sensing, and ease of experimental set up with existing technologies. However, it is a challenge to miniaturize optical sensors, as the signal to noise ratio degrades when scaled down.

2.6 Graphitic carbon film deposition technologies

Here, a general overview of different technologies used to grow or produce graphene and graphite films are presented. Methods to produce low-defect single crystal graphene are not presented here as it is not related to the main work presented in this thesis. Most of the graphitic films presented in this section are polycrystalline carbon films with grain boundaries and various crystallite sizes. This section is divided into two main topics: films which are grown directly onto the substrate, and films which are drop-casted onto the substrate.

2.6.1 Direct growth method

2.6.1.1 PECVD deposition

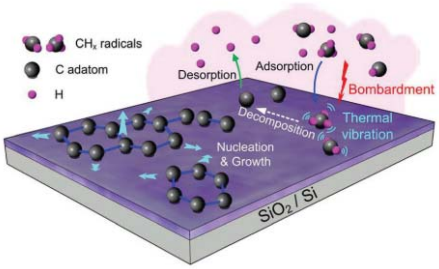

Figure 7: Schematic representation of NCG deposition in PECVD process adapted from [119]

In general, the deposition of NCG through PECVD requires a carbon precursor which can be decomposed into solid carbon and an exhaust gas (See Figure 7). In our case, methane is used as it decomposes readily into carbon and hydrogen gas in the reaction shown below:

$$CH_4\,(g) \leftrightarrow C(s) + 2H_2\,(g) \text{------ Eq. 2}$$

By varying the process conditions, such as the pressure, substrate temperatures, gas flow rate and RF power, the structure of the film can be varied, creating different allotropes of carbon. To deposit NC-graphite, it is imperative to select the right conditions, such that the carbon film deposited will fall under the graphitic domain. An abundance of sp^3 bonds in the film will degrade the electrical conductivity of the grains, as the number of available pi-electrons for conduction will be reduced.

The deposition of NC-graphite is governed by 5 main processes:

1. Dissociation
2. Adsorption
3. Surface diffusion
4. Nucleation (Bond forming)
5. Desorption

In a plasma enhanced deposition environment, the dissociation energy contributed by substrate surface temperature is less, due to the use of plasma that aids in dissociating the carbon precursor. Energy from surface temperature due to heating does contribute to nucleation and desorption of hydrocarbon molecules.

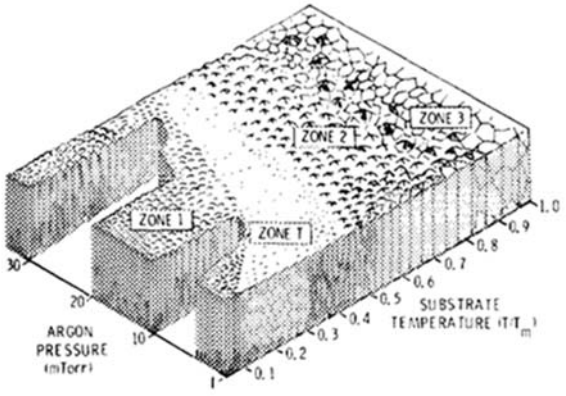

Figure 8: Microstructure zone model for thin film growth under different substrate temperature and gas pressure, from [120]

Thornton [121] describes the microstructure of thin films deposited at low substrate temperature to material melting temperature ratio as being columnar with voids (Zone 1 and Zone T in Figure 8). The paper discussed the effects of different substrate temperature on vapour deposited metallurgical layers. Although the paper focuses on surface irregularities and growth structure of metals, the underlying principle is also applicable to carbon film growth.

One of the advantages of plasma enhanced deposition is that it allows deposition to be carried out at lower substrate temperatures. However, this means that the adatoms (adsorbed atoms) possess less energy to move about on the substrate. As a result, each adsorbed atom effectively ‘sticks’ to the substrate. Subsequent atoms arriving from the plasma flux will then

stick to these atoms in an energetically favourable position, forming a columnar structure shown in Zone 1 and Zone T.

Zone 1 and Zone T are distinguished by the size of the columns. Zone 1 has thicker columnar structures which may be monocrystalline or polycrystalline in nature, while Zone T forms fibrous columns with higher density of voids in between them. Optically, however, Zone T appears to be more reflective and smoother, due to the small crystallite size which is unresolvable with a conventional optical based measurement. Thornton observed higher resistivity in Zone 1 and Zone T thin films, a few orders of magnitude greater than the film's material resistivity. This could be attributed to the presence of oxygen bonds which may have formed due to atmospheric exposure.

2.6.1.2 Thermal decomposition of SiC

Thermal decomposition of SiC has been studied extensively recently due to its potential in growing high quality single and few-layer graphene. The growth method was first proposed by Suemitsu et al in 2009 [122]. Their process was simple: growing a layer of SiC on silicon substrate via gas source molecular beam epitaxy, and subsequently anneal the SiC film in UHV at 1300ºC to obtain epitaxial graphene via thermal decomposition (Shown in Figure 9).

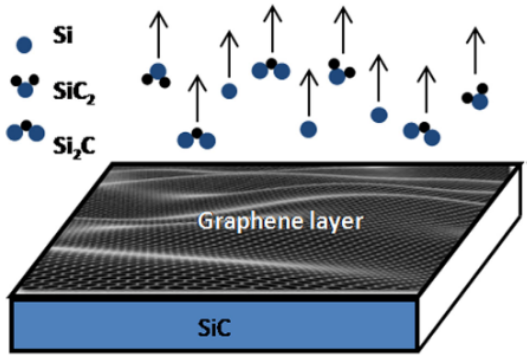

Figure 9: Illustration on the sublimation of silicon atom from SiC surface during thermal decomposition (adapted from [72]).

Thermal decomposition of SiC happens due to the thermal destruction of the surface SiC layers when subjected to high temperatures (900 ºC-2000 ºC) [10], [55], [72], [122], [123]. At such temperatures, the Si atom in the SiC film gains enough energy to sublimate from the SiC substrate in the UHV condition. The thermal decomposition of SiC can be summarized in the equations below [123]:

$$SiC(s) \leftrightarrow Si(g) + \mathrm{C}\,(s)\text{------ Eq. 3}$$

$$2\mathrm{SiC(s)} \leftrightarrow \mathrm{Si_2}C\mathrm{(g)} + C(s)\text{------ Eq. 4}$$

$$2\mathrm{SiC(s)} \leftrightarrow 2\mathrm{SiC(g)} + C(s)\text{------ Eq. 5}$$

The carbon atoms left behind then rearrange to form a uniform graphitic film on the top of the SiC substrate. Further annealing provides the carbon atoms with energy to go into the nucleation stage, which is analogous to the nucleation stage of PECVD deposition. In some cases H_2 is added to etch the remaining Si and amorphous carbon on the surface of the substrate [124]. Mynbaeva et al. studied the formation of different structure due to thermal decomposition of silicon carbide. Their study found that the first layer of carbon formed on the SiC – Graphite interface is electrically inactive, forming a buffer layer. This is due to the lack of pi-electrons in the film. The pi-electrons of the first layer is thought to be partly bound to the substrate atoms by covalent bonds. Multi-layered carbon films formed above the buffer layer conduct electricity with properties like that of CVD graphene films. Goler et al. [125] did Raman characterization on the buffer layer, and reported that no graphene related bands were observed. However, STM scans from the buffer layer shows periodicity and honeycomb structure like that of a graphene layer. This reinforces the believe that the buffer layer is indeed structurally identical to a single layer graphene, but due to strong covalent interaction with the underlying substrate atoms, its properties were altered.

Chandrashekar at al. [10] has demonstrated the use of this method to obtain a uniform film of nanocrystalline graphite for gas sensing applications. Their thin film was grown by solid state thermal decomposition of SiC at 2000 ^{o}C. The film was then etched to form a 0.5cm x 0.5cm samples, with Ti-Au contacts deposited at the corners. The film exhibits a decrease in resistance when exposed to NO_2 under a two terminal resistance measurement. This leads Chandrashekar et al. to believe that the nanocrystalline graphite films grown via thermal decomposition of SiC exhibits “p-type like” semiconducting properties. However, Hall effect measurements on the thin film did not yield any clear result on the carrier type of the film. In this work, we will also attempt to find the majority carrier of NCG using Hall effect measurements. The details of the measurement will be presented in Chapter 4.

2.6.1.3 Molecular Beam Epitaxy

Molecular beam epitaxy (MBE) is widely used for growing semiconductor films of high quality due to its slow and controllable deposition rate. However, it requires extremely high vacuum pressure which usually translates to a much higher cost. In a MBE system, the evaporated atoms or molecules do not interact much with each other due to the extremely low

pressure in the chamber. This results in bigger mean free path of the gas molecules, which sometimes exceeds the distance between the source and the target, hence the name “molecular beam”.

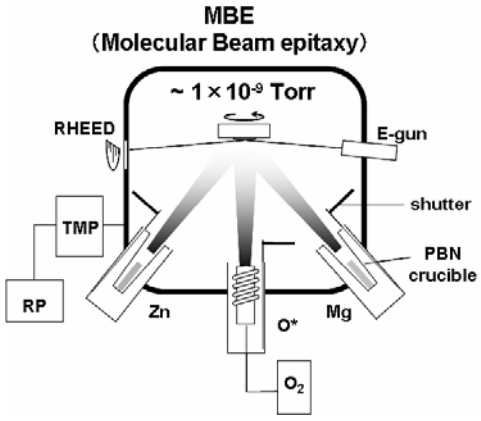

Figure 10: Schematic diagram of a MBE system (adapted from [126])

Figure 10 shows the set-up of a plasma assisted MBE system. Note that the set-up comes with a reflection high energy electron diffraction system (RHEED) which can be used to characterize the surface layer of the deposited film. The chamber is evacuated with a two-stage system, with a turbo molecular pump (TMP) and a rotary pump (RP). The set-up shown in Figure 10 is used for the deposition of $Mg_xZn_{1-x}O$ films. The source metals are introduced in a pyrolytic boron nitride (PBN) crucible, and oxygen is introduced as a plasma through an electromagnetic coil. However, MBE deposition is constrained by the availability of substrate. In order for MBE to be performed successfully, there must be template matching between the film and the underlying substrate.

Jerng et al. [127] demonstrated the use of MBE to deposit nanocrystalline graphite films. The films were deposited onto sapphire substrates of various cutting directions via MBE growth using solid carbon as source material. The nanocrystalline graphite films deposited exhibits similar Raman peaks as the ones deposited by PECVD [13] and Si-C decomposition [10]. The author theorized that the presence of nanocrystalline clusters of graphite instead of a single crystalline structure was due to the interaction between carbon and oxygen at the sapphire-graphite interface. The random variation of such interaction will explain why the formation of nanocrystals are independent of the cutting direction of the sapphire substrate.

Schumann et al. [128] investigated the growth of nanocrystalline graphene on the SiC buffer layer. The buffer layer is isomorphic to graphene, hence can be used as a template for graphene growth on SiC substrates. The author observes planar growth of graphene crystals in the

nanocrystalline film. The crystals are aligned in-plane with the buffer layer-SiC (0001) substrate irrespective of the thickness of the film.

Lippert et al. [129] demonstrated the growth of graphene islands on biotite mica substrates. The islands grown are in the micrometer regime. The deposited graphene has low defect density, resulting in high crystallinity, evident from the Raman spectrum of the resultant film. The high crystallinity of the graphene islands and its relatively large size makes it a useful candidate for making graphene-based transistors.

From a brief survey of literature, it is evident that MBE could be used for graphene and graphite deposition onto various substrates such as sapphire [127], silicon carbide [122][128], mica [130] and other dielectric substrates, such as and silicon dioxide[131]. However, due to the high cost of MBE equipment, PECVD is more desirable for lower cost implementation of NCG deposition.

2.6.2 Drop casted films

2.6.2.1 Reduced graphene oxide films

Due to the popularity of graphene in the research community, researchers are looking at more ways to produce graphene at a larger scale. Chemical exfoliation is one of the most popular methods as it allows for the mass production of graphene flakes. The flakes are often termed reduced graphene oxide (r-GO) as the production process involves oxidizing the graphite into graphite oxide, and subsequently exfoliating the graphite oxide into graphene oxide before reducing it to remove the oxygen functional groups. After reduction, the graphene oxide flakes become graphene flakes. However, when processed in bulk, the graphene oxide may not be reduced completely, with some oxygen functionals still present. Hence, the term “reduced graphene oxide” is usually used instead of “graphene”.

The chemical exfoliation of graphite is carried out by introducing functional layers between layers of graphite. This creates a graphite intercalation compound with a much larger interlayer spacing than pure graphite. As a result, the graphite crystal swells, making it easier to exfoliate and isolate the layers. The most common method involves introducing oxygen functional groups to the graphite layer using the Hummers Offeman method [132]. The Hummers Offeman method allows for the synthesis of high quality graphitic oxides using graphite powder as a source.

By modifying the original Hummers Offeman method, researchers are able to produce graphene oxide by dispersing the graphite oxide layers through ultrasonic sonication [133]. The resulting flakes can then be reduced back to its graphitic form using strong acids. The reduced graphene oxide would generally have higher defect density, like that of nanocrystalline graphite. Some researchers have incorporated graphene oxide as sensors without reducing the flakes to graphene [32].

While drop-casted films are easier to prepare, it is often hard to control the variance across each batch of devices fabricated. Also, drop-casted films are usually mechanically fragile when compared to PECVD deposited films.

2.7 Concluding Statement

The demand for smaller, and better environmental sensors is rising due to the industrial demand in producing smarter devices. This has led to a numerous research on novel materials for gas sensing. Traditionally, the research centres around metal oxide sensors, with researchers looking into lowering operating temperature and increasing sensitivity by changing either the size (e.g. metal oxide nanowires), or by changing the chemistry (e.g. using additives/nanoparticles). On the other end of the spectrum, researchers are also looking into emerging materials, such as conductive polymers and carbon-based films. Research on conductive polymers and carbon-based films are usually focused on the material preparation and characterization.

Carbon-based films show great promise as a material for gas and humidity sensing. Graphene is extremely suitable for gas sensing due to its 2D structure. Under controlled condition, graphene could sense up to a single molecular adsorption event [78]. However, it is difficult to obtain free-standing graphene for device fabrication.

NCG films, on the other hand, are relatively easier to fabricate. Despite its lower sensitivity relative to graphene, NCG exhibits good response when exposed to different humidity levels, showing good potential in practical application in normal household or health monitoring scenario. Previously reported materials, such as conductive polymers and carbon nanotubes, are fragile, and might not be able to withstand harsher environments. NCG, on the other hand, is relatively stable and robust to work with. As NCG is a relatively new material, there is a knowledge gap in the sensing mechanism of NCG, and the overall understanding of NCG as a sensing material.

Chapter 3: Fabrication and Characterization Techniques

In this chapter, the main fabrication techniques involved in fabricating the gas sensors and test structures are presented. The variations involved for sensors with different application will be detailed in later chapters. Subsequently, the experimental methods used in the succeeding chapters are also presented in detail. The results of each of the experimental steps will be discussed in depth in their respective chapters.

3.1 Overview of fabrication process

Resistive strips of various geometrical dimensions were designed and fabricated throughout the course of this project. The key fabrication steps are summarized in Figure 11.

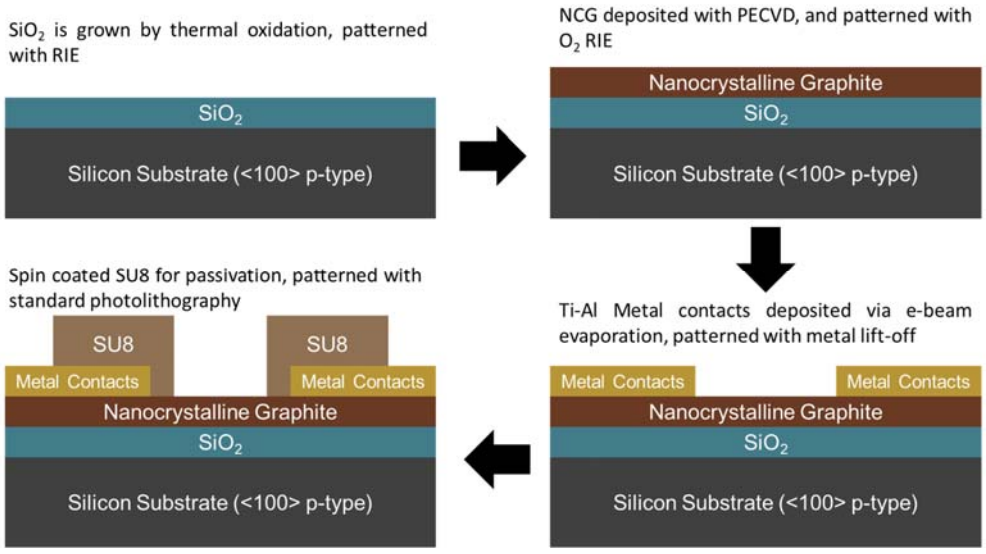

Figure 11: A brief illustration of the key fabrication steps

Each of the fabrication steps will only be presented once for the sake of brevity.

3.2 Wafer cleaning and preparation

The wafers used for this project are 6-inch, p-type, <100> Silicon wafers. The wafers are first immersed in a solution of NH_4OH:H_2O_2:H_2O at the ratio of 1:1:5 (RCA1) for 10 minutes, followed by a 10 minutes quick dump rinse to remove organic particles on the surface. After that, the wafer is immersed in HCl: H_2O_2:H_2O at a ratio of 1:1:6 (RCA2) for 10 minutes, followed by another H_2O rinse (Weir clean) clean to remove any metal contaminants. Finally,

the wafers are dipped in a solution of HF:H_2O at a ratio of 1:20 for 10 seconds, followed by a weir clean to remove any native oxides on the wafer.

The wafers are marked with a laser marker to identify the target thickness of the deposited wafer. Each chip on the wafer is also marked with an identification code based on their location on the wafer. This allows the actual thickness of NC-graphite on each chip to be determined, instead of using the average thickness of the whole wafer.

3.3 SiO2 growth via thermal oxidization

A thermal oxide layer of about 450 nm in target thickness was grown on the silicon wafers to act as a charge isolation layer between the substrate and the NC- graphite layer. The oxide layer was grown by wet oxidation using *Tempress 150mm Furnace* at 1000 ºC for 1 hour and 45 minutes to obtain a dense oxide layer. The overall oxide growth time was calculated with the Deal-Grove model, as shown:

$$t = \frac{X^2 - X_0^2}{B} + \frac{X - X_o}{\frac{B}{A}} \quad \text{------ Eq. 6}$$

where X_o is the initial oxide thickness (in μm) and X is the desired oxide thickness (in μm). B and B/A are called the quadratic reaction rate and the linear reaction rate, respectively. Both B and B/A can be represented in Arrhenius form as shown:

$$B = B_o e^{\frac{E_1}{k_b T}} \quad \text{------ Eq. 7}$$

$$\frac{B}{A} = \left(\frac{B_o}{A_o}\right) e^{\frac{E_2}{k_b T}} \quad \text{------ Eq. 8}$$

The values for B_o, B_o/A_o, E_1, and E_2 are taken from [134]:

$$B_o = 3.86 \times 10^2$$

$$\frac{B_o}{A_o} = 0.96 \times 10^8$$

$$E_1 = 0.78\ eV \quad E_2 = 2.05\ eV$$

Taking T = 1000ºC, the time needed to form 450 nm is calculated to be approximately 1 hour and 45 minutes. The wafers are oxidized at the calculated time, and the resulting film thickness was measured with a *J. A. Woolham M2000* ellipsometer. The average thickness of the deposited oxide layer is 462 nm, giving an error of about 2.6%, which is acceptable.

The deposited SiO2 layer was patterned and etched using standard photolithography. Each subsequent layer of the device is aligned to this layer. First, S1813 positive photoresist is spin coated onto the wafer at 3000 rpm for 30 seconds to form a 2-micron resist layer and baked for 60 seconds at 115ºC to cure the resist. The pattern was then transferred to the photoresist using a dark field photomask on the LE03 EVG 620TB mask aligner. After UV exposure, the wafer is then developed with MF-319 for 45 seconds and rinsed with DI water.

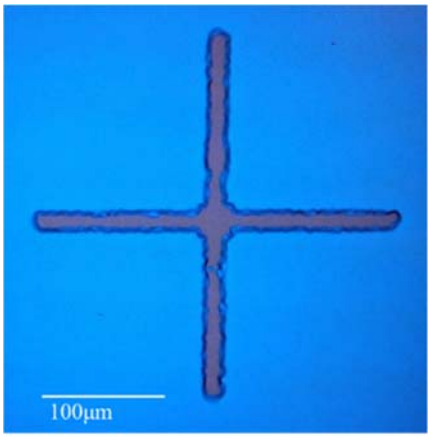

Figure 12: 'Mouse bites' observed in the developed wafer

Some ‘mouse bites’ were observed in the developed wafers. However, since the SiO_2 layer is used for electrical insulation, and the etched pattern plays no important role in the function of the device, the fabrication was continued. The presence of mouse bites in the developed film shows that the photoresist was under exposed. Hence, the exposure time was increased in the subsequent process to avoid the same problem.

The developed wafer is etched using Reactive Ion Etching (RIE) on an *Oxford Instruments RIE 80+* under CF_4 for 15 minutes to etch 300 nm of SiO2. The photoresist is then stripped with a plasma asher and cleaned with acetone and IPA.

3.4 NCG deposition

3.4.1 PECVD Deposition of NCG and characterization methods

NCG deposition for the final devices was carried out using PECVD at 850 ºC under a constant flow of methane (CH_4) and hydrogen (H_2) in an *Oxford Instruments Nanofab 1000 Agile* PECVD Chamber at 100 W RF power. Methane is used as the carbon source for the deposition, and hydrogen is added as a diluent to control the deposition rate and as an etchant to remove amorphous carbon [135]. The growth of the NCG film follows the general

mechanism for CVD growth, i.e. Dissociation, Adsorption, Surface diffusion, Nucleation, and Desorption [136]. A separate set of experiment ran with varying deposition temperature (between 750 ºC to 850 ºC) was done to determine the Arrhenius deposition rate of NCG using PECVD. Variations in deposition parameters and optimization steps carried out are detailed in Chapter 4.

Plasma is generated by an electric field applied between the top and bottom electrodes to assist in the dissociation of methane. This plasma source is known as capacitively coupled plasma (CCP), as the plasma is confined between two parallel plates. The bottom electrode is heated by a graphite heater. The temperature of the heating stage is monitored via a thermocouple embedded inside the bottom electrode. The temperature is regulated by a control system which adjusts the heating power based on the temperature reading from the thermocouple. The heated bottom electrode raises the temperature of the substrate such that gaseous by-products gain enough energy to desorb, but carbon atoms gain only enough energy to diffuse on the surface and form bonds with other carbon atoms (Nucleation phase). As the sensor is embedded within the lower electrode, the recorded temperature may vary from actual sample temperature. In this work, only the recorded temperature is reported.

The inflow of process gas is controlled by a pressure regulated valve and mass flow controllers. The mass flow controllers allow precise control over the ratio of gas pumped into the chamber. For NCG deposition, the chamber pressure is regulated at about 1500 mTorr.

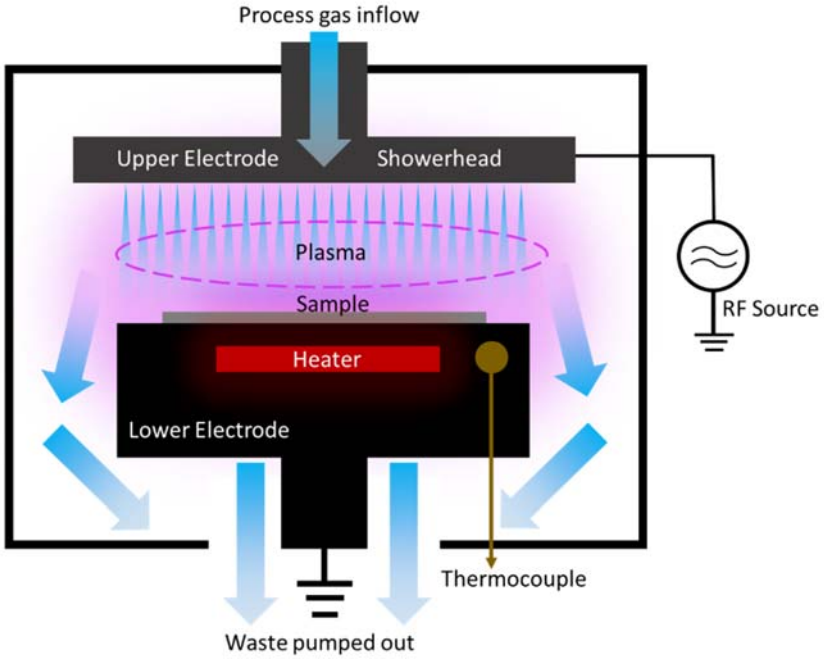

Figure 13: Illustration of the PECVD deposition process

Figure 13 shows the overall illustration of the PECVD process. The mixed process gas is introduced into the PECVD chamber via the upper electrode. The upper electrode consists of a showerhead structure designed to introduce gas uniformly across the whole deposition area. Waste gas is pumped out from the chamber via the exhaust port located underneath the bottom electrode. Hydrocarbons that are deposited onto the sample will desorb due to the high surface temperature and be purged by the flow of waste gas flowing out of the chamber.

The deposition parameters are summarized below:

Table 2: PECVD Deposition Parameters

Parameters	Value
Temperature (°C)	850
RF Power (W)	100
Chamber Pressure	1500
CH_4 Flowrate (sccm)	75
H_2 Flowrate (sccm)	60

3.4.2 NCG patterning with Oxygen RIE

The NC-graphite film was etched with O_2 RIE into different geometrical shapes and dimensions to be used in the subsequent experimental steps. The main structures are rectangular strips with different scales and aspect ratios. Standard photolithography was used for photo transfer, using S1813 as the photoresist.

The spin coating steps discussed in section 3.3 were repeated to obtain a uniform coating of about 2-micron. The pattern is transferred with a bright field mask via UV exposure on an *EVG 620TM* mask aligner and developed with MF-319 for 45 seconds.

The exposed wafer is then etched with an *Oxford Instruments RIE80+* using the O2 etch with a quartz back-plate. The etch duration differs based on the thickness of the NCG film. The wafers are inspected under an optical microscope after etching to determine the alignment error (See Figure 14).

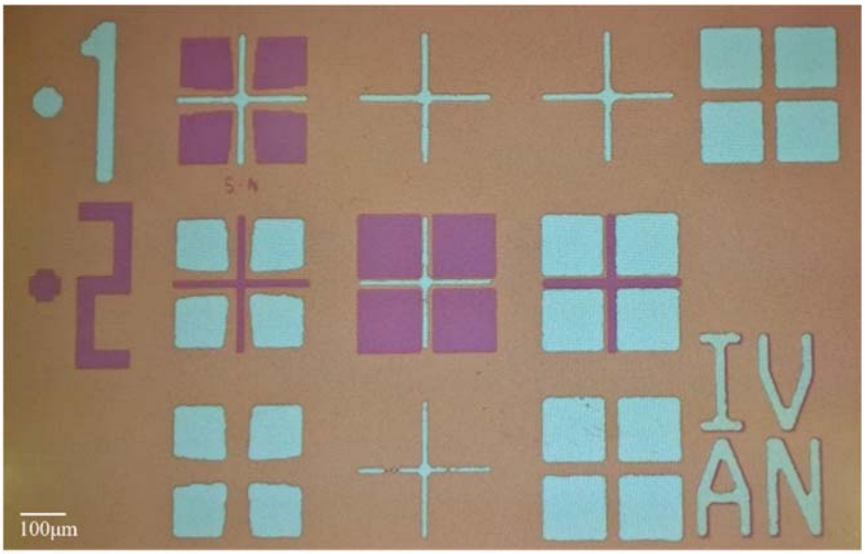

Figure 14: Alignment Marks with (1) Etched SiO2 and (2) NCG taken on B01W03

The average estimated alignment error is approximately 5.5µm across the wafer between the NC-graphite and etched SiO2 patterns. As the SiO2 trenches serves mainly as dicing marks and alignment guides, the error is well within designed tolerance.

3.4.3 Deposition results

For the fabrication of the devices, all depositions were carried out at 850 ºC to ensure uniform deposition rate. The thickness of the NC-graphite layer was controlled by varying the deposition time as shown in Table 3. CH_4 and H_2 flow are kept constant at 75 and 60 sccm respectively. The pressure of the chamber was maintained at 1500 mTorr, and the RF power was set to 100 W (See Table 2).

Table 3: Wafer thickness and deposition time

Wafer ID	Deposition Time (s)	Target Thickness (nm)	Average Thickness (nm)	Sheet Resistance (Ω/□)	Resistivity (kΩ cm)	Deposition rate (nm/s)
B01W01	790	50	43.69	2849.25	124.47	0.055
B01W02	1590	100	94.53	1101.67	104.14	0.059
B01W03	3200	200	185.91	476.67	88.62	0.058
B02W04	3130	150	189.59	469.20	88.96	0.06
B02W05	360	10	17.92	5332.54	95.56	0.049
B03W01	240	10	11.09	12194.44	135.24	0.046
B03W02	909	50	34.68	3247.00	112.61	0.038
B03W03	3360	100	68.30	1464.12	100.00	0.020
B03W04	7500	150	303.90	256.33	77.90	0.040
B03W05	5500	200	212.56	376.44	80.02	0.038

The wafer ID in the Table 3 is based on the deposition batch and deposition sequence. B01W01 denotes the first wafer in the first batch produced. B01 and B02 belong to the same experimental group but were split into two batches due to the Southampton cleanroom shutdown period. Deposition sequence in B01 and B02 was not deposited in any order, whereas for B03, the thickness of NCG was increased in each successive deposition. The deposition rate used for B01 and B02, was calculated based on the Arrhenius rate experiment detailed in section 4.2. During the deposition process of B03W01 – B03W03, the deposition rate is observed to degrade from 0.046 to 0.020 nm/s. Hence, a chamber clean process was done between B03W03

and B03W04 using CF_4 and Oxygen plasma to remove any residues from the PECVD chamber. After the chamber clean, the deposition rate improves to 0.040 nm/s. Due to the increase in deposition rate after the chamber clean, B03W04 was thicker than expected. Adjustments were made to B03W05 to compensate. The resistivity of the film is also observed to decrease with increasing film thickness, which is unusual, as one would expect the resistivity to remain constant, while the *resistance* decreases due to the increased film thickness. Further discussions on this point will be presented in section 4.3.

3.5 Ti-Al contact pads deposition and characterization

3.5.1 E-beam evaporation

The metal pads are deposited using e-beam evaporation. Patterns are formed using a lift-off process. To start, the wafer is spin coated with AZ2070 at 6000 rpm to form a 4-micron thick film for lift off. The AZ2070 resist forms an undercut profile which is ideal for lift-off process. The film is baked at 110 ºC for 60 s before UV exposure with a bright field mask on an *EVG 620TB* mask aligner. A post-expose bake of 110 ºC for 60 s is required before it is developed with AZ300 MIF.

E-beam evaporation was chosen because it provides a directional deposition, making it ideal for lift-off process. The E-beam metal evaporation is carried out on a *Leybold Lab 700eb Evaporator* as it allows precise control over the metal profile and evaporation process. For the first run (B01), 150nm of aluminium was deposited onto the devices as contact pads. However, it appears to be too thin for probing, as the device was easily damaged by the tungsten needles. For the subsequent fabrications (B02, B03), the thickness of the aluminium deposition was increased to 400 nm with 20 nm of titanium added as an adhesion layer. After metal evaporation, the excess metal is lifted off by removing the AZ2070 underneath the metal with N-Methyl-2-Pyrrolidone (NMP) via heated ultrasonic bath.

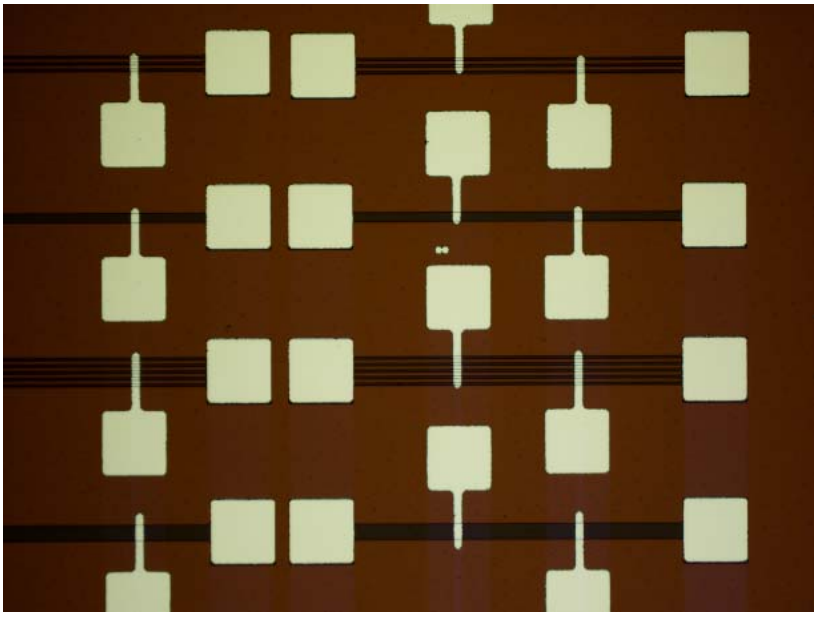

Figure 15: A optical microscope image showing parts of the 4-terminal resistive sensing device after metallization

The deposition result was checked manually with an optical microscope. Figure 15 shows the 4-terminal resistive sensing elements after the lift-off process has been carried out. The metal pads appear to be well formed, however, some rounding of the edges can be seen due to slight over-exposure of the photoresist during development.

3.5.2 Transmission line method (TLM) contact resistance measurement

After the lift-off process, the contact resistance of the metal-NCG interface was estimated using the transmission line method (TLM) with the structure shown in Figure 16. For the TLM measurements, 8 aluminum pads are deposited onto a 7100 µm NCG strip. The pads are spaced at increasing distance (measured from center of a pad to the next), at 600 µm, 700 µm, 800 µm, 900 µm, 1000 µm, 1100 µm and 1200 µm respectively. Measurement was done between the first pad and each subsequent pad.

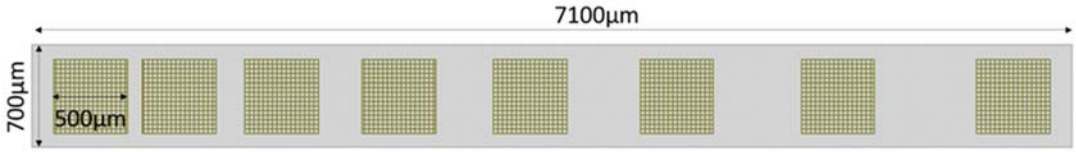

Figure 16: TLM Structure on fabricated chip

The TLM measurements are done with Quater Research low noise triaxial probes mounted on Rucker-Kolls micromanipulators. The measurement was done using an Agilent 2602

Source-Measurement Unit operating in 2 wire resistance measurement mode. The measurement results are shown in Section 4.8.

3.6 SU8 Deposition

The Microchem SU-8-2 (viscosity: 45 cSt) photoresist is spin-coated onto the wafer at 3000 rpm to form a 1.5-micron film. The film is then soft-baked for 60 s at 95 ºC to evaporate the solvent. UV exposure is done with a dark field mask on an *LE03 EVG 620TB* mask aligner. The wafer is subsequently developed with SU-8 developer (1-Methoxy-2-propanol acetate).

Chapter 4: NCG Characterization Results

The characterization results obtained on the NCG films is reported in this chapter. First, the thickness uniformity for sample scale deposition and wafer scale deposition is presented. Then, the deposition rate for deposition runs are calculated with an Arrhenius plot. After that the resistivity of the films at different thicknesses is presented. It was found that the intrinsic resistivity varies with the film's thickness, and a possible explanation is discussed. Hall effect measurements were then done to investigate the cause of the resistivity change, and to determine the majority carrier of the film. Finally, the morphology of the film is characterized using atomic force microscope (AFM), Raman spectroscopy, scanning electron microscope (SEM) and transmission electron microscope (TEM).

4.1 Thickness uniformity

The thickness of the NC-graphite film deposited on to 27 mm x 42 mm substrates are presented, as measured by ellipsometry, in Figure 17. The top and bottom points (y-coordinate above 1cm and below -1cm) of the thickness measurement are ignored due to possible interference caused by size mismatch. In certain cases, one or more points from the ignored coordinates fall outside the sample as the sample is shorter than the measurement range in the Y-direction. All points within the X-direction can be used as the sample is wider than the measurement range in the X-direction. All samples and wafers for the experiment were deposited with deposition time, T_{dep} of 40 minutes (2400 s).

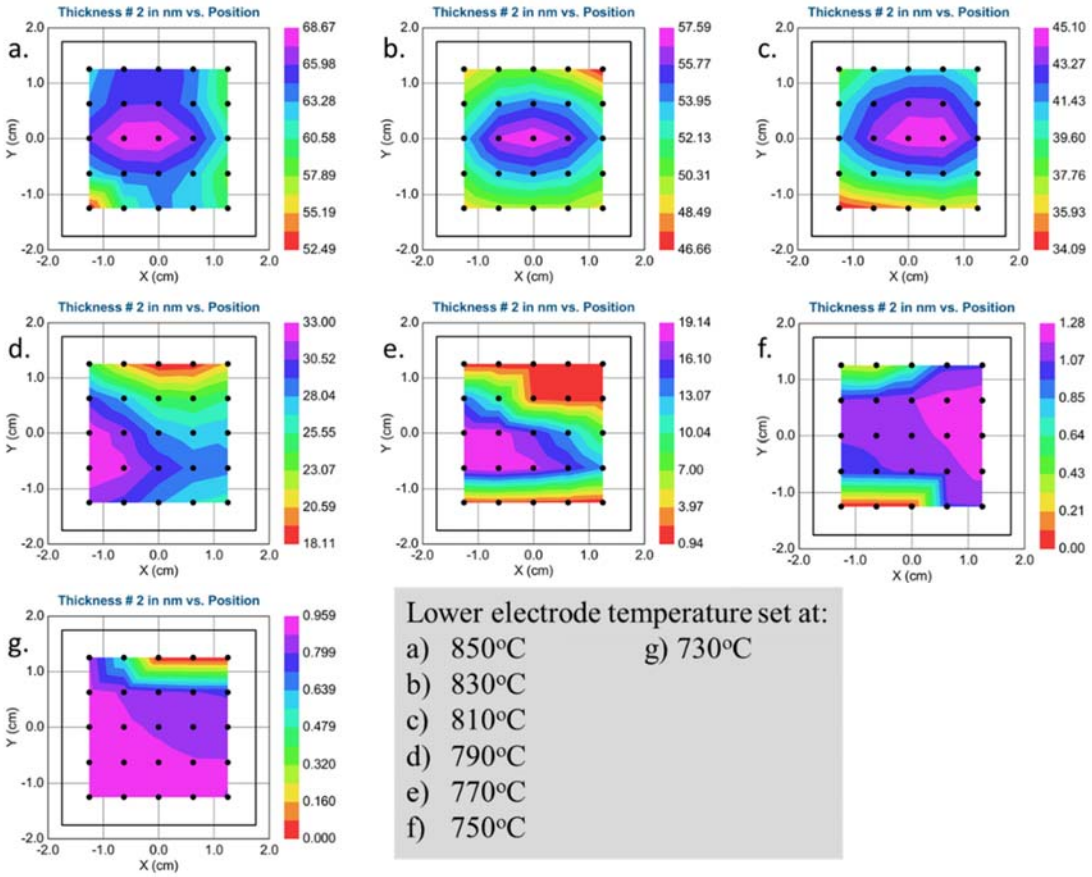

Figure 17: Thickness of deposited film on sample as measured by ellipsometry

In samples a, b, and c, a clear cluster with maximum NC-graphite deposition can be observed. However, in samples d, e, and f, the area with maximum deposition seems to be shifted to the side. In sample g, the ellipsometer registers a somewhat uniform area with variations less than 1 nm. This could indicate that deposition did not actually happen, and that the thickness measurement result is a consequence of model fitting. The non-uniformity of the film could be attributed to the non-uniform thermal distribution on the sample, and the fact that the sample is placed on a carrier wafer without a predefined etch to hold the sample in place. In some cases, the sample may have been placed in areas with denser plasma, in another, it might be in an area with less. Due to this, only the areas where film growth are observed is included in this report. The values are averaged to rule out the non-uniformity problem, to estimate the overall growth rate of the NC-graphite thin film.

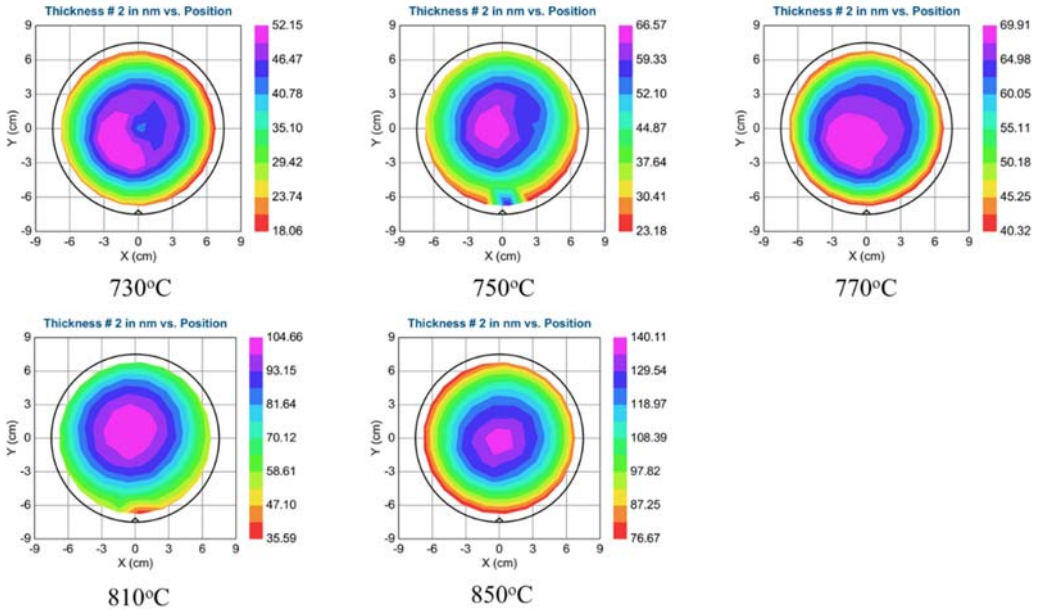

Figure 18: Thickness of deposited film on wafer as measured by ellipsometry

In contrast with the sample-scale deposition, the wafer scale deposition shows clear temperature induced thickness variation patterns as shown in Figure 18. The growth summary of both the samples and wafers are shown in Table 4.

Table 4: Summary of average NC-graphite thickness (D_{ave}) and average sheet resistance (R_s) for samples deposited at different deposition temperature (T_{dep}). The ID starting with 'S' denotes sample-scale deposition, while 'W' denotes wafer-scale deposition.

ID	t_{dep} (min)	T_{dep} (°C)	D_{ave} (nm)	Std. Dev (D_{ave})	R_s (kΩ/□)
S1	40	850	64.056	3.241	1.869
S2	40	830	52.124	2.752	2.407
S3	40	810	40.973	2.725	3.533
S4	40	790	27.002	3.257	6.386
S5	40	770	13.456	4.024	11.457
S6	40	750	0.872	0.343	Contact Limit
S7	40	730	No Dep.	N/A	Contact Limit
W1	40	850	121.610	11.605	0.667
W2	40	810	87.392	18.037	1.178
W3	40	770	66.570	11.924	1.844
W4	40	750	52.150	10.733	2.678
W5	40	730	44.337	7.579	3.300

From Table 4 it is obvious that the thickness of the film correlates strongly to the deposition temperature. Below 730 ^{o}C, no deposition was observed on sample scale depositions.

4.2 Arrhenius plot of NCG deposition rate

The reaction rate for any chemical reaction is governed by the Arrhenius equation. The Arrhenius equation can be thought of intuitively as the increase in the rate of reaction when temperature is increased. At the molecular level, thermal energy can be thought of as an averaged amount of kinetic energy that a group of particles possess. For a chemical reaction to form, the particles need to accumulate enough energy to break existing bonds, or to form new one.

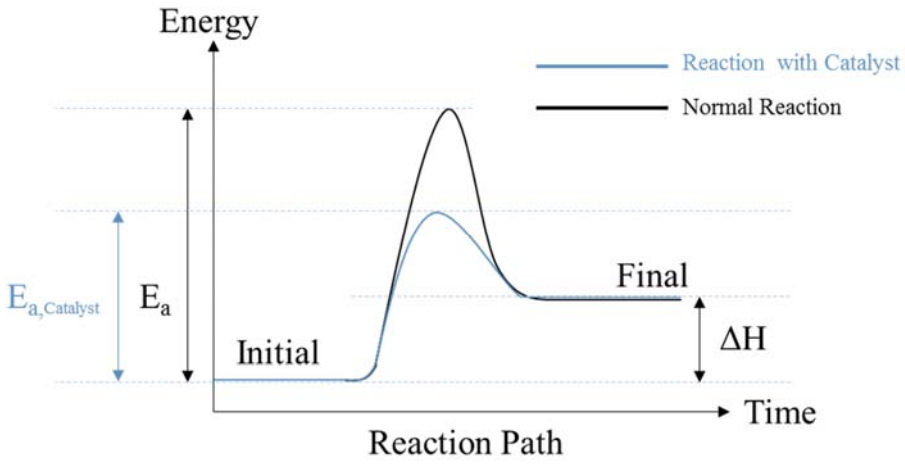

Figure 19: The relationship between activation energy E_a, the enthalpy of formation, ΔH, and the initial and final energy level of a system after a chemical reaction.

Figure 19 shows the concept of activation energy in a reaction with catalyst and one without. Note that the presence of a catalyst does not change the initial and final energy of the reactant, it simply lowers the activation energy, causing an increase in rate of reaction at the same temperature.

The rate of reaction can be generalized as a function of activation energy and temperature. This is where the Arrhenius equation come in. The Arrhenius equation relates the concept of activation energy (E_a) to Boltzmann's distribution law, creating one of the most important equations in Chemistry:

$$k = Ae^{\frac{-E_a}{k_b T}} \text{------ Eq. 9}$$

where,

k is the rate constant of the reaction at a fixed temperature, denoted in per seconds (s^{-1})

k_b is the Boltzmann's constant, 1.3807 x 10^{-23} Joules per Kelvin ($J \cdot K^{-1}$)

T is the absolute temperature in Kelvin (K), and

E_a is the apparent activation energy in Joules (J).

The Boltzmann's constant can be replaced with the ideal gas constant when dealing with a larger collection of particles (i.e. a mole). In that case, the calculation for E_a will yield the activation energy in joules per mol ($J \cdot mol^{-1}$). Understanding the activation energy in thin film deposition is important as it allows prediction to be done on the deposition rate based on the deposition temperature. By manipulating the Arrhenius equation, we can obtain a linear equation of the following form:

$$\ln(k) = -E_a \left(\frac{1}{RT}\right) + \ln(A) \text{ ------ Eq. 10}$$

From Eq. 8, it is apparent that the activation energy, E_a can be obtained from the gradient of an ln (k) against 1/RT graph. The parameter E_a is important as it provides insight into the chemical kinetics of the growth surface without depending on knowledge of the gas phase reaction. This is especially helpful when comparing data with other researchers who use different plasma-enhanced deposition process, where the energy supplied by the plasma may differ.

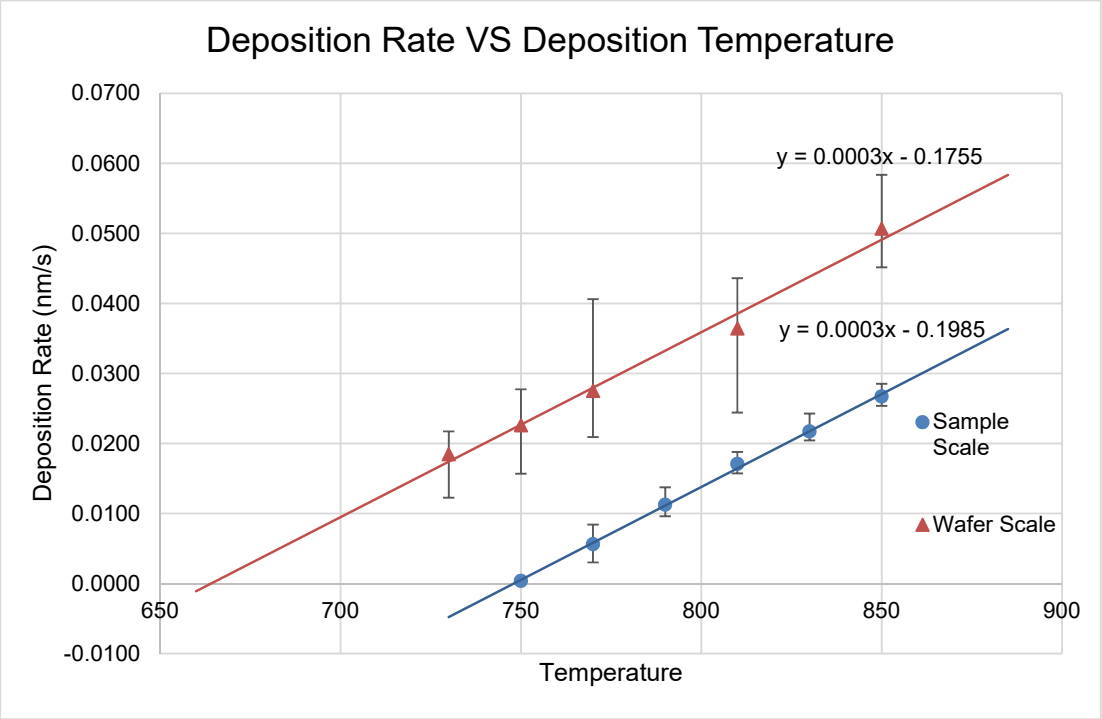

Figure 20: NCG Deposition rate against substrate temperature

Figure 20 shows that the relationship between the deposition rate of NC-graphite and the substrate temperature is linear for both sample scale and wafer scale deposition. The gradient remains almost the same, but the y-intercept for the sample scale lies at a lower point. As the sample is placed on top of a bare silicon wafer, the actual temperature of the sample surface may vary because the heater is controlled by temperature sensors placed at the bottom electrode. Due to the larger deposition area in the wafer scale deposition, the errors due to non-uniformity of film are larger. The films are usually thicker around the centre of the wafer, and gradually thins out towards the edge of the wafer.

The Arrhenius plot can be obtained by plotting the natural logarithm of the deposition rate shown in Table 4 against the reciprocal function of the product of ideal gas constant and temperature in degrees Kelvin.

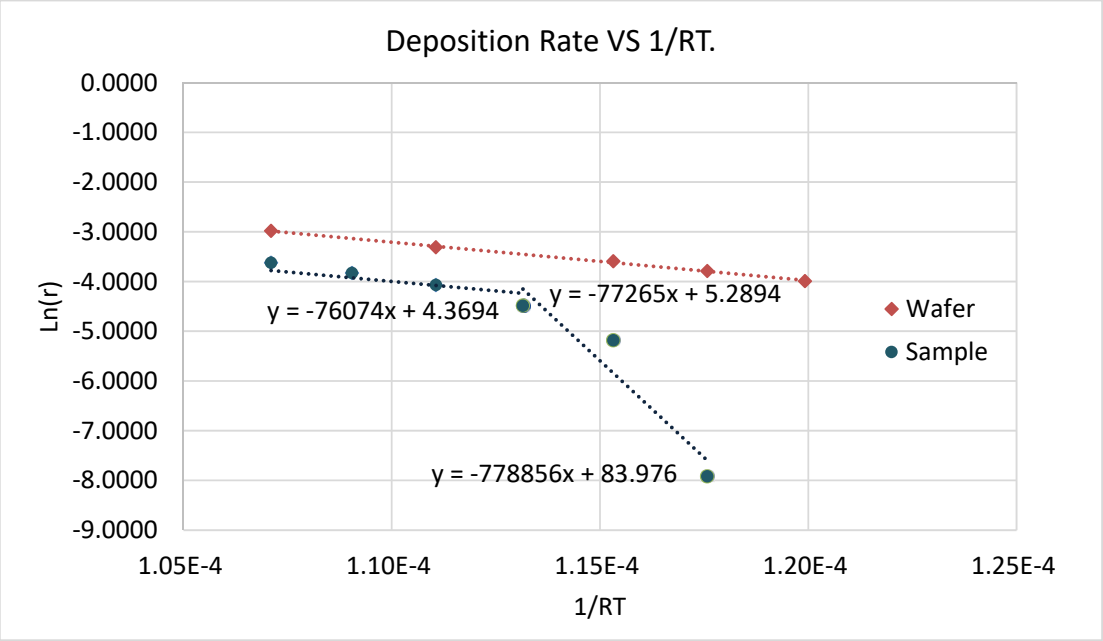

Figure 21: Arrhenius plot for NCG deposition on wafer and sample scale

Figure 21 shows the Arrhenius plots of the deposition and the apparent activation energy E_a can be estimated from the gradient of the linear fit. The sample scale deposition plot tends to negative abruptly due to the extremely low deposition rate at 730 °C. Hence, only the linear regime will be considered for the following calculations. For sample scale depositions, the value of E_a for each carbon adatoms (adsorbed atoms) can be calculated as shown below:

$$\ln(r) = -E_a\left(\frac{1}{RT}\right) + \ln(A)$$

$$E_{a,mol} = 76074\, J\, mol^{-1}$$

$$E_{a,adatom} = 76074\, J\, mol^{-1} \times \frac{1}{6.022\times10^{23}\ adatoms\ mol^{-1}}$$

$$E_{a,adatom} = 1.26323 \times 10^{-19} J$$

$$E_{a,adatom} = 0.788\, eV$$

The same calculation for wafer scale deposition yields E_a = 0.801 eV. The value of E_a denotes the minimum amount of energy needed by the particles to overcome the potential barrier and deposit on the surface of the substrate. The activation energy of other carbon films found in literature is shown in Table 5.

Table 5: Comparison of Activation Energy for Carbon Based Materials

Material	Fabrication method	E_a (eV)	Ref
Vertically Aligned Carbon Nanotubes	PECVD with nickel catalyst, with C_2H_2/NH_3 gas as carbon source and diluent.	0.23	[137]
Graphene	Thermal CVD on Cu catalyst, CH_4 gas as carbon source	2.6	[70]
Twisted bilayer graphene	Thermal CVD on Cu catalyst, CH_4 gas as carbon source	2.74	[138]
Carbon nanotubes	Thermal CVD with nickel catalyst, C_2H_2/NH_3 gas as carbon source and diluent.	1.21	[139]
Nanocrystalline graphite (NCG)	PECVD directly onto SiO_2 substrate with CH_4 as carbon source and H_2 as diluent.	0.801	This work

The apparent activation energy of the NCG could not be compared to similar films due to lack of literature on the material. However, it appears to be significantly lower than the energy required for thermal CVD graphene, and slightly higher than carbon nanotubes with PECVD. In the case of thermal CVD, the rate is limited by the activation energy of the dissociation of CH_4 and C_2H_2. Hence, the reported E_a values for [70], [138] and [139] is higher than their PECVD counterparts. When PECVD is used, the dissociation of carbon source happens due to the energy supplied by the plasma. Therefore, the film growth is limited by surface diffusion. In the case of [137], the E_a value corresponds to the activation energy of carbon surface diffusion on nickel. In the case of NCG, the value of E_a = 0.8 eV is close to the diffusion coefficient of carbon in silicon (0.87 eV) as reported by [140]. The slightly lower E_a could be attributed to the fact that the carbon is diffusing through SiO_2 instead of Si. Further work is needed to verify the activation energy for surface diffusion of carbon on SiO_2 but is not relevant to the scope of this thesis.

4.3 Resistivity

The sheet resistance of the films is investigated using 4-point probes. 12 measurements were made across the whole sample/wafer and averaged. The results of the measurements can be found in Table 4. The average resistivity of the films is obtained by multiplying the sheet resistance with the thickness of the films.

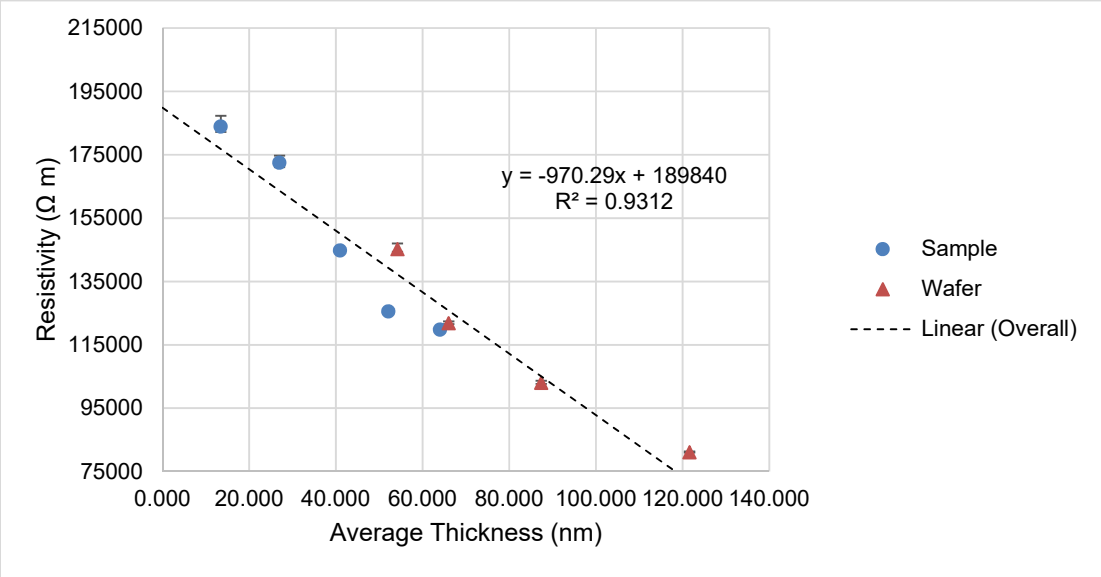

Figure 22: Graph of film resistivity against measured thickness

It is interesting to note that the apparent resistivity of the films seems to be decreasing with the thickness of the deposited films, independent of the geometrical factors. One reason could be the formation of additional layers of grains on top of the first layer, which provides additional conductive path for current to flow. Whereas in the thinner layer, the current can only flow from grains touching each other laterally, thicker films contain more possible paths for current to flow. The hypothesis was later verified in Section 4.5, where the AFM image shows a denser crystal grouping for thicker films, and a somewhat discontinuous structure for thinner films.

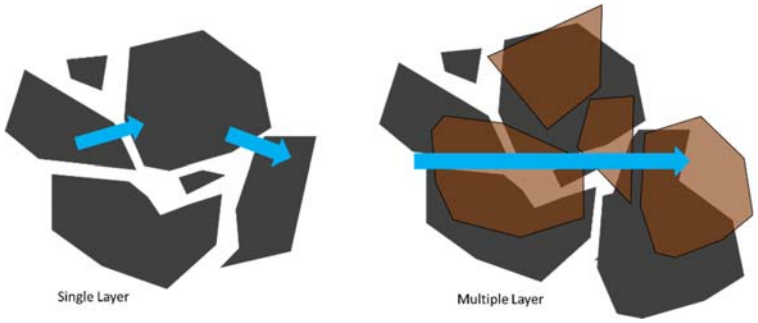

Figure 23: Graphical illustration of possible cause for decrease in intrinsic resistivity

In Section 4.5, the FESEM and AFM images seems to indicate clear granular structure with amorphous carbon spread between the grains. This creates a non-homogenous resistivity within the film, with conductive nanocrystals surrounded by resistive amorphous carbon. The amorphous nature of the material surrounding the grains was verified with TEM and SAED in Section 4.7.

Therefore, change in measured resistivity of the film could be attributed to the non-homogeneity in the film's nanostructure. These effects will need to be taken into consideration in the final sensor design.

4.4 Hall effect characterization

Hall effect measurement was done to identify the carrier concentration and carrier type of the NCG film. The Hall effect measurements were done at room temperature (25 ^{o}C) with current setting of 0.1 mA, 0.5 mA and 1 mA. The characterizations were done on samples measuring 1cm by 1 cm with 200 um square Ti/Al contacts deposited via e-beam evaporation.

In a Hall effect measurement, current is passed through the sample with a strong magnetic field perpendicular to the direction of current flow. Due to the deflection of charge carriers by the magnetic field, a potential difference occurs in the direction perpendicular to both the current flow and the magnetic field. Hall effect measurements allows the determination of the carrier type and carrier concentration of a material.

Previous work done by [8], [10], [91], [141], [142] suggests that graphitic materials are p-type semiconducting, however, in-depth study on the actual carrier type and concentration was not done. Work done by [1], [20], [71], [135] are on graphene and graphite gas sensors, where the Hall coefficients strongly resembles that of a p-type semiconducting gas sensor, while [136] works on multi-wall carbon nanotubes, and the effects of moisture and ammonia on the carbon nanotube's resistance is studied. Here, we report for the first time, a Hall effect measurement on PECVD grown NCG sheet to identify the carrier type of the material.

The results of the Hall effect measurement taken on two chips with different thicknesses is as shown in Table 6.

Table 6: Summary of Hall Effect measurements

Thickness (nm)	Measuring current (mA)	Average sheet concentration, σ (cm^{-1})	Average Mobility, μ (cm^2/vs)	Average Hall coefficient
68.3	0.1	$8.79x10^{14}$	5.24	+0.0426
68.3	0.5	$8.58\ x10^{14}$	5.36	+0.0436
68.3	1.0	$8.63\ x10^{14}$	5.33	+0.0433
303.9	0.1	$1.53\ x10^{15}$	6.52	+0.0246
303.9	0.5	$1.49\ x10^{15}$	6.66	+0.0252
303.9	1.0	$1.49\ x10^{15}$	6.60	+0.0250

The average sheet concentration and mobility is observed to increase with the thickness of the film, which corresponds to the increase in the intrinsic resistivity of the film as explained in 4.3. The resistivity of the film is related to the mobility and the sheet concentration via the following equation:

$$\rho = \frac{1}{q(\mu_n n + \mu_p p)} \quad \text{------ Eq. 11}$$

Where q is the unit charge, μ is the mobility of the carrier, and n and p are the concentration of the negative and positive charge carriers respectively. For our measurement, the majority carrier is positive, hence the equation can be simplified to:

$$\rho = \frac{1}{q(\mu_p p)} \quad \text{------ Eq. 12}$$

As both the mobility and the carrier concentration increase with increased thickness, the resistivity decreases.

The measurement suggests hole-transport in NCG films. Although the origin of this property is unknown, it is believed that the defective grain boundary plays an important role in modulating the majority carrier of the material. In a perfect graphene or graphite crystal, one would expect n-type semiconducting behaviour, due to the delocalized pi-electrons in the benzene ring structure. However, in a highly defective sample, the defected region may have sp^3 bonds and oxygen bonds which could potentially cause electron localization. The bound states would then create a "shortage" of electrons in the material, allowing for hole conduction to occur.

4.5 Surface morphology

AFM measurement was carried out on samples S1 to S5 to investigate the effect of deposition temperature on the surface morphology of the film (See Figure 24). The height profile and phase image were taken to study the film's surface. The height profile allows the surface roughness to be estimated, while the phase image may show regions with variations in surface properties, such as different elasticity, friction or adhesion.

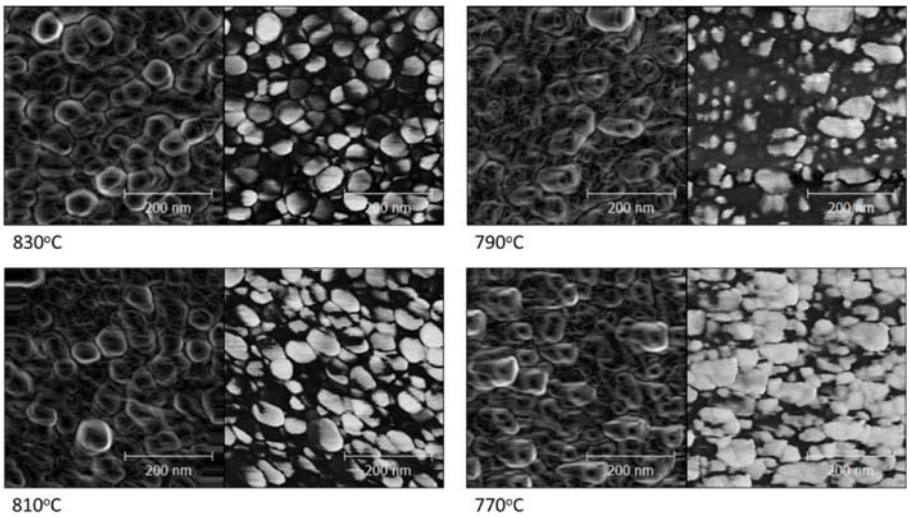

Figure 24: AFM image of sample scale deposited films at different temperature (770 °C – 830 °C). Right image is an edge enhanced AFM image, left image is the phase image. Z-height range from 0 nm to 15 nm (See Figure 24 for height profile).

The absolute roughness, R_a for the films is 1.63 nm (± 0.05 nm), while the RMS roughness of the films is 2.11 nm (± 0.08 nm). The surface roughness variation across films deposited at different temperature is not great. The AFM image of sample deposited at 850 °C is shown in Figure 25, as more detailed analysis was done on the sample.

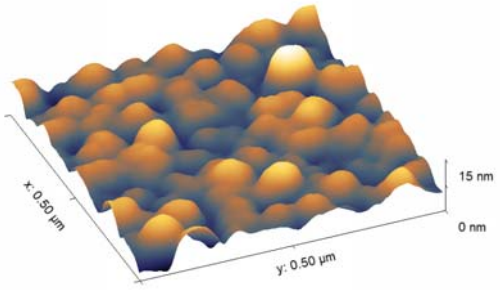

Figure 25: 3D view of surface roughness profile of film deposited at 850 °C z-height normalized to 0 nm -15 nm

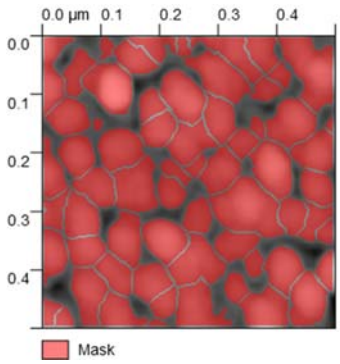

Figure 26: Watershed for grain size estimation

The mean grain size was estimated based on the sample deposited at 850 ºC as it provides the best watershed image. The mean grain equivalent disc radius obtained was 37.57nm. Also, from the phase image, it is observed that the grains on the thinner film (770 ºC deposition) shows a flatter phase difference when compared to the ones observed in the thicker films. The grains formed at 770 ºC are made up of flat islands, as the average thickness of the film is only 13.45 nm.

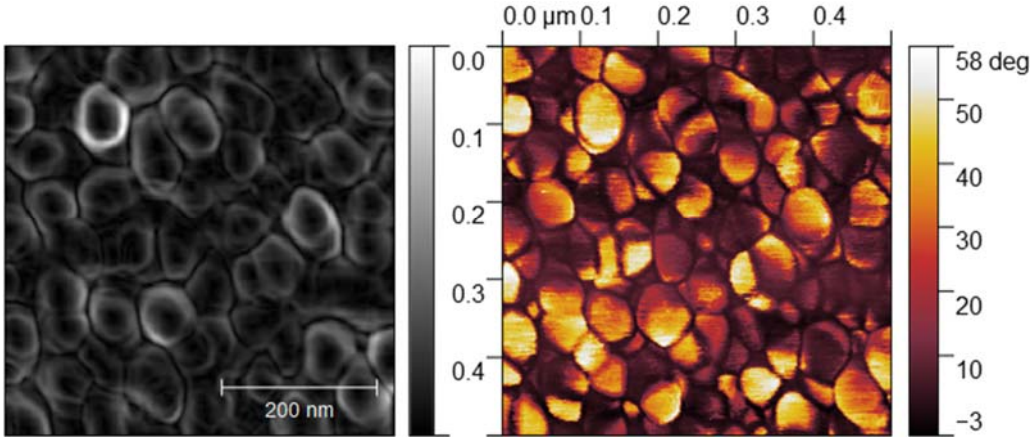

Figure 27: Edge enhanced AFM height profile and AFM Phase image of NCG deposited at 850 ºC showing clear phase differences between grains and grain boundaries.

As the film thickness grows, the grains became more circular in shape, and more evenly distributed. Since the phase shift of the cantilever is sensitive to the surface stiffness and adhesion properties [143], the phase image clearly shows the presence of two different material on the film (Figure 27). We investigated the grain structure further using field emission scanning electron microscope (FESEM). The FESEM images are taken at MIMOS Bhd. with a Hitachi SU8030 FESEM.

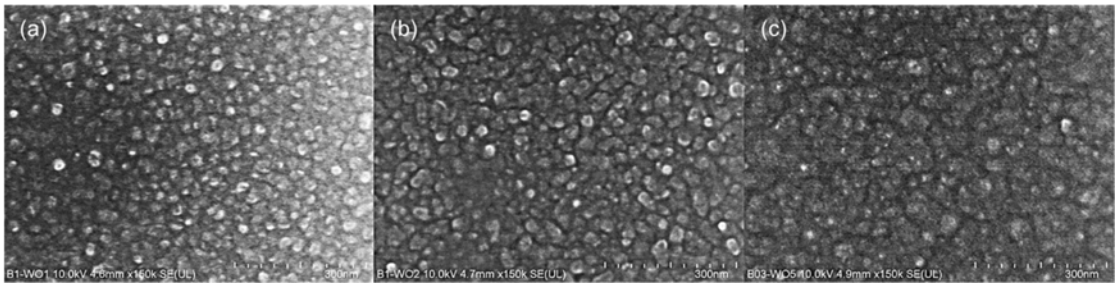

Figure 28: FESEM images of NCG grown at 850ºC with different thicknesses: (a) 43 nm (Target: 50 nm), (b) 94 nm (Target: 100nm), (c) 212 nm (Target: 200nm). Note that 300nm at the scale bar refers to the interval between each tick marks.

From the FESEM images in Figure 28, the NCG film clearly exhibits granular characteristics. As the thickness of the film was increased with increasing deposition time, the grains appear to agglomerate, forming grain clusters which are thicker. This could be attributed to the growth of amorphous carbon which could grow around multiple crystallite grains, fusing them into a bigger grain. The presence of amorphous carbon between the NCG grains was confirmed by visual inspection of the TEM image and analysis of the SAED pattern (See Section 4.7). The decrease in grain boundaries for thicker film could be the reason for the slightly decreased sensing performance of the sensor with thicker films.

Note that the thinner film also exhibits a slightly more significant charge-up effect during the SEM imaging. This can be attributed to the slightly higher resistance of the thinner NCG film as explained in Figure 23. Having higher charge-up effect also means that a higher resolution image could not be taken on the thinner NCG film.

4.6 Raman spectroscopy

The Raman spectrum of NCG was obtained using a Renishaw inVia Raman Spectrometer with a 650nm laser with a single spot with spot size of 1µm directly after fabrication. The Raman spectrum was performed at room temperature (24 ºC) and the laser power was set to 5mW constant power. The resultant spectra (see Figure 28) show clear D and G peak with visible 2D and 2D' peak.

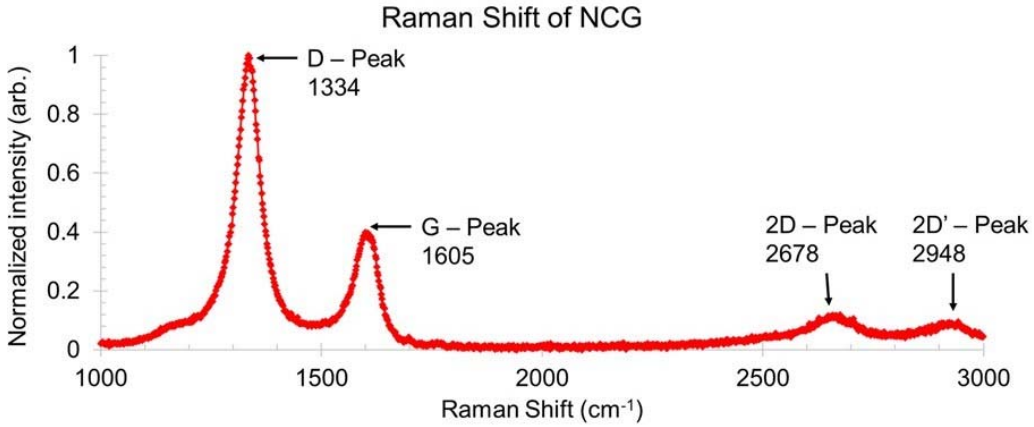

Figure 29: Raman spectrum of NCG (B03W05)

The Raman spectra of the film is comparable to those reported in [10], [144], [145]. The high D-peak in the spectrum is an indication of high defect density in the sheet as the D-peak is generally attributed to the bond stretching of carbon atom pairs. The G-peak, on the other hand, corresponds to the breathing mode vibration of the graphitic rings [146]. Both the G-peak and the D-peak observed are due to the sp^2 bond vibrations.

As the intensity of G peak and D peak corresponds to the presence of carbon pairs and rings in a film, it is possible to determine the degree of amorphization of a film by observing the change in ratio between the two peaks, and the shift in the G peak. The term "nanocrystalline graphite" is introduced as the film contains clusters of graphitic rings, held in place by a matrix of amorphous carbon. Following the three-stage model of carbon amorphization proposed by Ferrari and Robertson [146], the ratio of the D-G peak intensity should be around 2.

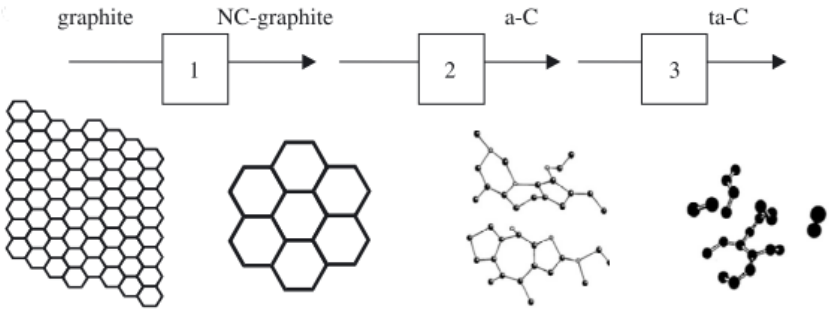

Figure 30: Three-stage model proposed by Ferrari and Robertson [146]

The model first considers the characteristics of pristine graphene with breathing mode vibration, and carbon pair vibrations. The binding geometry of a pure graphite crystal lattice restricts the vibration of each individual aromatic ring. As the level of disorders increase, the intensity of D peak increases as well. The breaking of the pure crystalline graphite into smaller graphite nano crystals means that more aromatic chains have the freedom to vibrate in breathing mode. As the level of amorphization increases beyond that, the rings start to break, forming amorphous carbon with less aromatic rings. Thus, the D peak to G peak ratio decreases again. The NCG deposited in this work has a D-G ratio of around 2, which is enough to be classified as “nanocrystalline graphite”.

4.7 TEM and SAED

TEM studies were done to verify the validity of the Raman and surface morphology characterization, and to ensure that the material deposited was NCG, and not graphene oxide. The SAED pattern was analysed to obtain the interlayer spacing, and to determine the crystallinity of the sample. The interlayer spacing of the sample is then used to verify the presence of graphite nanocrystals on the sample instead of graphite oxide. This is important as the NCG film was patterned with O_2 RIE.

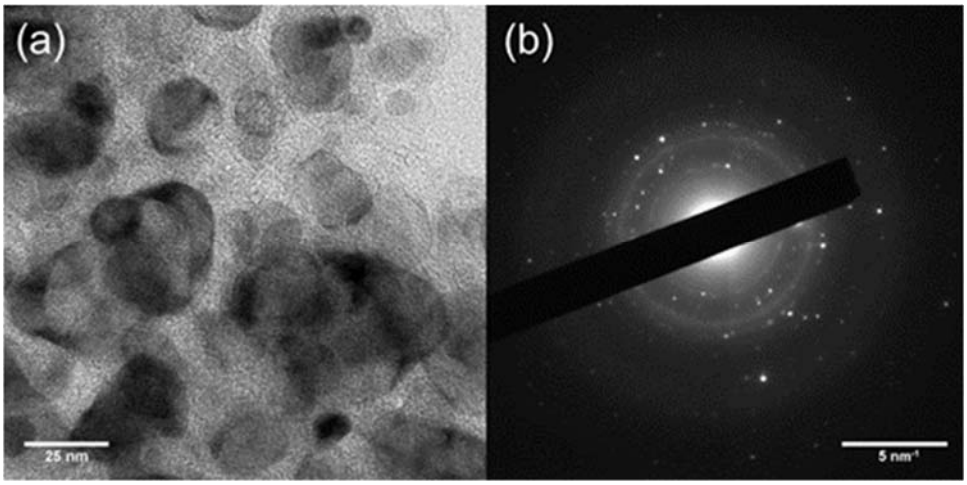

Figure 31: (a) TEM and (b) SAED images of NCG taken by Dr.Sam Fishlock from the University of Ulster.

Figure 31 shows the TEM images. The samples were prepared using mechanical exfoliation into ethanol, sonicated for 10 minutes, and micropipetted into a copper supported holey carbon grid (Agar Scientific Holey Carbon Film on 300 mesh cu). HRTEM (JEOL JEM-2100F) was used for imaging at 200keV excitation.

The TEM images shows small crystallites dispersed and immobilized on the holey carbon grid. The SAED image of the sample taken shows diffuse rings with bright spots. The bright spots are indicative of crystallites of a certain orientation, while the diffuse rings are indicative of the amorphous region of the film [147]–[149].

The interlayer distance of the film can be calculated by measuring the radius of the rings in the SAED image as shown in Figure 32.

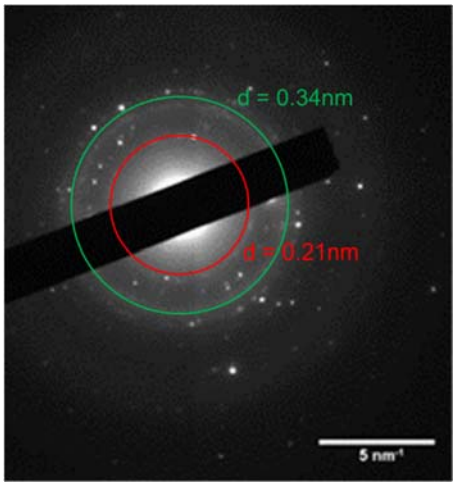

Figure 32: Calculating the interlayer distance from SAED for verification

In Figure 32, two of the brightest rings in the SAED image was taken as reference for calculation. The radius of the circles in reciprocal space (nm^{-1}) was taken and converted into real space (nm). The value of the radius (d = 0.34 nm, d = 0.21 nm) is the interlayer distance of the graphene sheets in the graphite crystals. These values are comparable with known XRD data of graphite [150], which shows two major peaks at interlayer spacing of 3.39 Å and 2.14Å respectively. Details of the XRD extracted from [150] can be found in Appendix B of this thesis. The measurement confirms the presence of graphite layers in the film. A higher-resolution TEM (HRTEM) image was then taken of a single nanocrystal to verify its graphitic nature.

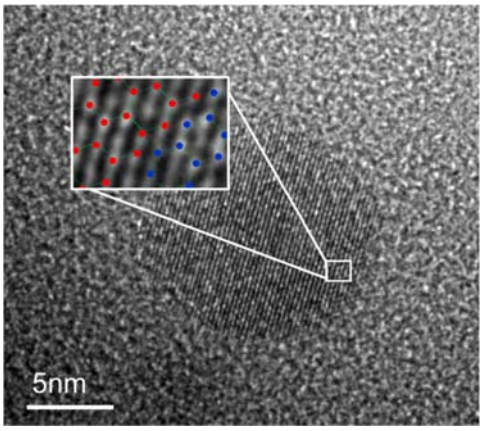

Figure 33: TEM with higher magnification taken at MIMOS Bhd.

Figure 33 shows a higher resolution TEM image taken in MIMOS Bhd, with a FEI Tecnai G2 F20 X-twin TEM system. The image obtained at a much higher resolution allowed us to verify the graphitic nature of the nanocrystals in our film. From the digitally

enlarged photo of the NCG grain, the hexagonal crystal shape is apparent, confirming the graphitic nature of the nanocrystals.

4.8 Contact characteristics

The transmission line method (TLM) of Fig. 16 is used to find the contact resistance of the connection pads. The contact characteristics of a TLM device can be modelled as shown below:

Figure 34: Resistance model of NCG strip between two metal contacts

If all the fabricated contact pads in Figure 16 are identical, $R_{contact}$ will be constant regardless of the length of the NCG strip. As the length of the NCG strip is increased, the total measured resistance increases linearly due to the increase in R_{NCG}. The resistance change can be represented as shown:

$$R_{total} = \frac{R_s}{W}(L + 2L_T) = \frac{R_s}{W} L + 2R_{contact} \qquad \text{------ Eq. 13}$$

where R_s represents the sheet resistance of the NCG film, and L is the length of the NCG strip between the contact pads, and W is the width of the square contact pads (500 µm) (Refer to Figure 16). As the length of the strip, L, tends towards 0, the resistance value of R_{NCG} disappears, hence, the remaining resistance will be the contact resistance contributed by the metal-NCG interface.

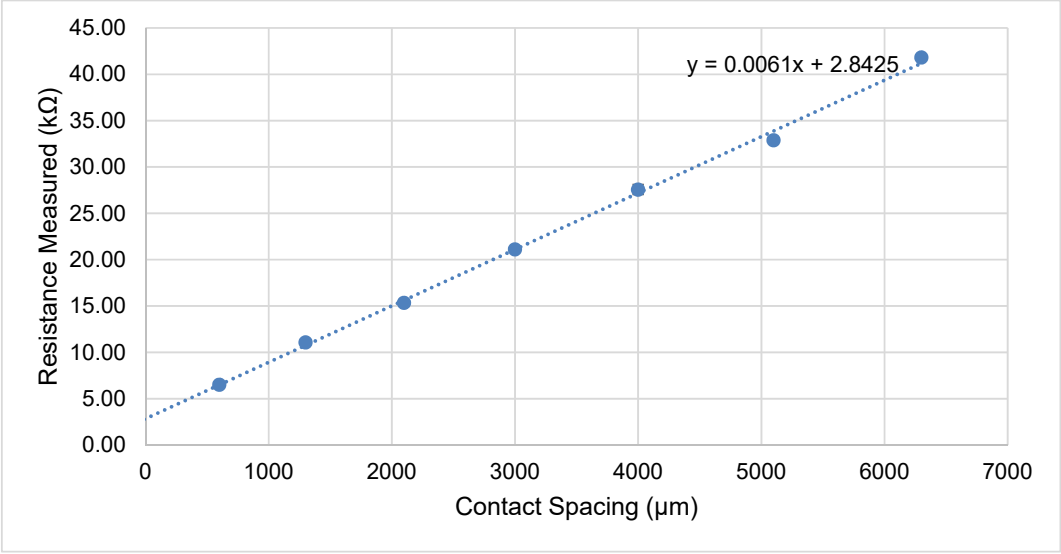

Figure 35: Plot of measured resistance as function of contact spacing for a TLM device

The contact resistance can be calculated by linear interpolation of the resistance-length graph. The graph in Figure 35 shows a y-intercept, $2R_{contact}$ of 2.8425 kΩ, which corresponds to the contact resistance, $R_{contact}$ of 1.421 kΩ. This is an acceptable range of contact resistance, as the resistance of the strip lies in the 0.1 MΩ range.

To verify the measurement, one could derive the sheet resistance for a 500µm pad from the graph and compare it to the sheet resistance measured on a four-point probe. The R_s can be found as shown [151]:

$$\text{Slope} = 0.0061 = \frac{R_S}{W} \text{ ------ Eq. 14}$$

$$R_s = 0.0061k\Omega\ \mu m^{-1} \times 500\ \mu m \text{ ------ Eq. 15}$$

$$R_s = 3.05k\Omega \text{ ------ Eq. 16}$$

The calculated sheet resistance is close to the sheet resistance measured by the four-point probe, which is 2.88 kΩ. The IV-characteristic of NCG with the contact was also measured to determine the contact characteristic. Figure 36 shows the IV-plot of NCG strips with different contact separation.

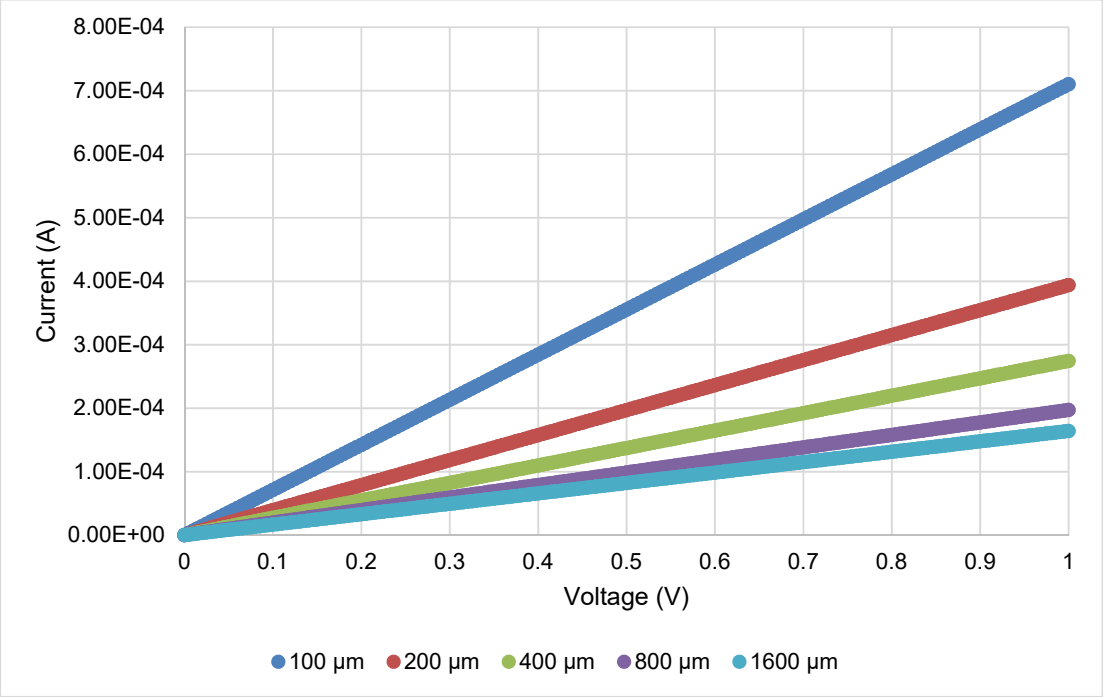

Figure 36: IV-plot of NCG with different length. Voltage sweep from 0 - 1V.

The IV plot shows no indication of a Schottky barrier, indicating the formation of good Ohmic contact between the NCG strip and the metallic contacts.

Chapter 5: Gas Sensing Characterization of NCG Film

In this chapter, the gas sensing characteristics of the NCG film was evaluated. The gas sensing tests was carried out in two sites, with a preliminary test done in the UK, and subsequently a more complete test was done in Malaysia.

5.1 Design and implementation of the gas sensing test chamber

5.1.1 Initial design (UK)

To test the sensors, a sensor test platform was designed and implemented (See Figure 37 and Figure 38). The system consists of two inputs, one for the diluent, and one for analyte. The analyte chosen for this test is NO2. The input gas lines are fitted with check valves to prevent back flow of gasses. At the output side, a vacuum pump is attached to remove air from the chamber, while an exhaust line was used to vent the analyte into the atmosphere.

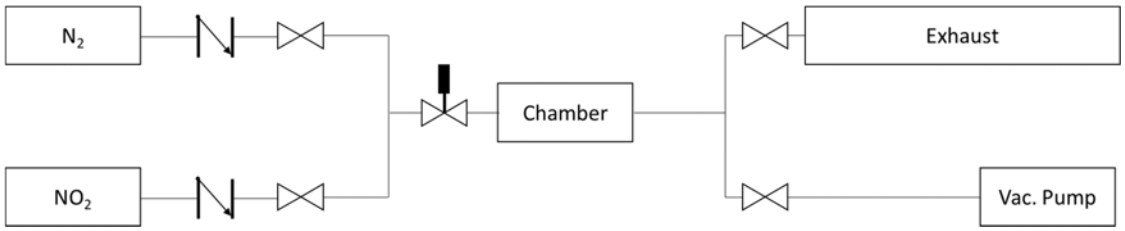

Figure 37: Piping and instrumentation diagram for the sensor test platform

The setup was built during the 2nd year of this project in the Southampton campus using a cleanroom grade vacuum CF cross reducer flange with appropriate electrical feedthroughs modules. The vacuum pump is a rotary vane pump with a maximum vacuum pressure of 10 hPa (1 kPa).

The setup of the chamber is as shown:

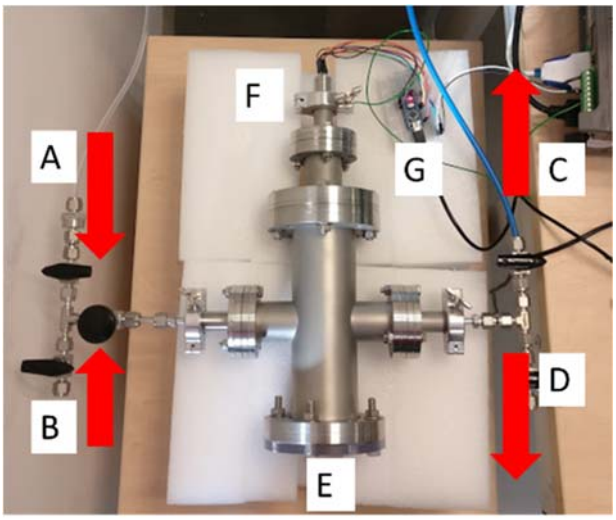

Figure 38: Gas sensor test system in the UK. The description of each components is as follows: (A) NO_2 inlet, (B) Air/NO_2 inlet, (C) Vacuum pump outlet, (D) Vent to atmosphere, (E) Polycarbonate viewport, (F) Airtight wire feedthrough, (G) Microcontroller for control an logging

Inside the chamber, the sensor is placed on a customized PCB, and attached to a sensor housing fabricated with standard stripboard and 3D printed parts. Standard jumper wires are used to connect the desired sensing strip to the output wires connected to a Keithley 2600A 2 channel SMU via phoenix connectors (See Figure 39 and Figure 40).

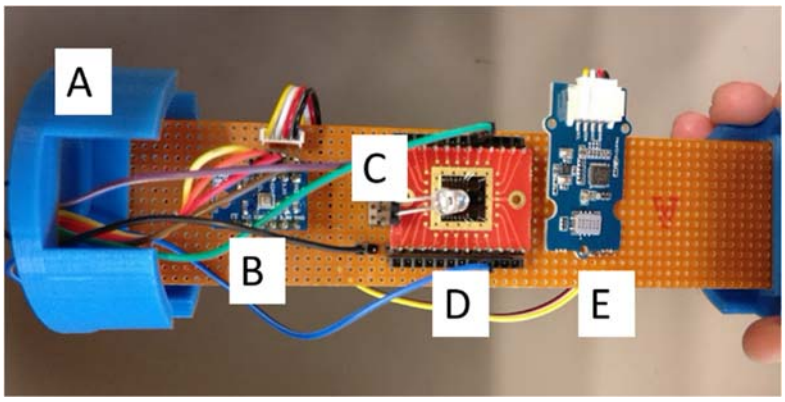

Figure 39: Electrical connection of the gas sensor test system. The description of each components is as follows: (A) 3D printed stripboard housing (B) BME280 pressure, humidity and temperature sensor (C) UV LED to aid in gas desorption (*HELTC UV LED*, λ=365nm, 100mW) (D) NCG sensor mounted on a custom PCB and wire bonded with Al wires (E) Multichannel Gas Sensor Module (*MICS-6814* by SGX Sensortec)

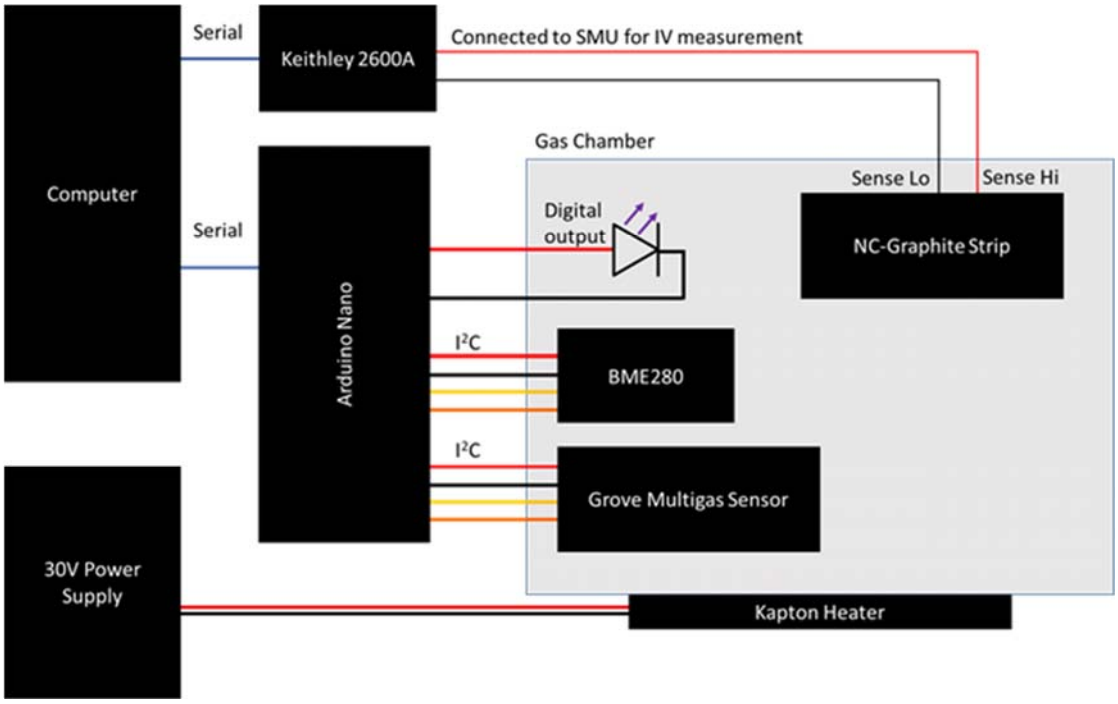

Figure 40: Electrical connection of the test chamber for the NC-graphite gas sensor

The resistance of the strip is measured using a Keithley 2600A Source-Measurement Unit (SMU). The SMU is configured to carry out a voltage sweep from 1V to 2V at an interval of 0.1V. The output current is measured, and the resistance is determined using the slope of the current-voltage curve. If the current-voltage curve is not linear, the readings are treated as invalid, and the experiment will be halted.

The internal environment of the system was monitored using a BME 280 Temperature-Humidity-Pressure Sensor and a Grove Multi-gas Sensor. The output of the sensors are accessed using the I2C protocol through the vacuum wire feedthrough. The BME 280 sensor is effective for temperature range from -40 ^{o}C to 85 ^{o}C, pressures ranging from 300 to 110 kPa and full range of relative humidity (0% to 100% RH). The Grove Multi-gas sensor, on the other hand, is sensitive to multiple gasses, but for this experiment, only NO_2 is of interest. The Grove Multi-gas sensor is sensitive to 0.05 to 10 ppm of NO_2. A UV LED emitting at 360nm was installed inside the chamber to illuminate the sensor with UV light to expedite the desorption process. A Kapton heater was used to control the temperature of the chamber for humidity experiments.

5.1.2 Multigas test setup (Malaysia)

During the 3rd year of the PhD program, another setup was built in Malaysia with mass flow controllers to control the gas flow for different gas concentrations, and heater to

expedite gas desorption. The electrical connection of the new chamber is shown in Figure 41.

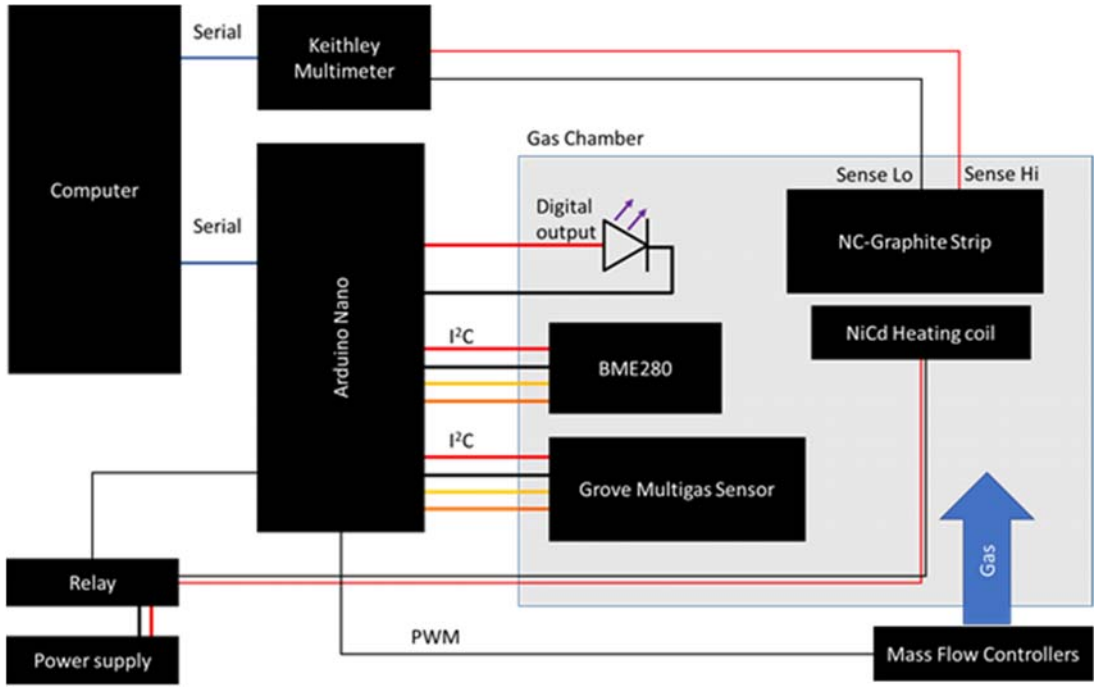

Figure 41: Electrical connection for improved gas-sensor test chamber

The new gas chamber features a single body construction, with polycarbonate viewing window which is sealed with a rubber O-ring. National Pipe Taper (NPT) threads were made on the inlet and outlet of the chamber and fitted with Swagelok adapters. The chamber was fabricated at the Southampton Engineering Design and Manufacturing Centre (EDMC). NiCd heating coils were installed for temperature control. The heating setup works well between the range of 20 – 60 ^{o}C. Figure 42 and Figure 43 shows the structures of the fabricated chamber while Figure 44 shows the software interface.

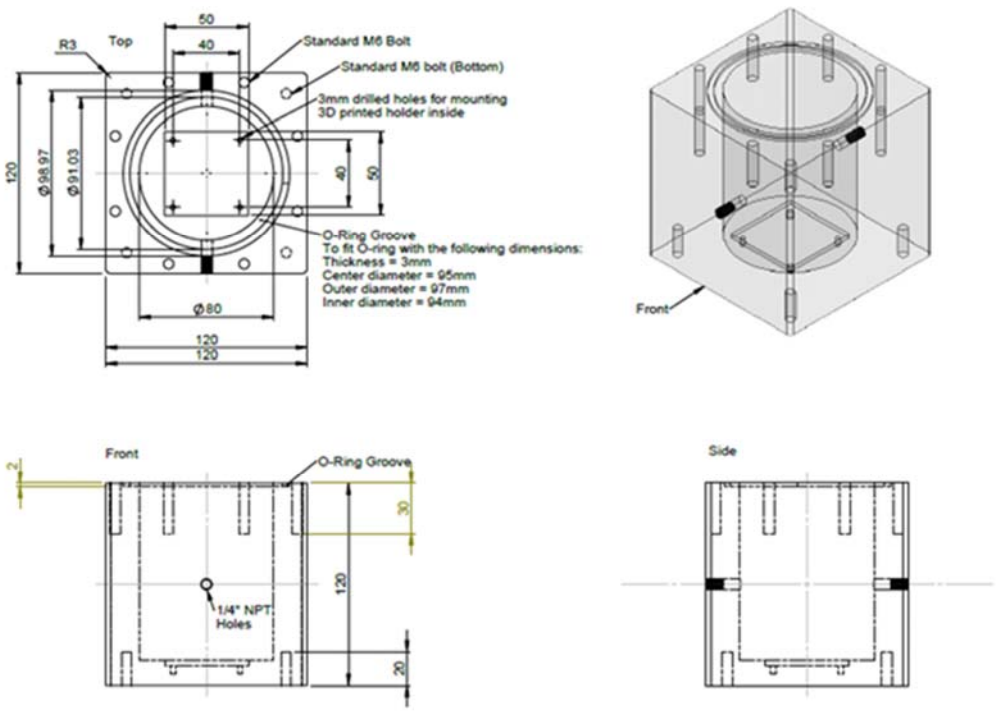

Figure 42: Mechanical drawing of gas test chamber

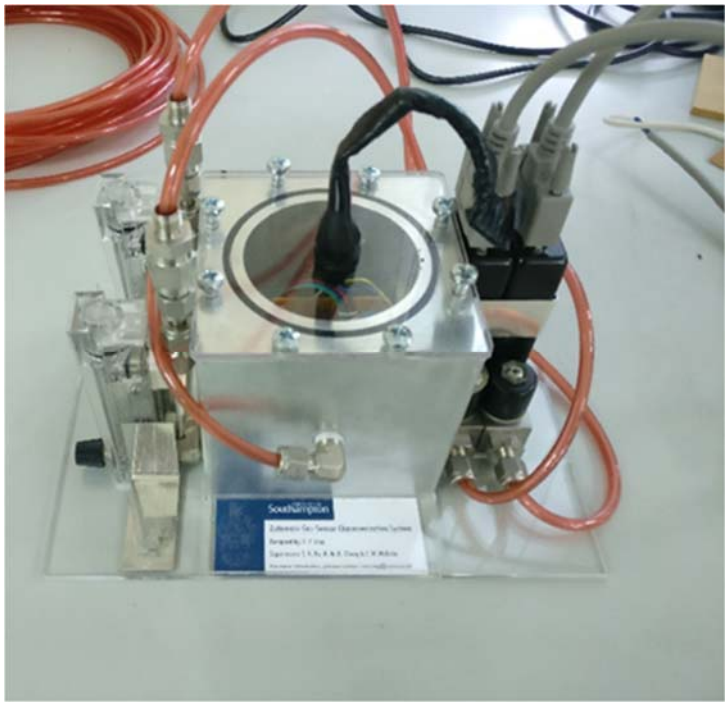

Figure 43: Fully assembled test chamber

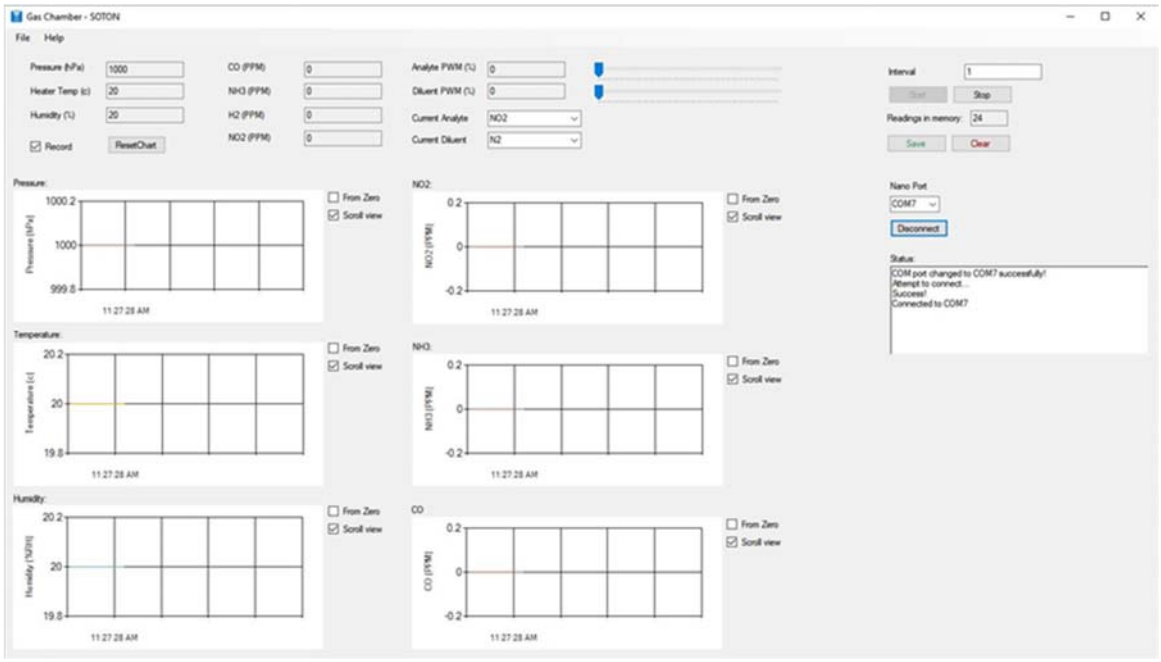

Figure 44: Screenshot of the gas sensor test chamber controller.

The gas sensor test chamber was controlled via a simple software written for Microsoft's .NET platform using C#. The sensor data obtained was stored as time indexed CSV files for further analysis.

The types of gas purchased for testing in the multigas test setup are listed in Table 7.

Table 7: List of purchased gas

Gas type	Concentration (ppm)	Diluent
NO_2	10	N_2
NH_3	10	N_2
CO	10	N_2
Synthetic Atmosphere (20.9% O_2 /N_2)	N/A	N/A

All gases were purchased from AirLiquide and stored in CALGAZ portable cylinders. All gases purchased are of calibration grade.

5.2 Preliminary NO2 sensing test (UK)

To gauge the effect if NO_2 on the resistance of the NC-graphite thin film, 10 ppm of NO_2 diluted with N_2 was used for the experiment (BOC UK). However, due to the unavailability of the N_2 supply in the lab during the Cleanroom shutdown period, comparison could only be done between the chamber filled with NO_2, and the chamber filled with ambient atmospheric air. The thickest sensor (303 nm, B03W04) was used at this time as the measured resistance is the lowest among the strips tested.

The first experiment done was to understand the general trend of the sensor's response towards NO2. To do this, the sensor's responses were recorded over an extended period, once with ambient atmospheric air, and another time with NO_2.

For both tests, the temperature was kept relatively constant, at 30.85 ± 0.3 ºC. The resistance of the strip appears to increase after exposure to NO2, which contradicts our previous belief that the NCG is a p-type material. However, further investigation reveals that the rise in resistance could be attributed to the difference in humidity levels when the two sets of measurements were made. The suspicion was confirmed by analysing the scatterplot in Figure 45.

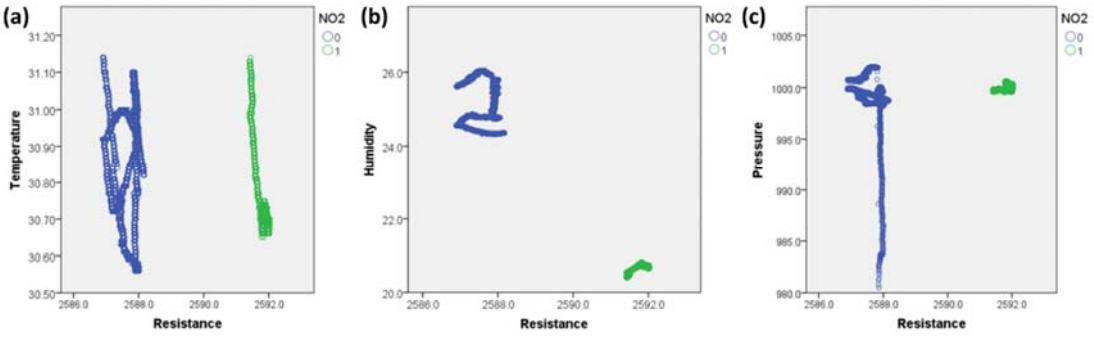

Figure 45: Scatterplots of temperature (ºC) (a), humidity (%RH) (b) and pressure (hPa) (c) against resistance (Ohm)

The scatterplot shows two distinct groups, with the green dots being results from measurement done with 10ppm of NO_2 present and the blue dots being results obtained in air. Apart from the straight line on the blue group in the pressure graph Figure 45(c), the pressure and temperature readings of the two group appears to be in the same range. The straight line is a result of vacuum purging of the chamber to lower the humidity level. From the humidity-resistance scatterplot, it is evident that even after vacuum purging, the chamber's humidity level in the presence of air is still higher compared to the humidity level

of the NO_2. Hence, the apparent rise of the resistance level in the film could be because of the reduction in relative humidity rather than the redox reaction between the NO_2 and the NCG strips.

To mitigate this problem, a temperature and humidity sweep was carried out in the chamber at elevated temperatures. It is observed that at around 50ºC, the relative humidity of atmospheric air is almost comparable to the relative humidity of the NO_2 gas. Therefore, a temperature sweep from 45ºC to 55ºC was carried out. As the heating element of the experiment was controlled manually, some slight inaccuracies were present at the starting point and the stopping point of the sweep.

The experiment is started by purging air out of the chamber and filling it up with NO2. This is done by first reducing the internal pressure of the chamber to about 30 kPa using a vacuum pump and pumping it to 102 kPa with the compressed 10ppm NO2/N2 mixture. The process is repeated 3 times to ensure minimum amount of atmospheric gas in the chamber.

Then, the heater was turned on until the temperature is almost 45ºC, where the data logger is activated. The heating continued until the temperature reads about 55ºC. At that point, the heating was cut off, and the temperature drops to approximately 45ºC again. The same process is repeated with atmospheric air.

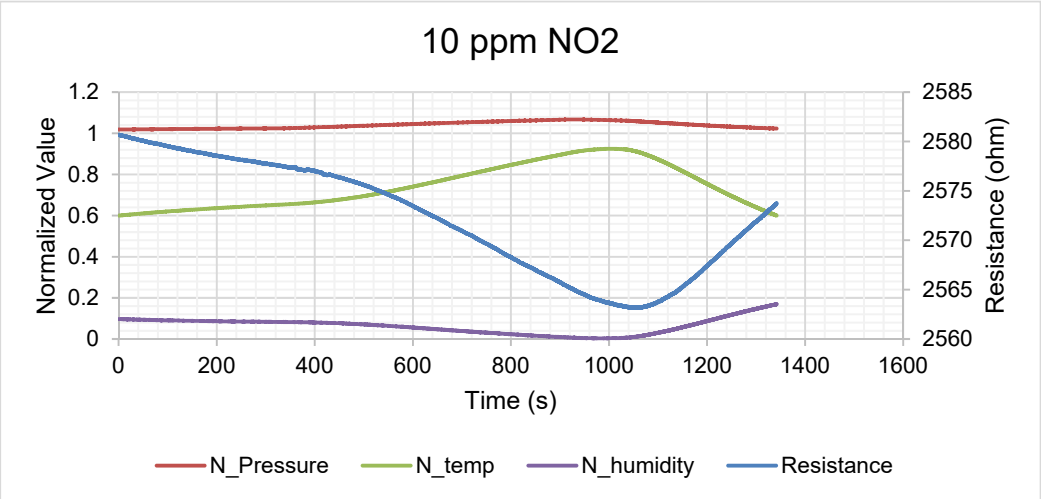

Figure 46: Time-domain response of the resistance, normalized temperature, normalized pressure and normalized humidity when the chamber is filled with NO_2

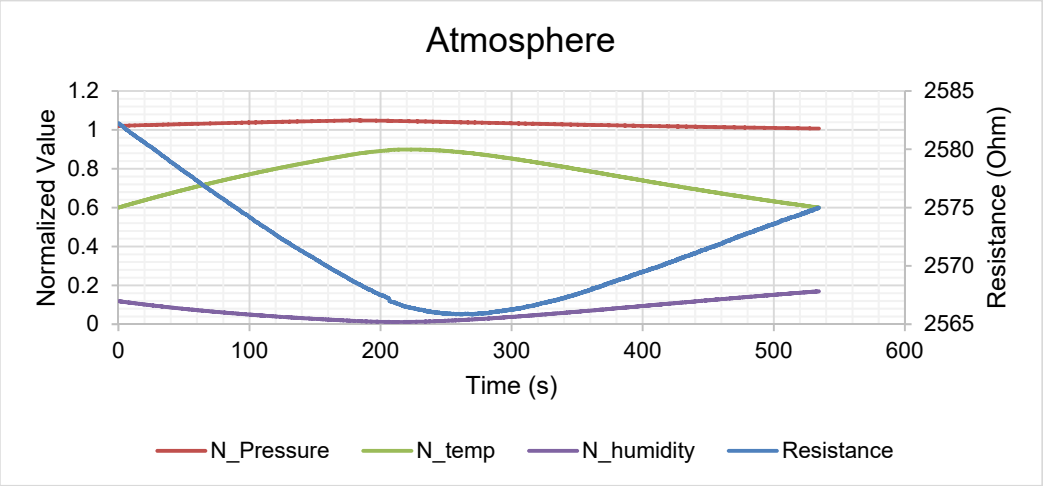

Figure 47: Time-domain response of the resistance, normalized temperature, normalized pressure and normalized humidity when the chamber is filled with atmospheric gas

Take note that the initial heat-up with NO_2 in the chamber is observed to be slightly slower, as this was done at a slightly lower power setting. However, the overall sweep was still carried out over approximately the same range of temperature and humidity. The data obtained was plotted as another scatter plot to observe the effect of NO_2 on the sensor's resistance.

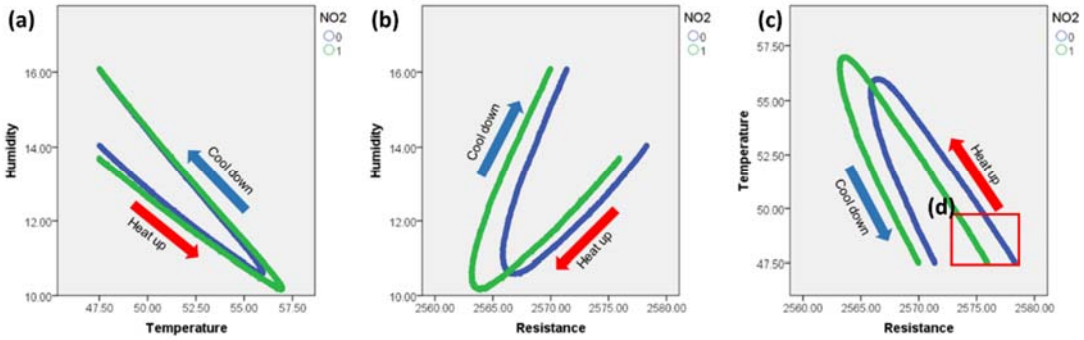

Figure 48: Scatterplot of the experimental parameters: (a) humidity-temperature, (b) humidity-resistance, (c) temperature-resistance, (d) linear part of graph sampled for further analysis. The green line indicates 10ppm NO_2 in the chamber and the blue line indicates ambient atmospheric gas.

From the figure above, we can see that the humidity level and temperature level are clearly overlapping, showing similar conditions for both measurement rounds. There is a noticeable hysteresis in the measurement, with a higher relative humidity value measured after the heat up process. However, after purging, the value dropped back to normal. This

could be attributed to the increase in temperature of the walls on the steel body. Since the heater is not heating the air directly, but rather, doing so through the body of the chamber, the increased temperature of the chamber walls could be much higher than the measured temperature near the NC-graphite strip. Therefore, some pre-adsorbed moisture on the chamber walls could be liberated. During the purging cycle, the introduction of cooler air may reduce the temperature of the chamber walls to enable re-adsorption of water molecules, thus, resulting in the same hysteresis effect in both NO_2 and atmospheric measurements.

Nonetheless, the introduction of NO_2 shows a consistent shift towards the left side of the graph in the resistance-humidity plot and the resistance-temperature plot. This indicates a lower resistance for strips exposed to NO_2 at the same temperature and humidity. To estimate the contribution of relative humidity and temperature to the resistance, the linear part of Figure 48(c)(inset) is extracted as shown in Figure 49.

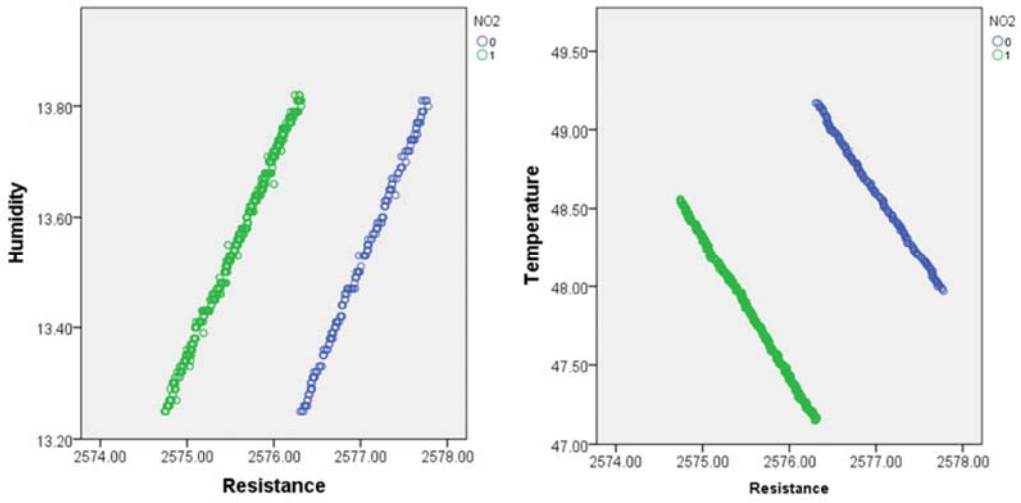

Figure 49: Linear part of humidity-resistance and temperature resistance graph during cool down cycle

The resistance of the sensor decreased upon exposure to 10 ppm of NO_2 by 1.6 Ohms. The overall percentage change is 0.062%. It is worth noting that the magnitude of change in resistance due to the variations of relative humidity is way larger than the change contributed by NO_2.

5.3 Multi-gas characterization (Malaysia)

The devices fabricated in the UK were brought back to Malaysia for another series of calibration. Based on the results obtained in the UK, another set of NO_2 experiment was done in the Malaysia campus. For this experiment, a much thinner strip was used (B03W02, 34 nm).

5.3.1 NO_2 sensing test

The basic setup of the system was described in Figure 41. The experiment was done with 25 minutes of vacuum baseline measurement, 25 minutes of N_2 baseline measurement, followed by a pulse of 10 ppm NO_2/N_2 mixture (See Figure 50).

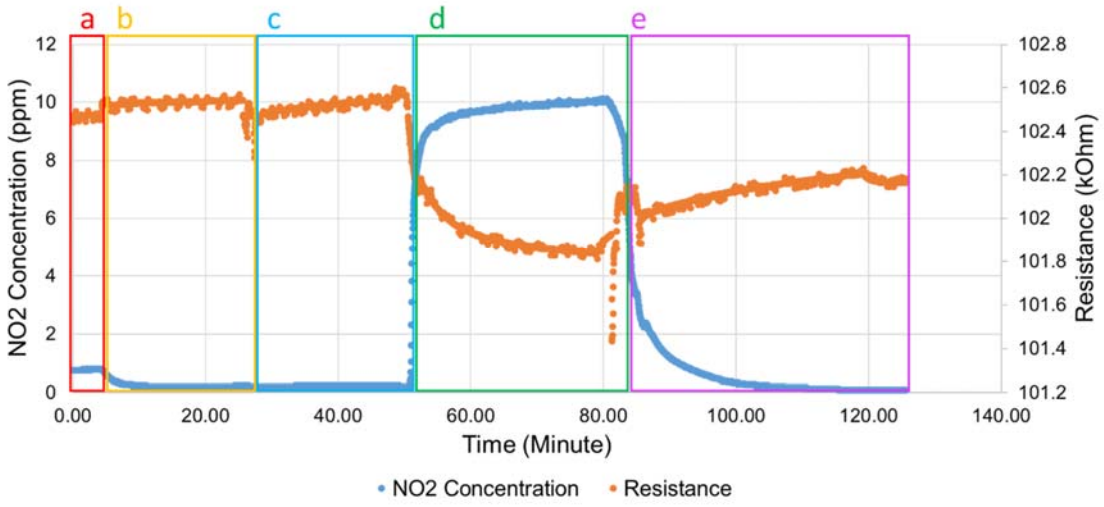

Figure 50: Time domain signal of measured NO_2 concentration from Grove multigas sensor and measured resistance of the NCG strip (B03W02). Blue line corresponds to NO_2 concentration while the orange line corresponds to the measured resistance. (a) Baseline measurement at atmosphere. (b) Baseline measurement in vacuum. (7.5 kPa / 0.075 bar) (c) Baseline measurement in N_2 atmospheric pressure. (d) Measurement of NO_2 exposure at atmospheric pressure. (e) Sensor recovery in N_2 at atmospheric pressure.

The measurement period for (b) and (c) is 25 minutes, while the measurement period for (d) is approximately 35 minutes to allow the sensor to reach a steady state value. After flushing the chamber with N_2 at the end of the experiment, the readings were taken for a period of 40 minutes. From (a) to (b), the resistance increases slightly (by 0.07%) due to the removal of atmospheric gases from the chamber. The resistance stays relatively unchanged

between the vacuum measurement (7.5 kPa / 0.075 bar) to the N_2 baseline measurement (101.3 kPa / 1.013 bar). This validates the preliminary result obtained in the UK which suggests that the resistance of the strip does not vary with pressure, and that the variation was a result of humidity difference at different pressures.

When NO_2 was introduced to the system, a significant drop in resistance is observed. The resistance difference between the average resistance measured at vacuum baseline and the average steady state resistance at 10 ppm exposure is calculated as shown:

$$\Delta R = R_{baseline} - R_{NO2} = 101851\Omega - 102531\Omega = -680\,\Omega \text{ ------ Eq. 17}$$

$$Percentage\ Change = \frac{\Delta R}{R_{baseline}} \times 100\% = -0.663\% \text{ ------ Eq. 18}$$

The recovery of the sensor appears to be significantly slower than its response time. This can be attributed to the strong interaction between the NCG film and the adsorbed NO_2 molecules. The magnitude and percentage change of this strip (B03W02, 34 nm) upon exposure to 10 ppm of NO_2 is significantly higher than the ones measured in the UK (303 nm, B03W04), which indicates a greater sensitivity for thinner sensor strips.

The fluctuations seen between (d) and (e) can be attributed to the purging cycle of the gas chamber, where the chamber was evacuated to vacuum and filled with N_2. The purging cycle was repeated 3 times, resulting in a rapid decrease in NO_2 concentration. A slight fluctuation could also be observed on the response of the reference NO_2 sensor.

5.3.2 CO sensing test

A quicker CO test was done to determine the effect of CO on the sensor. The setup is similar to the previous section. However, vacuum to N_2 tests are not shown here for brevity. Due to the absence of a reliable CO reference sensor, the chamber was evacuated before CO was introduced to ensure that the internal volume of the gas chamber is filled up with 10ppm CO with N_2 balance.

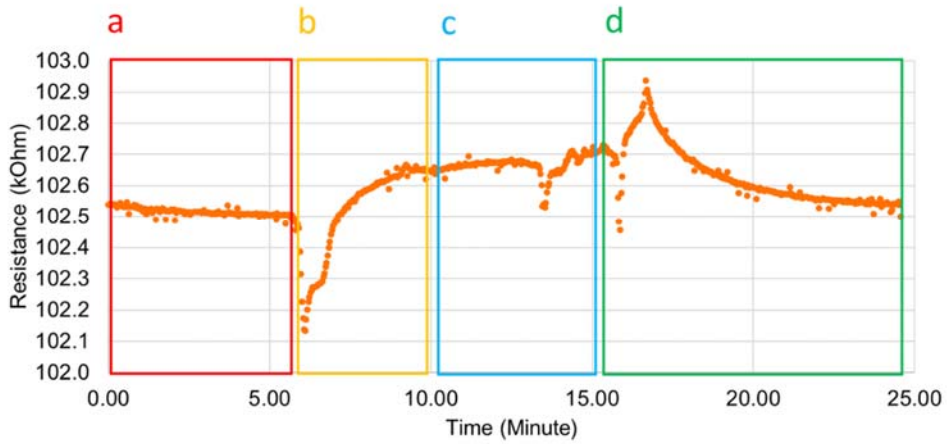

Figure 51: Time domain signal of measured resistance of the NCG strip (B03W02) with 10ppm of CO added. (a) Baseline measurement in N_2 at atmospheric pressure. (b) Chamber evacuate until 10 kPa, and switchover to CO flow at 10 sccm. (c) CO flow is stopped. Measurement of 10 ppm CO exposure at atmospheric pressure. (d) Sensor recovery in N_2 at atmospheric pressure

The measurement period between (b) and (c) only takes 10 minutes as the flow of CO is stopped when the signal appears to reach a steady state. The fluctuations at the end of C are artefacts caused by multiple quick vacuum-N_2 flush cycle to remove CO before being pumped back to atmospheric pressure for sensor recovery.

Upon exposure to CO, the sensor experiences a slight rise in resistance, which could be attributed to the slight reducing properties of CO. The presence of CO could liberate surface oxygen previously adsorbed on the film due to atmospheric exposure, as CO reacts with oxygen species to form CO_2. The magnitude of resistance change due to CO is lower than that of NO_2. The resistance difference between the average resistance measured at vacuum baseline and the average steady state resistance at 10 ppm exposure is calculated as shown:

$$\Delta R = R_{CO} - R_{baseline} = 102652\Omega - 102509\Omega = 143\ \Omega \text{ ------ Eq. 19}$$

$$Percentage\ Change = \frac{\Delta R}{R_{baseline}} \times 100\% = 0.14\% \text{ ------ Eq. 20}$$

The recovery of the sensor appears to be faster for CO when compared to NO_2 exposure. This could indicate weaker chemical interaction between CO and the NCG film.

5.3.3 NH_3 sensing test

The same method described above was repeated for NH_3, which is a known reducing gas to verify the observations made (See Figure 52).

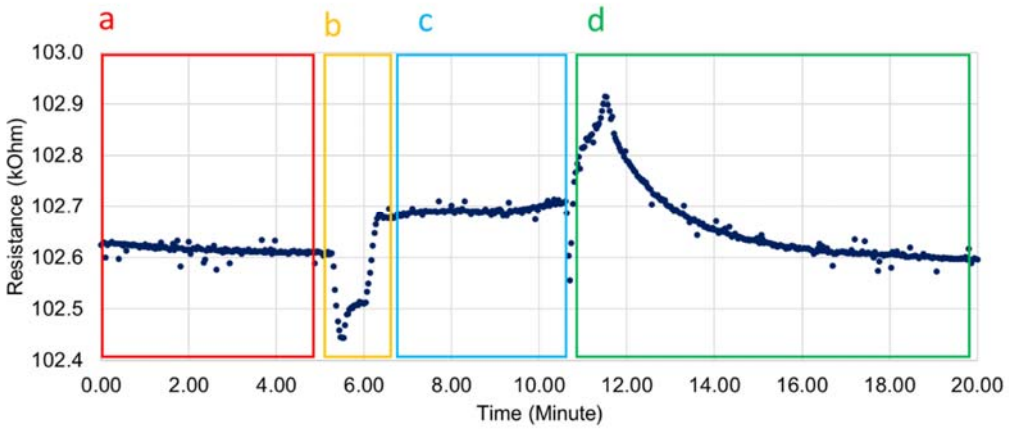

Figure 52: Time domain signal of measured resistance of the NCG strip (B03W02) with 10ppm of NH_3 added (a) Baseline measurement in N_2 at atmospheric pressure. (b) Chamber evacuate until 10 kPa, and switchover to NH_3 flow at 10 sccm. (c) NH_3 flow is stopped. Measurement of 10 ppm NH_3 exposure at atmospheric pressure. (d) Sensor recovery in N_2 at atmospheric pressure

The resistance difference between the average resistance measured at vacuum baseline and the average steady state resistance at 10 ppm exposure is calculated as shown:

$$\Delta R = R_{NH3} - R_{baseline} = 102716\Omega - 102613\Omega = 103\ \Omega \text{ ------ Eq. 21}$$

$$Percentage\ Change = \frac{\Delta R}{R_{baseline}} \times 100\% = 0.1\% \text{ ------ Eq. 22}$$

The recovery time for NH_3 exposure appears to be like that of CO, however, the magnitude of response for both CO and NH_3 are less than that of NO_2. This agrees with previous work done by [5], [51], [64], [152] which suggests that ammonia (NH_3) is a weak electron donor, forming a more energetically favourable ammonium (NH_4) upon interaction with the sensing layer. The protonation of NH_3 could happen in hydrogen vacancies at the defective site of the NCG film.

5.4 Discussions

5.4.1 Surface adsorption model of NCG

Due to the porous structure of the NCG film (See Section 4.7), gas molecules are adsorbed around the pore space around the grains. Specific gases will adsorb into the amorphous carbon surrounding the crystalline grains, and thus, modulating the resistance of the amorphous regions, which forms the active sensing site of the NCG film.

For the gas sensing tests, the measurements were done in a no-flow environment, hence, the average resistance reading was only taken during the steady state. If the gas adsorption on the is mainly due to chemisorption (Langmuir adsorption) and is non-dissociative in nature, the rate of adsorption per effective coverage area (C_a) of the said gas on the NCG film can be expressed as:

$$\frac{dN_{ads}(t)}{C_a \cdot dt} = \frac{SP_{partial}}{\sqrt{2\pi mRT}} \text{ ------ Eq. 23}$$

where S is the sticking probability of the molecule upon striking the NCG film, $P_{partial}$ is the partial pressure of NO_2, m is the molar mass of the adsorbate gas, R is the ideal gas constant, and T is the temperature in kelvins [153]. In this model, the gas permeability of the NCG is ignored, as gas permeation into the bulk of the film would be treated as an increase in the effective surface area of the film.

An interesting parameter to be considered is S which governs the probability of each collision event to result in a successful adsorption. The sticking probability is a function of surface coverage, i.e. the percentage of NCG surface covered with gas molecules (θ).

$$S \cong S_o(1-\theta) \text{ ------ Eq. 24}$$

Since the concentration of NO_2 is kept in the ppm range, θ is kept at a relatively small value, hence $S \approx S_o$. The partial pressure of NO_2 is a function of the total pressure in the chamber and the fraction of NO_2 present in the chamber, $P_{partial} = P_{total} * C(t)$, where C(t) is the concentration of NO_2 in the chamber. Equation 23 can then be simplified as:

$$\frac{dN_{ads}(t)}{C_a \cdot dt} = \alpha C(t), \alpha = \frac{S_o P_{total}}{\sqrt{2\pi mRT}} \text{ ------ Eq. 25}$$

To study the number of adsorbed molecules on the sensor surface, one must also consider the rate at which the molecule desorbs from the surface by considering the Arrhenius form of the desorption equation:

$$\frac{dN_{des}(t)}{C_a \cdot dt} = N_{surface}(t) \cdot ve^{-\frac{E_a}{RT}} \text{ ------ Eq. 26}$$

where v denotes the pre-exponential factor, which contains information about the frequency of attempted desorption by the molecule, while E_a denotes the activation energy of the adsorption and $N_{surface}$ is the number of molecules currently adsorbed on the surface of the sensor. E_a for the interaction between NCG and NO_2 can be obtained using ab initio simulations [79]. Simplifying the equation, we obtain:

$$\frac{dN_{des}(t)}{C_a \cdot dt} = \beta \cdot N_{surface}(t), \quad \beta = ve^{-\frac{E_a}{RT}} \text{ ------ Eq. 27}$$

The rate of change of molecules adsorbed can then be expressed as:

$$\frac{dN_{surface}(t)}{C_a \cdot dt} = \frac{dN_{ads}(t)}{C_a \cdot dt} - \frac{dN_{des}(t)}{C_a \cdot dt} \text{ ------ Eq. 28}$$

$$\frac{dN_{surface}(t)}{C_a \cdot dt} = \alpha C(t) - \beta \cdot N_{surface}(t) \text{ ------ Eq. 29}$$

which can be solved using Laplace transform:

$$\frac{1}{C_a} sN_{surface}(S) - N_{surface}(0) = \alpha C(S) - \beta \cdot N_{surface}(S) \text{ ------ Eq. 30}$$

$$\frac{N_{surface}(s)}{C(s)} = \frac{C_a \alpha}{s + C_a \beta} \text{ ------ Eq. 31}$$

$$N_{surface}(t) = C(t) \cdot \alpha C_a e^{-\beta C_a} \text{ ------ Eq. 32}$$

If the number of molecules adsorbed on the surface of the film affects the majority carrier of the film, the relationship between the resistance of the film and the number of adsorbed particles can be investigated by considering the resistance model of the NCG film.

5.4.2 Resistance model of NCG

The NCG is a polycrystalline film, hence the resistance across the film is not homogenous. The resistance of NCG consists of two components, one corresponding to amorphous material and the other crystalline material, as shown in Section 4.5 and Section 4.7. The crystalline areas of the NCG generally has a much lower resistance due to the presence of delocalized pi electrons. The amorphous part of the film is a mix of sp^2 and sp^3 bonds. The ability of the amorphous carbon to conduct is highly dependent on the availability

of pi electrons in the sp^2 bonds. In regions where sp^3 bonds are formed, electrons are usually trapped in strong sigma bonds, with does not allow for conduction. The porous nature of the film allows gases to be absorbed into the film through voids formed due to the irregular shape of the nanocrystals. The gas will then be adsorbed onto the porous structure of the amorphous carbon surrounding the nanocrystals. Theses amorphous carbon region is thought to act as the active sensing site for the NCG film, as NO_2, NH_3 and CO adsorb favourably on defect sites when compared to pristine graphene/graphite surfaces [79]. The graphite nanocrystals merely provide a high conductivity path for the current to pass through and does not contribute actively to the sensing mechanism.

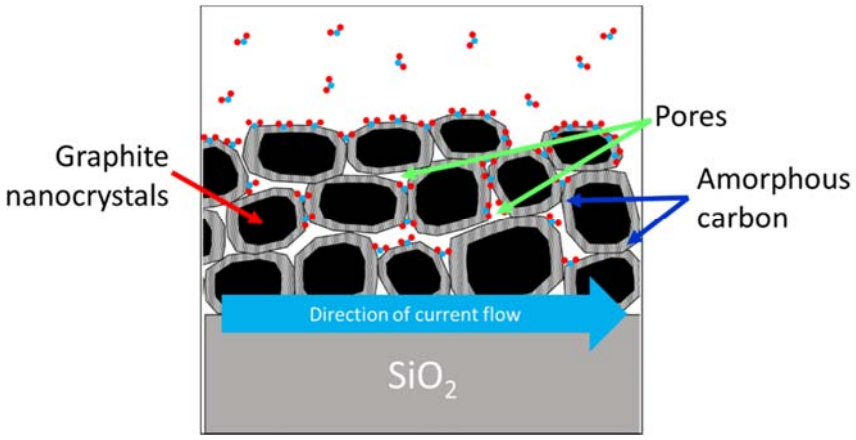

Figure 53: Illustration of gas adsorption and carrier enhancement on the NCG film. Grey areas denote region with amorphous carbon while black area denotes graphitic crystals. The illustration is not drawn to scale.

To model the resistance of the NCG strip, both the injection mechanism and the conduction mechanism must be taken into consideration. Between the metal contact and the NCG film, the injection mechanism could be a Schottky contact or an Ohmic contact. However, as demonstrated in Section 4.8, the contact characteristic of the NCG strip is mainly Ohmic, thus allowing us to model the contact resistances as series resistors (Refer to Figure 34). Due to the crystalline nature of the graphitic nanocrystals, the predominant bulk conduction mechanism should be Ohmic. However, for the amorphous carbon, the conduction mechanism could be Ohmic conduction if the proportion of sp^2 bonds in the amorphous region is higher, or due to the Poole-Frenkel effect if the proportion of sp^3 bonds is higher [154]. In a Poole-Frenkel type conduction, the trapped electrons occasionally gain enough energy through thermal fluctuation, allowing it to move a short distance before settling into another localized state. In the presence of an electric field, this will allow the charge carrier to move in the direction of the electric field, albeit slowly [155].

The amorphous region of the film which is formed between the nanocrystals can be thought of as defects which introduces charge traps in the film. These charge traps creates localized states for electrons [156]. At room temperature, some of the trapped electrons gained enough energy to break free from the localized state through Poole-Frenkel effect, thus creating a "hole" capable of trapping another electron. This creates an apparent p-type semiconducting behaviour, over the usual metallic conduction mechanism of graphite. In other words, the defects in the amorphous region of the NCG film acts as a sort of quasi-dopant, creating a p-type-like semiconducting behaviour. The p-type-like conduction of NCG is observed in Section 4.4, where the Hall effect characterization shows holes as the majority charge carrier.

Therefore, the NCG film can be modelled as a p-type like semiconducting film and on gas adsorption will follow a charge transfer type mechanism as briefly described in section 2.1.3. The measured resistance of the NCG film can be represented as follow:

$$R_{total} = R_{contact} + R_{exposed} + R_o \text{ ------ Eq. 33}$$

where $R_{contact}$ is the contact resistance of the strip, $R_{exposed}$ is the resistance of the region of the film exposed to the analyte gas and is affected by the gas permeability of the film, and R_o is the resistance of the area in the film which is not exposed to the analyte gas.

When the NCG strip is exposed to the gas, $R_{exposed}$ will be modulated. The change in resistance is attributed to the change in resistivity, as opposed to a change in the film's dimension.

$$R_{exposed} = \rho\gamma\,, \gamma = \frac{L}{A} \text{ ------ Eq. 34}$$

where ρ represents the resistivity of the exposed area of the film, and γ denotes the geometrical constant of the exposed region, which is affected by the gas permeability of the film due to pores, as well as the geometrical dimensions of the NCG film, as the film is porous [157]. If the exposed region remains unchanged, then, ρ will be modulated upon gas adsorption due to the charge transfer between the gas molecules and the NCG film. The resistivity of $R_{exposed}$ can be modelled as the inverse of the conductivity as shown:

$$\rho = \frac{1}{\sigma} = \frac{1}{q(\mu_p n_{total})} \text{------ Eq. 35}$$

where q is the magnitude of the elemental charge, μ_p is the mobility of the holes (the dominant carrier), and n_{total} is the total carrier concentration in the NCG film. Upon interaction with the redox gas, the carrier concentration is changed. Therefore, an additional

term, n_d was added to represent the carrier modulation facilitated by the gas adsorption. The total carrier of the film's active region can then be represented as:

$$n_{total} = n_p + n_d \text{------ Eq. 36}$$

where n_p represents the number of holes (positive charge carrier), and n_d is the number of the donated carrier. The sign for n_d is positive if electrons is being taken away from the material, and negative if electron is being donated to the material. The relationship between the number of electrons donated or taken away from the material is, again, proportional to the number of gas molecule adsorbed on the gas sensor, hence, the number of donated carriers at any given time can be represented as:

$$n_d = \kappa N_{surface}(t) = \kappa\{C(t) \cdot \alpha C_a e^{-\beta C_a}\} \text{ ------ Eq. 37}$$

where κ is a constant which contains information on the amount of charge carrier donated per molecule adsorbed, and the type of carrier. The value of κ can be estimated by first principle simulation reported by [79], [158]. It is believed that the gas adsorption happens predominantly on the defective areas of the film, as suggested by [79]. Therefore, the charge transfer mechanism is thought to happen predominantly on the amorphous region where trapped charge is thought to contribute to the film's p-type semiconducting behaviour. In the resistance model, the constant term R_o was introduced to represent the regions impermeable to the gas, hence, does not experience any changes in resistances.

The overall model for the resistance changes due to gas exposure can be summarized as shown:

$$\mathrm{R_{total}(t)} = \mathrm{R_{contact}} + \mathrm{R_o} + \frac{\gamma}{q\mu_p\left(n_p + \kappa\{C(t)\cdot\alpha C_a e^{-\beta C_a}\}\right)} \text{ ------ Eq. 38}$$

$R_{contact}$ and R_o is believed to be constant, while the resistance across the amorphous regions of the film is thought to change upon adsorption of gas molecules.

The number of charge carriers available for conduction in the film is being modulated by the adsorbed gas. Within the context of this standard charge transfer model, the results presented above for gas adsorption can be explained. A further explanation of the charge transfer model for each of the analyte gases is presented in section 5.4.3.

5.4.3 Overview of the gas sensing performance of NCG

Here, the change in resistance of NCG film upon exposure to different gases were investigated. The resistance of the NCG film decreases upon exposure to NO_2, and increases

upon exposure to NH_3 and CO. The NCG film also shows slightly stronger response to NO_2 (0.6% change) compared to NH_3 (0.1% change) and CO (0.14% change). This result agrees with previously reported work of p-type-like semiconducting sensors [10], [83], [86], [87], [89], [91], [92], [152]. The result also agrees with first principle simulations on defected [79] and pristine [158] graphene, which predicts similar sensing response towards NO_2 and NH_3.

5.4.3.1 Response towards NO_2

Simulations of NO_2 adsorption on graphitic crystals shows strong evidence of electron acceptance by the adsorbed NO_2. This result is consistent for both pristine [158] and defective [79] forms of graphitic crystals. In the case of NCG, where a P-type conduction mechanism is observed, the adsorption of NO_2 on the film will result in an increase of holes for P-type conduction. Thus, the measured resistance of the film will decrease.

First principle simulations report strong charge acceptance behaviour in NO_2 with -0.1*e* reported for pristine graphene [158] and -0.19*e* reported for defective graphene [79]. This is consistent with our reported results, which shows a larger percentage of change with NO_2 when compared to NH_3 or CO. The reduction of NCG's resistance upon exposure to NO_2 is also consistent with the simulated results.

5.4.3.2 Response towards CO and NH_3

Both CO and NH_3 shows small charge donation towards the graphitic film in simulations. The average charge transfer for NH_3 is 0.027*e* [158] on pristine graphene and 0.020*e* on defective graphene [79]. On the other hand, CO shows a larger charge transfer on defective graphene (0.260 *e*) [79] when compared to pristine graphene (0.012 *e*) [158].

From the experiments, the magnitude of resistance increases experienced by the film upon exposure to CO (0.14%) and NH_3 (0.10%) is similar. This could be attributed to the fact that NCG is a mixture of amorphous carbon with high defect density and graphitic nanocrystals. As CO is thought to donate more charge at defective regions, the net effect of charge donation may be comparable to NH_3 which has a similar charge transfer magnitude for both defective and crystalline graphene.

5.4.3.3 Response towards H_2O

During the gas sensing experiments, NCG was observed to respond much more strongly to relative humidity. Due to the preferential response of the gas sensors towards humidity, work has been done to evaluate the performance of the NCG sensor as a possible

humidity sensor in Chapter 6. However, the response of NCG towards redox species is not to be ignored, despite having a much smaller magnitude of change. Data obtained from this work could be expanded further to exploit the possibility of using NCG as redox gas sensors in environments where humidity is negligible. Future iterations of the work could also investigate other methods to enhance the sensitivity of the sensor as a redox gas sensor while keeping water vapour away from the sensor's surface.

Chapter 6: Humidity Sensing with NCG Films

Part of this work was published as "Sensing performance of Nanocrystalline Graphite Based Humidity Sensors" in IEEE Sensors Journal. In this chapter, the humidity sensing performance of NCG is investigated. It was established in Chapter 5 that the magnitude of response to humidity is at least an order of magnitude higher than redox gasses at atmospheric condition. Here, we report for the first time, the humidity sensing performance of PECVD NCG films with various geometrical parameters. The sensing mechanism for water vapour is found to be different from that reported in Chapter 5.

6.1 Humidity sensing performance of NCG

6.1.1 Methodology

The fabricated chip (1cm x 1cm) was diced and assembled onto a PCB. The naming convention used, and the geometrical dimensions of the devices are summarized in Table 8 while images of the devices taken on an optical microscope are shown in Figure 54. The chip was connected to the PCB through aluminium wire bonding. The gas sensor PCB was then assembled onto the gas sensing rig via pin headers. The experiment was divided into 3 sets, which aims to test the effect of the device's width, thickness and exposed edge on the overall sensing performance of the sensor. For each set of experiments, different devices were used.

Table 8: Description of Devices

Device ID	Geometrical Dimensions			Description
	Width	Length	Thickness	
100_3_30_Str	100 µm	3 mm	30 nm	Straight strips
300_3_30_Str	300 µm	3 mm	30 nm	Straight strips
500_3_30_Str	500 µm	3 mm	30 nm	Straight strips
10_20_30_Mdr	10 µm	20 mm	30 nm	Meandered strips
10_20_300_Mdr	10 µm	20 mm	300 nm	Meandered strips
150_3_300_Str	150 µm	3 mm	300 nm	Straight strips
150_3_300_Arr	50 µm x 3	3 mm	300 nm	Array strips with same top surface area.

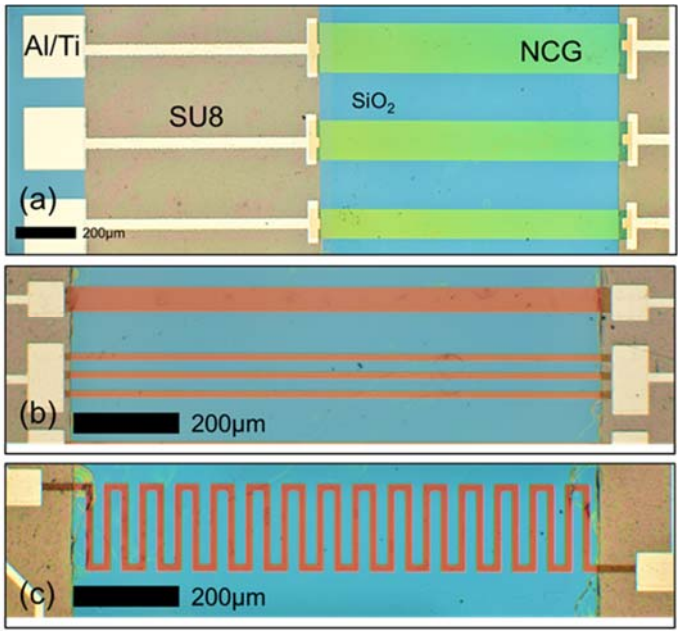

Figure 54: Optical microscope image of the strips used for testing. (a) 300_3_30_Str (Bottom), 400_3_30_Str (Middle, Unused) and 500_3_30_Str (Top). (b) Single and arrayed NCG Strips 150_3_300_Str (Top) and 150_3_300_Arr (Bottom) (c) Optical Microscope image of 10_20_300_Mdr : Meandered strip

The gas sensor test chamber in Figure 43 was modified to work as a humidity test chamber. The relative humidity of the gas chamber was increased by introducing water vapour through a commercial ultrasonic humidifier filled with deionized water. The modified humidity test chamber is shown in Figure 55.

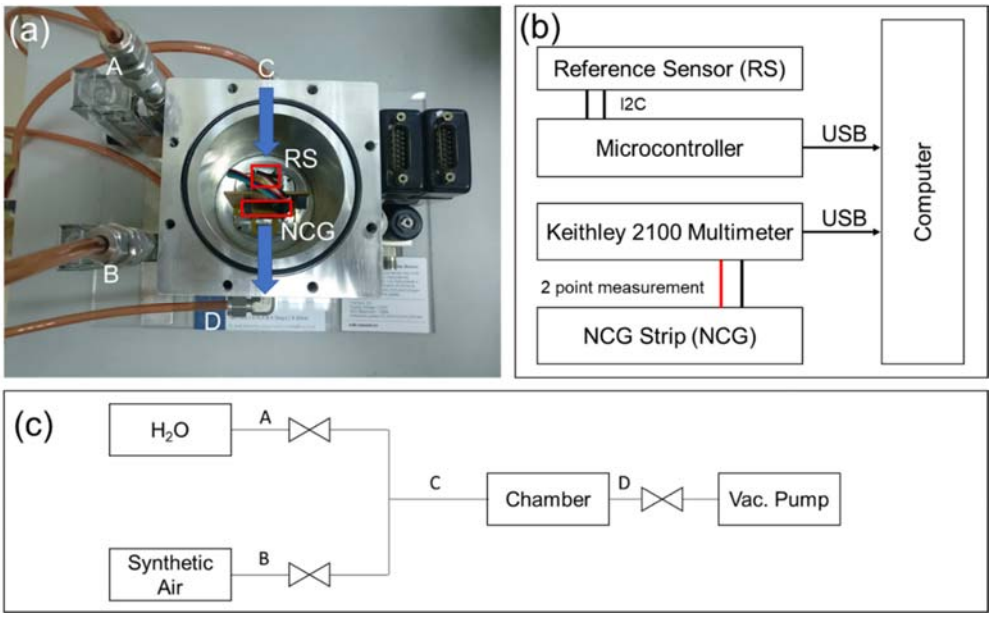

Figure 55: (a) Humidity testing setup. Blue arrows on the picture shows the direction of gas flow in the chamber. The cover of the chamber is removed for clarity. (b) electrical connection of the setup, (c) block diagram of the humidity test system

At the beginning of each measurement cycle, the humidity of the chamber was lowered to 40% RH using 20 g of silica gel (Hannschweiller Chemicals GmbH) as desiccant. Synthetic air (Calgaz, 20% O2 in N2 balance, Relative humidity < 25% RH) was used to remove excessive moisture if necessary. Due to the limitation of the setup, only relative humidity ranges between 40% RH – 90% RH could be measured. At relative humidity levels above 90% RH, water starts condensing within the chamber, and risk damaging the internal sensors.

Humidity was increased by feeding water vapour created from the humidifier into the chamber for 3 seconds. After that, the chamber was sealed, and resistance was logged every 2 seconds using a Keithley 2100 high precision multimeter. A 30-minute delay was introduced after each humidity pulse for sensor signal stabilization. An additional measurement cycle was carried out using a vacuum pump on a sealed chamber to establish the relationship between the sensor's resistance and the relative humidity of its environment at lower% RH values. The chamber was pumped down from 101.3 kPa (1 atm) to 2 kPa (0.0197 atm) and the humidity was increased by introducing atmospheric air. To verify that the effect of measurement is from the NCG film, and not the metal contacts, a set of NCG films with similar geometrical dimensions were fabricated and covered entirely with SU8. Tests on these devices shows no response to change in humidity.

6.1.2 Results and discussion

6.1.2.1 Resistance change due to humidity variation

The sensor shows obvious reduction in resistance upon exposure to higher relative humidity. The step-like response for the sensor (10_20_300_Mdr) is shown in Figure 56. At target relative humidity higher than 90%, water starts to condense on the viewing window and the sensor's surface, causing a drastic drop in resistance. During the vacuum – ambient pressure cycling, the resistance shows high repeatability across all 4 measurement cycles.

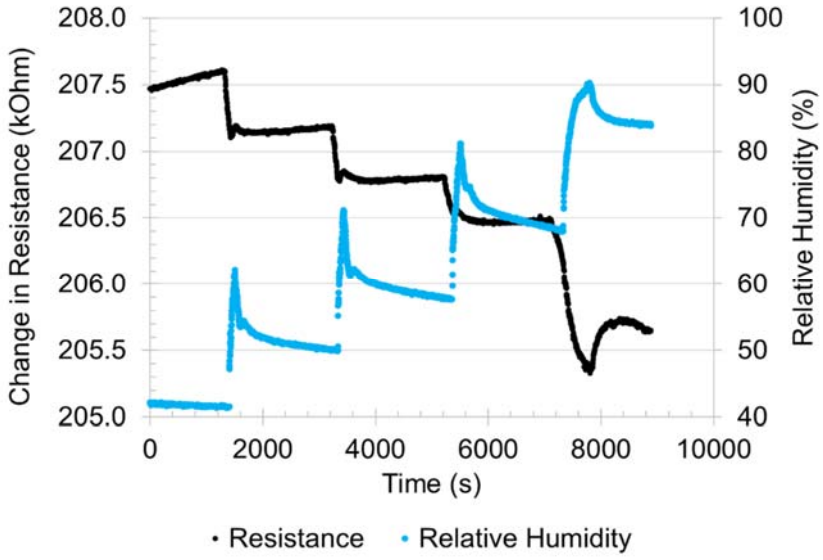

Figure 56: Response of sensor (10_20_300_Mdr) to different values of relative humidity steps

The spikes seen on the humidity-time plot are a consequence of the sensor placement. As the reference sensor is exposed to the inflow of humid air, it will experience a spike when the air is being pumped into the chamber and stabilizes as the air flow is stopped. Figure 57 shows the vacuum to ambient pressure cycle to obtain lower humidity level readings. Vacuum-ambient cycle was undertaken because it allows for faster data collection, as opposed to using silica gel desiccants.

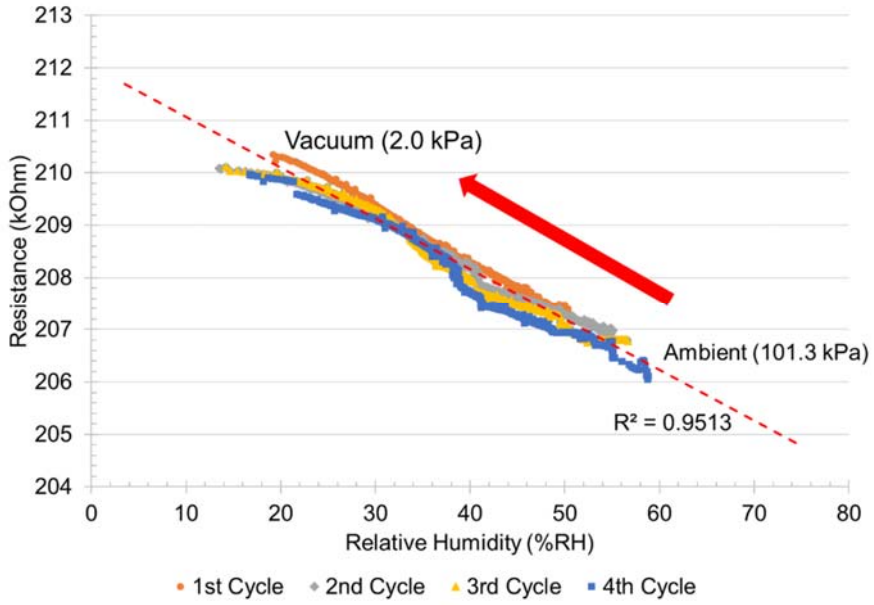

Figure 57: Resistance as a function of relative humidity, taken as an aggregate of 4 vacuum-ambient measurement cycles from 10_20_300_Mdr

An experiment done in section 6.3.2 indicates that the NCG film has negligible response to pressure. Statistical values from Figure 56 and Figure 57 are used to determine the average resistance at any given relative humidity, and is plotted in Figure 58.

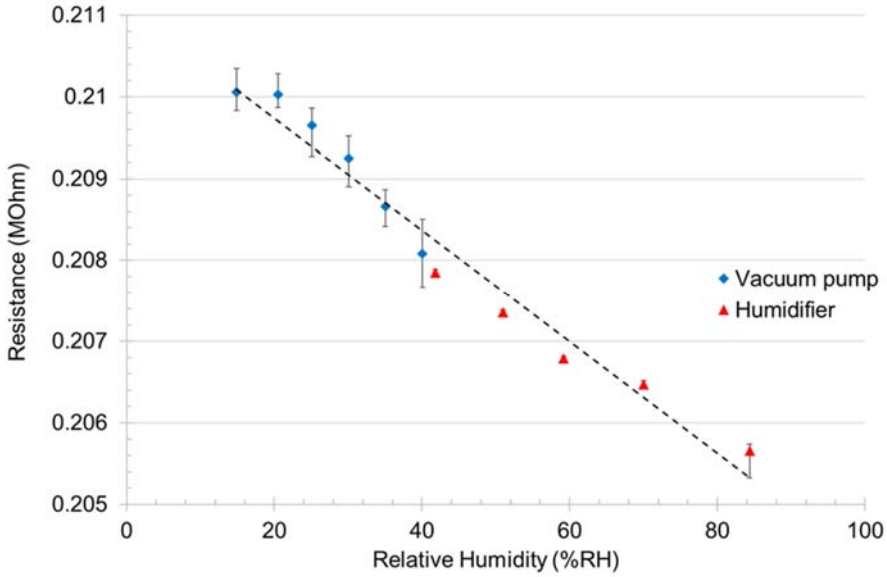

Figure 58: Resistance of NCG meandering strip (10_20_300_Mdr) as a function of humidity

The NCG strip shows a linear change in resistance in response to the change in relative humidity. The larger errors in the lower humidity range is a consequence of using a vacuum pump.

6.2 Effects of geometrical dimensions on sensing capabilities

6.2.1 Effect of varying widths to the sensitivity

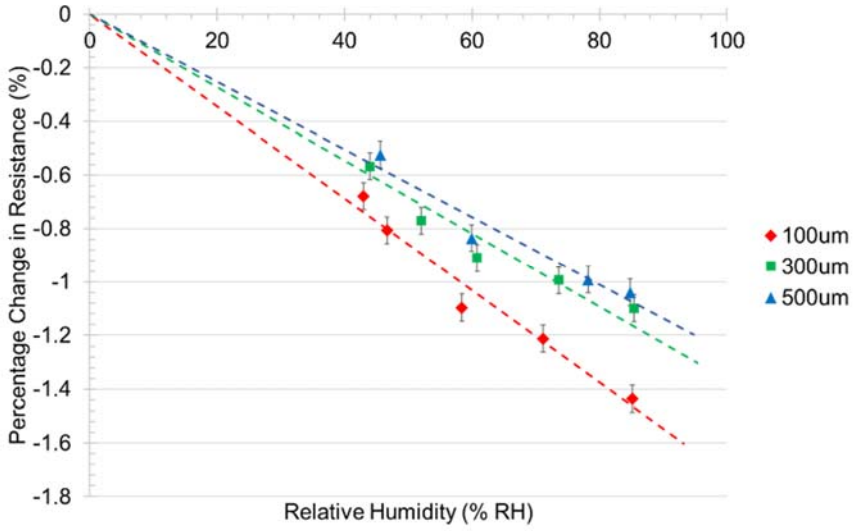

Figure 59: Percentage change in resistance of the sensor as a function of relative humidity for devices of different widths but same thickness and length. Thickness = 30nm, length = 3mm. The optical microscope image of the strips used is shown in Figure 54(a).

Figure 59 shows the percentage of change in the sensor's resistance as a function of the change in humidity for different sensor widths. Each data point is extracted from the steady state reading of the NCG sensors at the relative humidity level. In the case of NCG, the effect seems to be anisotropic. An increase in the width of the strips appears to cause a decrease in the percentage of response. However, in the wider strips (300 µm and 500 µm), the change in thickness doesn't cause much differences in the percentage of change. The magnitude of resistance change is also dependant on the width of the strip. The magnitude of resistance changes for the 100 µm strip (ΔR = -17.14Ω/%RH) is significantly higher than the magnitude of resistance changes for the 300 µm (ΔR = -4.32Ω/%RH) and 500 µm (ΔR = -2.48Ω/%RH) strips.

6.2.2 Effect of thickness on the sensitivity

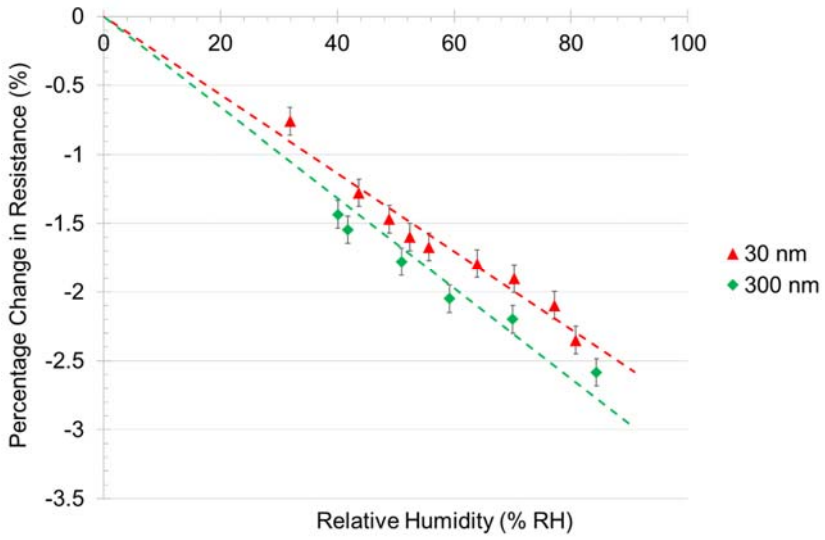

Figure 60: Percentage change in resistance of the sensor as a function of relative humidity for devices of thickness, with the same width and length. Width = 10 μm, length = 20 mm (Meandered strips).

Figure 60 shows the percentage of change in the sensor's resistance as a function of the change in humidity for different sensor thickness. As narrower and longer strips are predicted to have better sensing performance, a long meandering design was used (Figure 54(c)). Two devices with the same width and length, but a different thickness, were tested. For the same top surface exposed, the thicker strip experiences a slightly higher percentage change in resistance. Note that these devices are meandered strips, hence, the higher percentage of change in comparison to the straight strips can be attributed to the longer and narrower structure of the device. However, the thinner strip experiences a much higher magnitude of resistance change (ΔR = -280.76Ω/%RH) compared to the thicker strip (ΔR = -64.16Ω/%RH).

6.2.3 Effect of the number of sidewalls on sensitivity

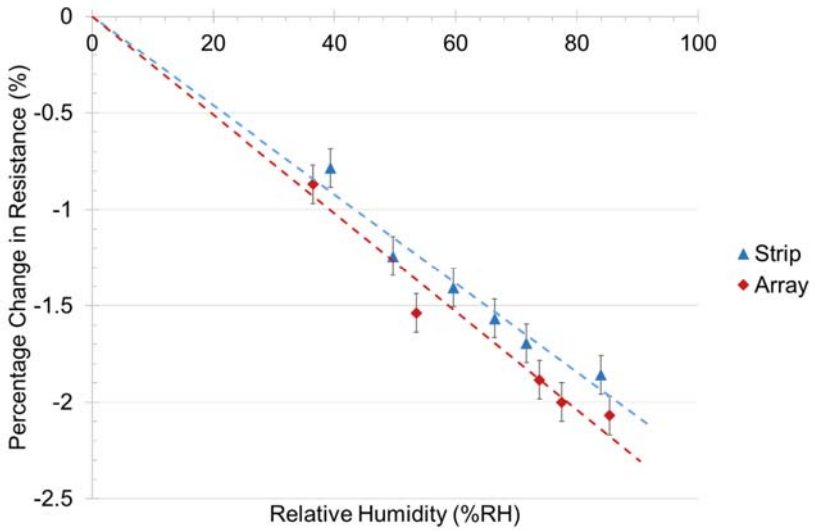

Figure 61: Percentage of change in conductance in strips as a function of relative humidity for devices with the same total top surface area, but different amount of side walls exposed. Thickness = 300 nm, length = 3 mm, width = 150 µm (Strip) & 50µm x 3 (Arrays)

Figure 61 shows the percentage of change in the sensor's resistance as a function of the change in humidity for sensor strips or arrays with similar top surface area. There appear to be no significant differences in the performance of the sensor. The slightly higher percentage of change in the array could be attributed to the differences in dimensions during fabrication. The magnitude of resistance change for both devices are similar (Array ΔR = -3.21 Ω/%RH; Strip ΔR = -3.58 Ω/%RH).

6.3 Effects of other environmental variables on NCG sensors

6.3.1 Random multivariate sweep test

To isolate the effects of temperature, pressure and humidity on the NCG strip, a random multivariate sweep was done. For this experiment, extra humidity was introduced into the chamber by pumping vapor out of an enclosed airspace filled with water from T = 25s to T = 70s and from T = 230s to T = 270s whilst maintaining the same pressure and temperature (Refer to Figure 62). This is essential, because the reference sensor reports the relative humidity reading, which is a function of the concentration of water vapor, temperature and pressure. Due to this, any direct measurement of parameters will not be an accurate picture of the sensor's response as the inputs are correlated with one another.

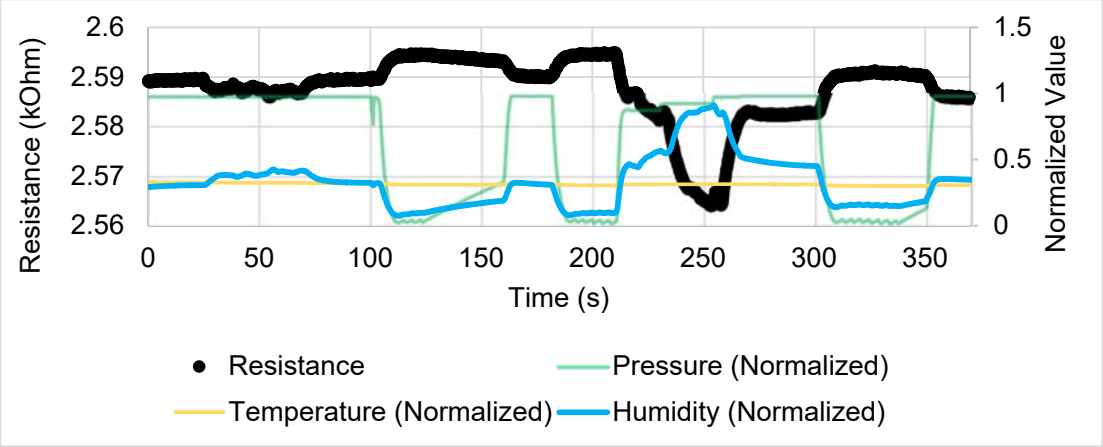

Figure 62: Multivariate sweep to determine the effect of pressure and temperature on the strips

By doing a random multivariate sweep, the pressure and humidity levels are varied randomly by introducing pumped air into the chamber and evacuating using a vacuum pump. From the time response, it is observed that the resistance change is almost exactly a mirror copy of the relative humidity in the chamber. The temperature was kept constant; however, some fluctuations were registered when the vacuum pump is operated due to temperature difference between the gas chamber and the lab environment in the outside. To understand the relationship between the measured parameters and the sensor's responses, a scatterplot matrix of the variables is generated as shown in Figure 63, using IBM SPSS.

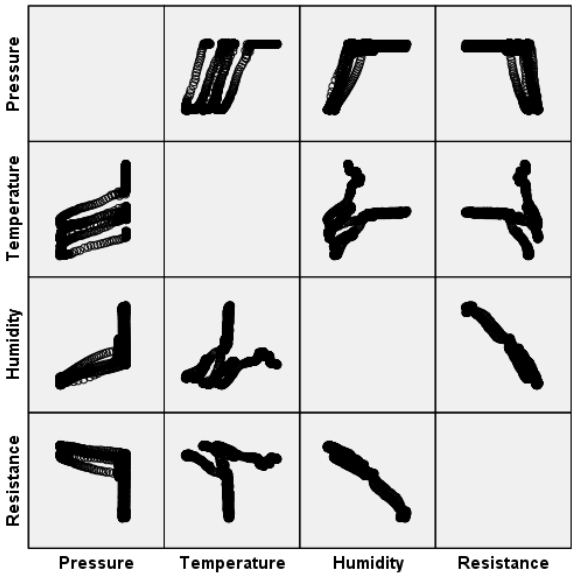

Figure 63: Scatterplot matrix of data sweeps similar to those of Figure 62

From the scatterplot matrix, it is evident that the resistance has high correlation with the relative humidity of the chamber. It is also useful to note that the correlation between humidity and pressure is reduced by introducing water vapour at random pressure. Nonetheless, some semblance of correlation is still observed because generally humidity will increase as pressure is increased. Correlation between pressure and temperature is still present, as Gay-Lussac's law holds true. However, the pressure-temperature response is split into multiple groups, possibly due to differences in the level of humidity. Figure 64 shows the correlation matrix for the scatterplot above (Figure 63).

Correlations

		Pressure	Temperature	Humidity	Resistance
Pressure	Pearson Correlation	1	.698**	.727**	-.553**
	Sig. (2-tailed)		.000	.000	.000
	N	2500	2500	2500	2500
Temperature	Pearson Correlation	.698**	1	.323**	-.123**
	Sig. (2-tailed)	.000		.000	.000
	N	2500	2500	2500	2500
Humidity	Pearson Correlation	.727**	.323**	1	-.958**
	Sig. (2-tailed)	.000	.000		.000
	N	2500	2500	2500	2500
Resistance	Pearson Correlation	-.553**	-.123**	**-.958****	1
	Sig. (2-tailed)	.000	.000	.000	
	N	2500	2500	2500	2500

**. Correlation is significant at the 0.01 level (2-tailed).

Figure 64: Correlation matrix of the pressure, temperature and humidity sweep

The correlation matrix shows the Pearson's correlation between each pair of variables. Note that the coefficient of correlation between resistance and humidity is extremely high, at -0.958, when compared to the other components. Do note, however, that the experiment was carried out under a near-constant temperature of about 33ºC, and the low correlation between temperature and resistance in this case does not imply that the material is not sensitive to temperature, but rather, it is an indication that the contribution of temperature is low in this case. A separate temperature sweep experiment was carried out and presented in the next section.

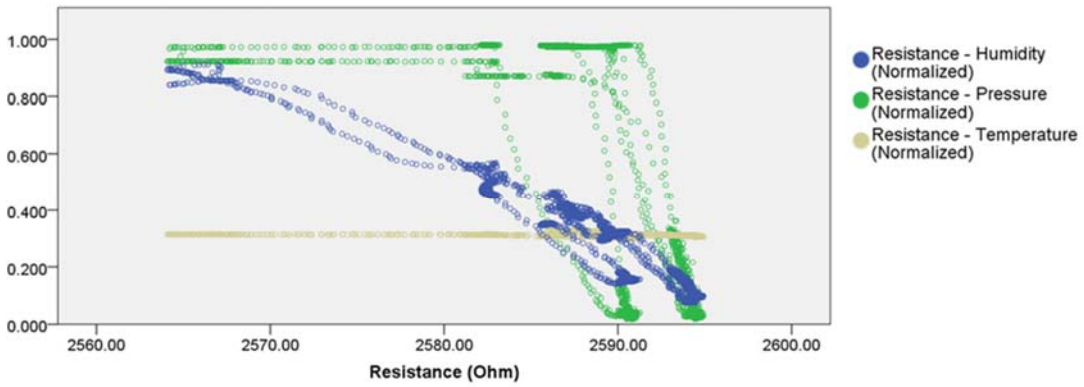

Figure 65: Group scatterplot of the sensor's response to temperature, humidity and pressure

From the group scatterplot (Figure 65), it is evident that the apparent variation of the sensor's resistance towards pressure is a direct result of the reduction of water vapour during the pumping cycle. At the higher humidity range (i.e. normalized humidity > 0.6), there appears to be no correlation between the pressure of the test environment and that of the sensor's resistance. At the lower humidity range, the correlation happens due to the use of a vacuum pump to remove the water pressure. As the pressure of the system bears little to no effect on the resistance of the sensor, the validity of the lower humidity range in the humidity test experiment was asserted. A further verification was carried out to understand the effects of pressure on resistance in the absence of other interfering factors.

6.3.2 Effects of pressure variations on NCG sensors in the absence of humidity variations

To study the effect of varying pressure on the NCG strip, the chamber was first pumped down to 20 kPa, and maintained at the said pressure for 2 hours. Then, the air pressure of the chamber was increased in steps until atmospheric pressure was reached. The humidity level and the pressure level were constantly monitored.

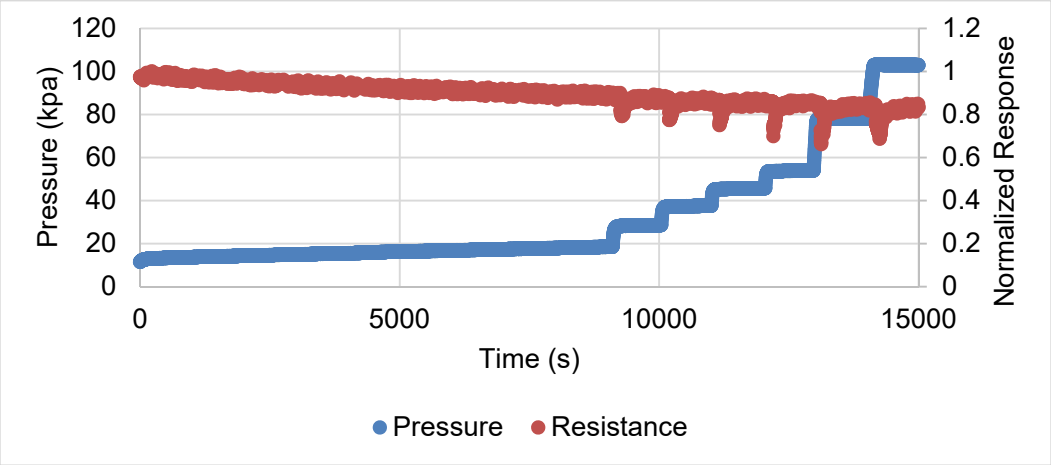

Figure 66: Time domain response of resistance and pressure

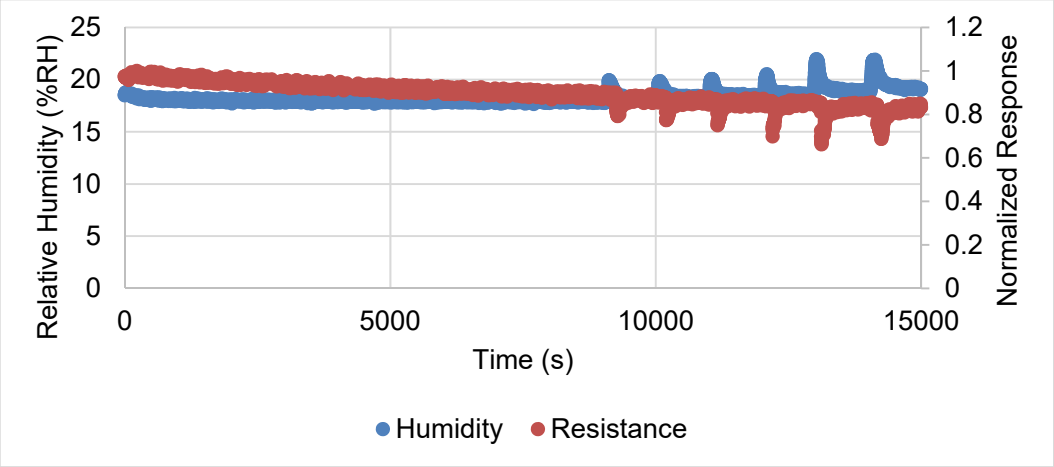

Figure 67: Time domain response of resistance and humidity

The pressure was increased in steps of ~10 kPa for 4 steps, and ~30 kPa for 2 steps by introducing N_2 into the test chamber. The sensor shows no discernible response to the change in pressure (Refer to Figure 66 and Figure 67). Also, during the first 2.5 hours, when the chamber was maintained at 20 kPa, the signal from the sensor remains stable. The slight decrease in resistance can be attributed to the presence of water which may desorb from the chamber wall due to the low pressure. A slight rise of the humidity level is measured by the reference sensor. During the pumping cycle, the sharp increase in humidity reading is attributed to the flow of air incident on the reference sensor. Our sensor response almost mirrors exactly the response of the humidity sensor. The slight observable correlation between the increase in pressure and the decrease in resistance can be attributed to the humidity fluctuations sensed by our sensor. From this experiment, the environmental pressure has no significant effect on the change in resistance of the NCG sensor.

6.3.3 Effects of temperature variation on NCG sensors

To study the temperature dependence of the NCG strips, 2 strips of the same geometrical dimensions (150 µm × 2500 µm) were used. One was exposed to the atmosphere, while the other was covered with SU8. The chip was mounted on a custom PCB, and wire bonded with aluminium wires.

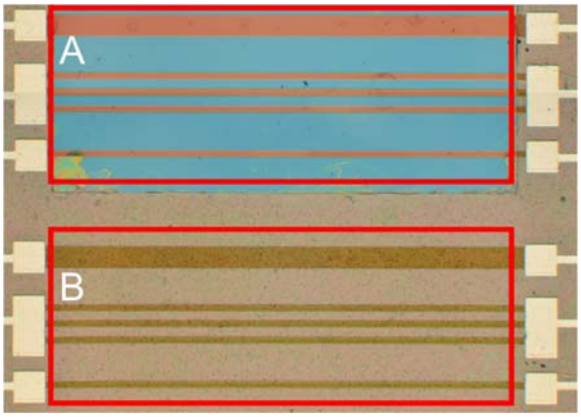

Figure 68: Identical strips on the sensor chip the chip. The region labelled A is exposed to air, while the region labelled B is covered with SU8.

Both strips (Figure 68) were exposed to atmosphere with average relative humidity of 55%. The relative humidity and room temperature of the environment was tracked with a commercially available Bosch BME280 environmental sensor and remained constant throughout the experiment. The resistance of the strips was measured with 2-terminal resistance measurement on a Keithley 2100 high precision multimeter.

The temperature sweep was controlled using a relay-based feedback control with a thermocouple-based feedback sensor. The heater was run at 60 W for 20 minutes, with a temperature setpoint of 55 ^{o}C. The resultant data was shown in Figure 69 and Figure 70.

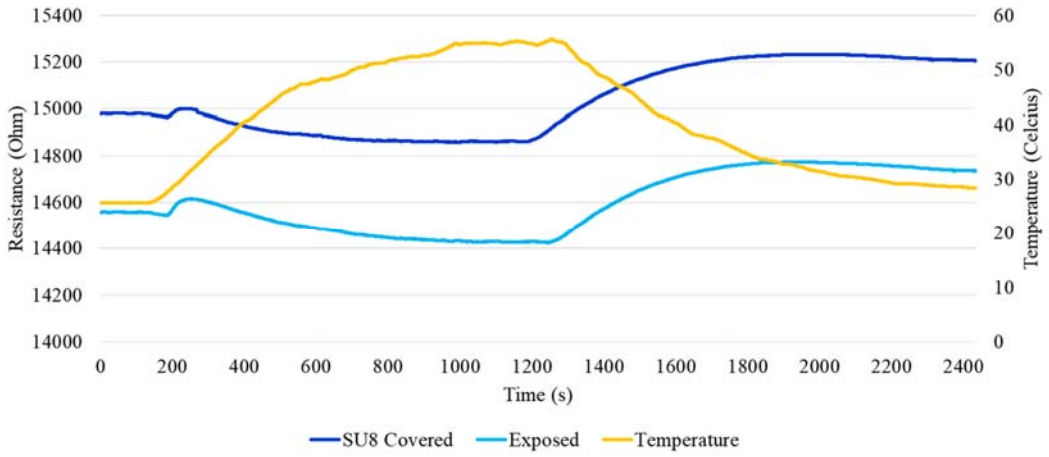

Figure 69: Variation of resistance measured at different temperature.

It is observed that the resistance rises slightly before decreasing at every heat up cycle. This was predicted to be a desorption process, as the strips were exposed to the atmosphere. Subsequent heat up and cool-down cycles show a weaker desorption peak, as the gas has less time to adsorb onto the surface. The surface covered with SU8 shows a significantly smaller desorption peak when compared to the exposed strip.

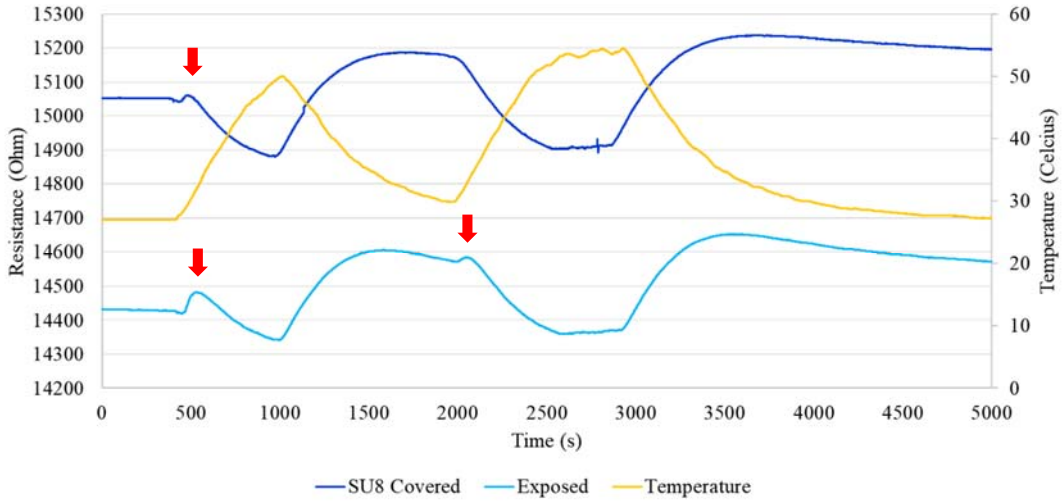

Figure 70: Variation of resistance measured at different temperature with two sweeps. Red arrows indicate desorption peaks.

The NCG strips experiences a resistance change of -0.005% $^{o}C^{-1}$ in response to the temperature sweep. This is important to note as the temperature of the environment may affect the reliability of NCG as a chemical sensor. Hence, a temperature reference is needed for temperature compensation whenever NCG is being used as a gas or humidity sensor.

6.4 Discussions

The results from section 6.1 and 6.3 shows that the resistance decreases upon the interaction of moisture with the NCG strip. If the sensing mechanism is charge transfer, one would expect the resistance of the film to increase. Since NCG is exhibiting P-type semiconducting behaviour, the electron transfer from the water molecule would decrease the available carriers available for conduction. The linear decrease of the resistance would suggest another sensing mechanism.

6.4.1 Conduction model of a two-phase material

In Section 5.4, a resistance model of the NCG was constructed based on the assumption that the sensing mechanism was due to charge transfer. However, for humidity sensing, a different model is proposed. The surface morphology of NCG is not uniform, as shown in Figure 25, thus, it is believed that capillary adsorption plays a major role in forming a conductive bridge at higher RH values. In this section, a piecewise type model is considered, where the change in resistance of the grain due to water adsorption (as in Eq. 38) is considered with an additional conduction path arising due to capillary adsorption of water.

Consider the equation 39:

$$R_{total} = R_{contact} + R_{exposed} + R_o \text{------ Eq. 39}$$

The total resistance consists of $R_{contact}$, which represents the total contact resistance, including the resistance across the wire-bond pad interface and the probe to multimeter interface, R_o the resistance of the unexposed areas of the film, and $R_{exposed}$, the resistance of the film areas exposed to the relative humidity. For any arbitrary path taken by the charge carrier on the NCG, there will be alternating regions of high resistivity (amorphous carbon areas) and high conductivity (crystalline areas).

Figure 71 shows an illustration of the cross-section of water adsorption in the film. The water droplets form conductive bridges which conduct better than the amorphous regions. It is assumed that the crystalline part of the film does not change its resistance. As the relative humidity increases, the number of bridges formed due to capillary condensation increases proportionally. Hence, causing a change in the film's resistance.

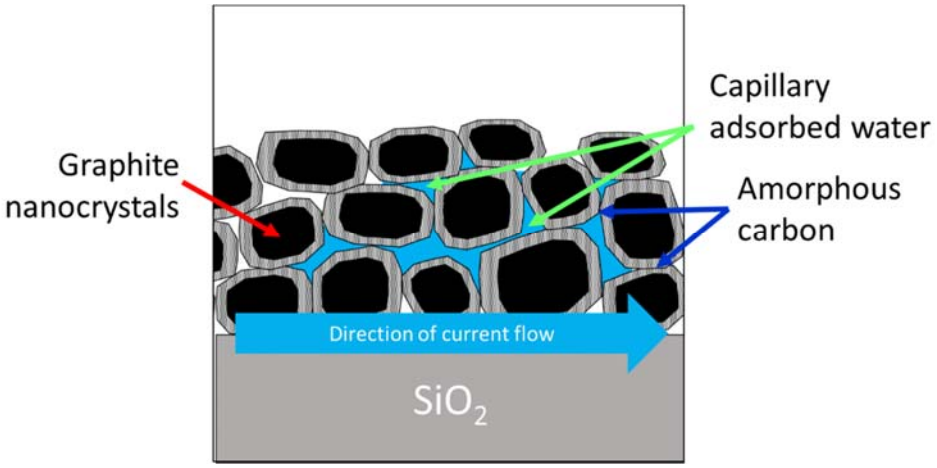

Figure 71: Illustration of average current moving across the NCG film. Gray areas denote grain boundaries with amorphous carbon, black area denotes graphitic crystals and blue area denotes water condensation due to capillary adsorption. Water is thought to adsorb favourably along the pores of the film due to capillary adsorption.

In a two-phase material, one can consider the average current density, J_a as a function of the effective conductivity of the two-phase material, σ_e, and the average electric field across the material, E_a [159]. The effective conductivity of the material is modelled as a function of the distribution of the phases, which is denoted as C_{grain} and $C_{boundary}$, where $C_{grain} = 1 - C_{boundary}$. From the SEM images of the film, it is determined that $C_{grain} >> C_{boundary}$.

The resistance of the film can be modelled as individual series resistance with a piecewise cross-sectional area connected in parallel to the other resistances. By taking a simple piece-wise model of the film, each piece can be thought of as a cuboid with a unit cross-sectional area, A. Figure 72 illustrates the piece-wise model for the resistance of NCG. The ratio of the effective length of the boundary resistance is proportional to the ratio of the C_{grain} and $C_{boundary}$. In cases where the current paths are disrupted by voids, it is assumed that the current flows around the void.

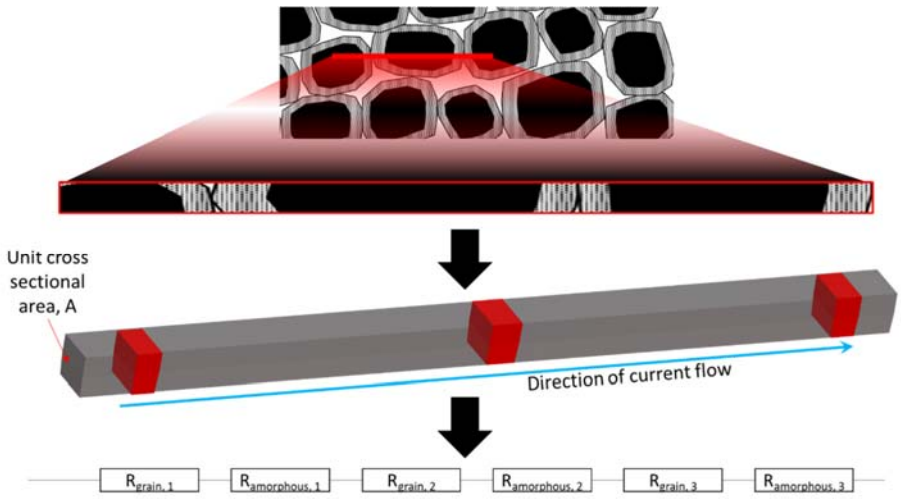

Figure 72: Simplified piece-wise model of the resistance in the film. Red area denotes resistance contributed by the amorphous regions.

The resistance at each of these sections could be modelled based on their geometry, using the resistance formula:

$$R_e = \frac{\rho_x L_e}{A} \text{ ------ Eq. 40}$$

where R_e is the effective resistance of the element, ρ_x is the resistivity of the said element, L_e is the effective length of the element and A is the cross-sectional area of the piecewise element being analysed. The total resistance along the length of the piecewise model is the sum of all the resistive elements:

$$R_{exposed,n} = \sum R_{grain,n,i} + \sum R_{amorphous,n,j} \text{ ------ Eq. 41}$$

where $R_{exposed,n}$ refers to the resistance of the nth strip, $R_{grain,n,i}$ is the resistance of the i^{th} grain within the strip and $R_{boundary,n,j}$ is the resistance of the j^{th} boundary within the strip. The resultant equivalent circuit is shown in Figure 73.

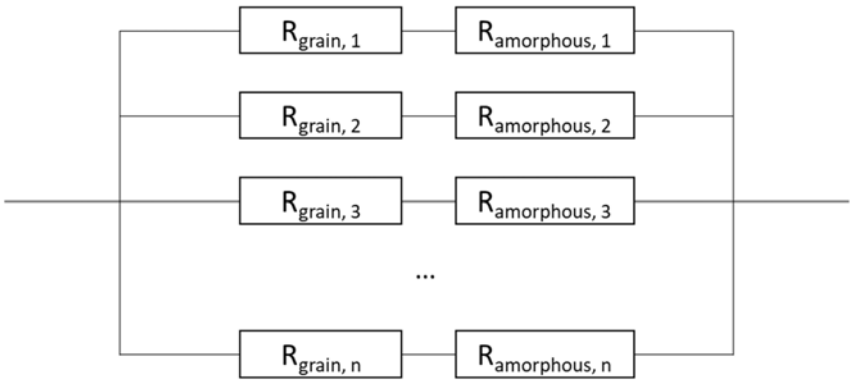

Figure 73: Resistance model of the NCG film

The alternating grain and boundary resistances are consolidated as R_{grain} and $R_{amorphous}$ accordingly, where R_{grain} is the sum of the series resistance contributed by the graphitic grains and $R_{amorphous}$ is the sum of the series resistance contributed by the grain boundaries in each strip along the current path.

6.4.2 Adsorption of water on NCG grains

The favourable adsorption of water onto the NCG surface is most likely due to the capillary adsorption effect. Due to the porosity of the film (Evident from Section 4.5), water will adsorb favourably at the grain boundaries. The adsorption of water molecules on the boundaries can be described with the Kelvin equation as shown:

$$\ln\left(\frac{p_v}{p_{sat}}\right) = \frac{2\gamma V_m}{rRT} \text{------ Eq. 42}$$

where p_v is the equilibrium vapour pressure, p_{sat} is the saturation vapour pressure for water condensation, r is the mean radius of the water meniscus, γ is the surface tension of the water-air interface, V_m is the molar volume of the liquid, R is the ideal gas constant and T is the temperature. As the value of equilibrium vapour pressure, p_v is increased relative to the saturation vapour pressure p_{sat}, capillary condensation will occur within a pore or crack, forming a meniscus until the liquid/vapour equilibrium is reached (As illustrated in Figure 74). Also, very small pores readily favours the adsorption of water.

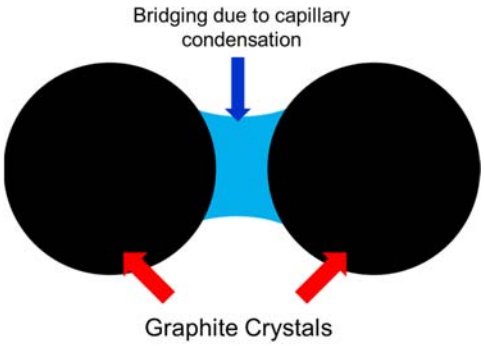

Figure 74: Illustration of water bridging due to capillary condensation

Assuming the system remains at a constant temperature, this will result in the increase in the adsorbed volume of water until a liquid-vapour equilibrium is reached. Thus, at a constant relative humidity value, a finite number of bridges will be formed across the film, creating a conduction path with a much lower resistance compared to the amorphous carbon (As illustrated in Figure 75).

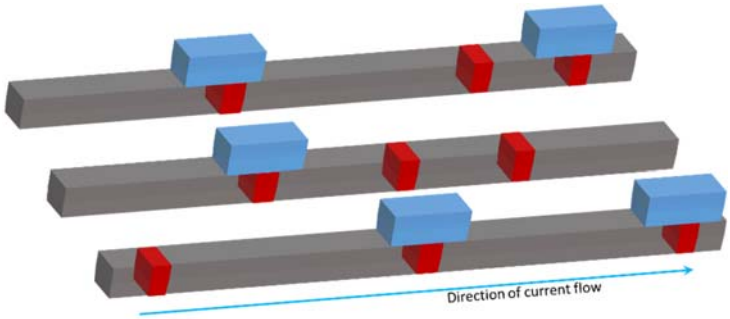

Figure 75: Resistance model of the exposed regions with bridge formed by capillary adsorption. Blue parts represent water droplets, grey regions represent conductive crystals and red regions represents amorphous carbon.

The conduction mechanism of the adsorbed water is explained previously in section 2.1.2. When bridging occurs across two adjacent grains due to capillary adsorption, the Grotthuss mechanism will create an alternative pathway for the current to flow. Hence, the sum of series resistance contributed by the boundary will be reduced due to the additional current pathways created by water adsorption. The resultant model is as shown in Figure 76.

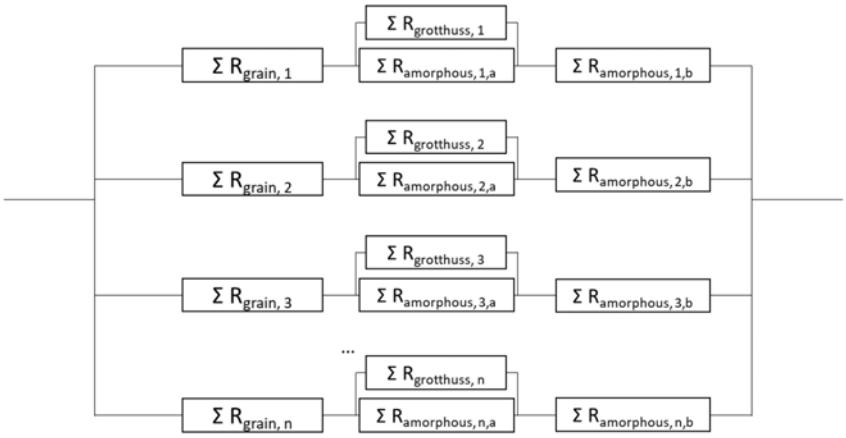

Figure 76: Resistance model of the NCG film with adsorbed water, $R_{grothuss}$ is the resistance across the capillary water bridge, $R_{amorphous,n,a}$ denotes resistance of grain boundary area with water, while $R_{amorphous,n,b}$ denotes resistance of the unexposed region.

In a narrower strip, there is fewer parallel paths available for conduction, hence, the *magnitude* of change per %RH is higher compared to the wider strips. In longer strips, one would also expect a larger *magnitude* of change, as the number of the exposed $R_{amorphous}$ will be much higher. Hence, a longer, narrower and thinner strip is much more favourable for humidity sensing.

The *sensitivity*, or the percentage resistance ΔR/R, will not change significantly as the wire dimensions change because the wire resistance scales linearly as R~ L_e/A. The simple model explains the major results; the decrease in NCG resistance with increasing humidity. If required, the response could be further modelled by computer simulation. One possible starting point would be to use the simple model above with,

$$\frac{1}{R_{exposed}} = \sum_{k=0}^{p} \frac{1}{\sum_{i=0}^{n} R_{grain,k,i} + \sum_{j=0}^{m} \begin{cases} R_{amorphous,k,j}(C(t)) & If\ no\ condensation \\ \frac{R_{amorphous,k,j,(C(t))} R_{grotthuss,k,j(C(t))}}{R_{amorphous,k,j,(C(t))} + R_{grotthuss,k,j(C(t))}} & otherwise \end{cases}} \quad \text{------ Eq. 43}$$

where *p, n* and *m* represent the number of piecewise elements in the direction of the cross-sectional area, the number of grains along the piecewise element, and the number of boundaries along the piecewise element of the film respectively. Here it is assumed that the probability of bridge formation increases linearly with the concentration of the water vapour C(t).

6.5 NCG humidity sensor application

In view of the robustness of NCG and its sensitivity towards humidity, the potential of using this material as a wearable breath monitoring system was tested. This system can be thought of as a "smart mask" which incorporates the sensor on the inner surface of the mask. Hence, additional considerations, such as the potential of exposure to sweat and saliva, must be considered. Based on the previous results, this sensor was implemented on a thin meandering design, scaled down to 10 µm by 940 µm.

6.5.1 Sensor design

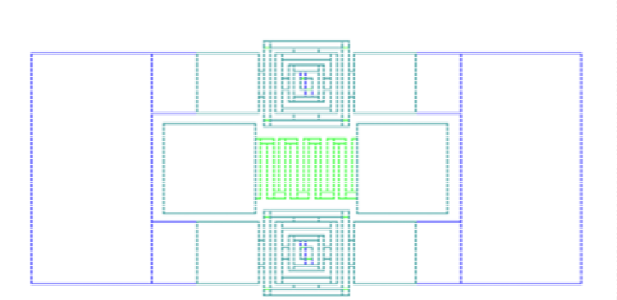

Figure 77: Layout of the human breath sensor, green colour denotes NCG (10µm by 940µm), while cyan denotes area where NCG and metal overlaps, blue region indicates metal pads.

The sensor was fabricated on the same batch process used to make the sensors used in section 6.3. However, the resultant sensor was not wire bonded. Instead, it is probed with tungsten needles mounted on 2 micromanipulators. Two Al/Ti heating pads were fabricated near the sensor to help in removing condensation should it occur (See Figure 77).

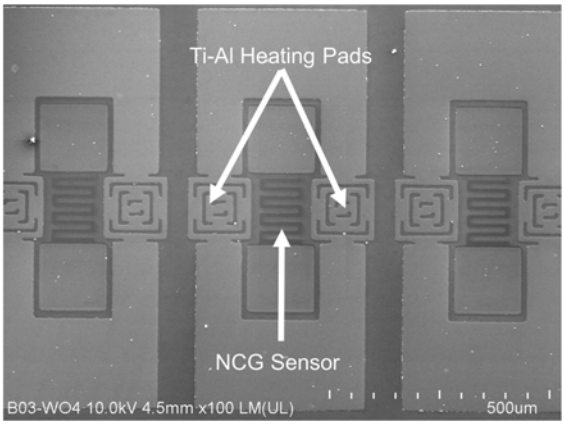

Figure 78: SEM image of the fabricated sensor with integrated heating pads

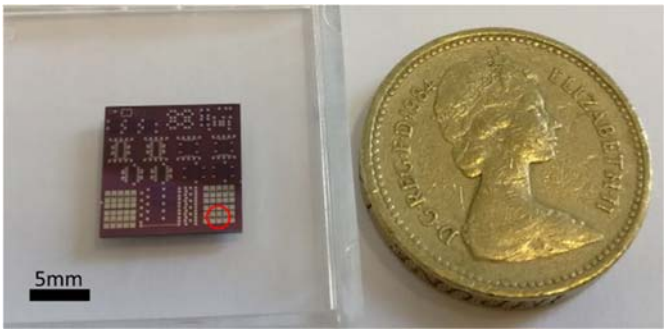

Figure 79: Size of the sensor in relation to a British Pound

The overall sensor was measured in an exposed, 1 cm by 1 cm silicon die (See Figure 79). The overall footprint of the sensor (including the heating pads) is 400 µm by 600 µm. Figure 79 shows the size of the sensor in relation to a British pound coin. The red circle denotes the area where the SEM image in Figure 78 was taken.

6.5.2 Human breath detection

For this experiment, the sensor shown in Figure 77 deposited on B03W05 was used as a reference.

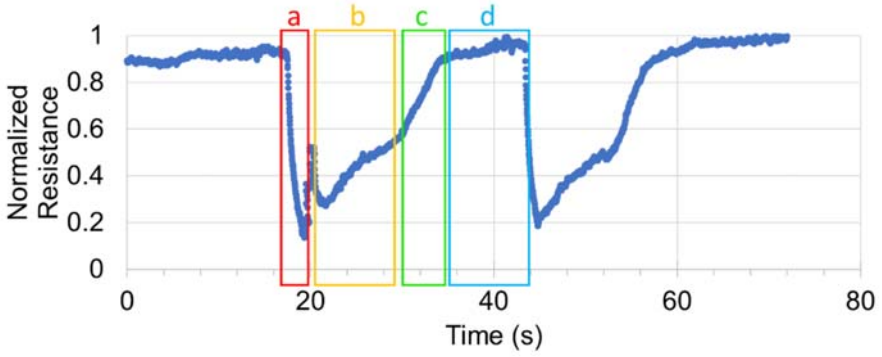

Figure 80: Normalized response of the sensor to a normal adult breath cycle

In Figure 80, the labelled sections corresponds to (a) Exhalation (b) Hold (c) Inhalation (d) Hold of the human breath. The resistance is normalized to baseline at room relative humidity (RH) level, 40%RH, to the maximum RH level, 100%RH. The baseline resistance is 56.32 kOhm. The sensor shows enough response to track and measure human breath in normal breathing conditions and has the potential to be developed into a further environmental sensing prototype.

6.5.3 Response to ionic solutions

To gauge the recoverability of the sensor towards possible environmental contaminants under the proposed application, concentrated KCl solution of 1.0 Mol was dripped onto the sensor to mimic sweat.

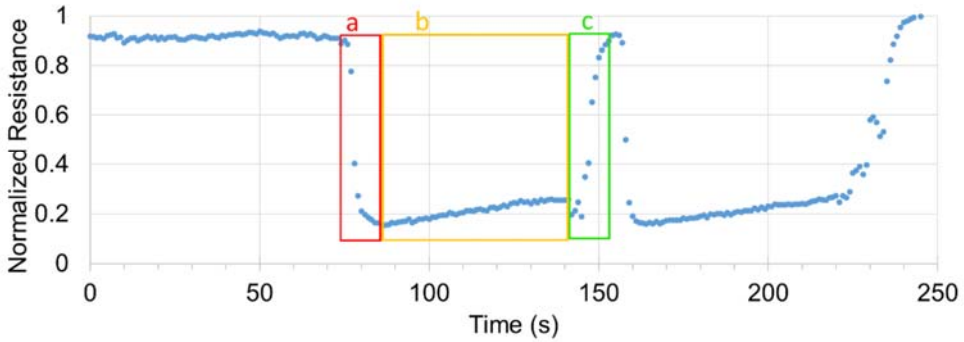

Figure 81: Resistance drop due to KCl solution The droplet was dripped onto the sensor at (a) and the droplet was left on the chip for the period labelled (b), and at (c), the process was repeated. At (c), the droplet was removed by gently touching the droplet with a piece of clean cleanroom wipe. Due to capillary action, the droplet is absorbed by the cleanroom wipe.

Figure 81 shows the response of the sensor towards a 10 µl droplet of KCl solution. There is a slight rise in resistance during (b), presumably due to the evaporation of the water in the KCL solution. Note that NCG contains grain boundaries with high resistance. Hence exposure to ionic solution will create a shunt which lowers the resistance almost instantly. However, as the droplet evaporates, the area covered by the droplet is gradually reduced. Hence, although the concentration of the ions in the droplet increases with time, the resistance is observed to increase as well.

After wiping, the sensor exhibits a slightly higher resistance than the baseline. This could be due to leftover dried ionic salt which could modify the properties of the film. However, the dried salt can easily be removed by washing with water.

Chapter 7: Conclusions and Outlook

In this thesis, the potential of using NCG as an environmental sensor for NO_2 and humidity is investigated. The sensor shows preferential response towards the humidity level of the environment and the sensing effect is thought to be due to the interaction between adsorbed water molecules and the grain boundaries of the sensor.

The sensor was fabricated using PECVD method which was developed in-house at the Southampton Nanofabrication Center. The NCG films were characterized to through various electrical and physical measurement to understand its electrical and structural properties. Here, the granular properties of NCG was confirmed, and the presence of amorphous carbon on the boundaries of NCG was shown using SAED and TEM images. The presence of sp^2 bonded carbon and high defect concentration (due to the presence of amorphous carbon) is shown on the Raman spectra of the NCG. Hall effect measurements on the NCG film reveals a hole-dominated transport mechanism on the NCG film.

Gas sensing measurements were done using NO_2, NH_3 and CO to determine the sensing characteristic of the NCG film. The resistance of the film decreases upon exposure to NO_2 and increases when exposed to reducing gasses (CO and NH_3). It is believed that the oxidizing nature of NO_2 depletes the electrons in the NCG film, thus causing an increase in holes. As the majority carrier in the NCG film are holes, the film experiences a decrease in resistance due to the increase in conductivity of the film. Upon exposure to reducing gasses, however, the film experiences an increase in resistance, due to the opposite effect. The measured response of the sensor towards 10 ppm of redox gas is 0.66% for NO_2, 0.14% for CO and 0.1% for NH_3. Future work could be done to further characterize the sensing effect of the NCG film towards higher concentration of redox gases.

At the same time, the film shows response to ambient moisture levels in static atmosphere. A modified sensing rig was constructed to investigate the response of the sensor towards varying level of relative humidity. In the static measurement, the chamber is isolated once the desired humidity level is reached, so no airflow is present in the chamber. The films experienced up to 3% change in resistance when exposed to 85%RH (with a recorded maximum change in resistance of 23.8kOhm for baseline-85%RH) measurements. The sensing result is not superior to graphene oxide and CVD graphene, but is comparable to pure graphene, multilayer graphene and carbon nanotubes. The relationship between the film's geometrical dimensions and shapes were investigated to determine the best sensor

configuration. The meandering structure was found to give the best sensing performance for the humidity sensor. The main sensing mechanism for water vapour was determined to be the capillary adsorption in the NCG pores combined with Grotthuss mechanism.

In conclusion, this work contributed to the following discoveries:

1. For the first time, the majority carrier of NCG was measured with Hall effect characterization and was determined to be holes instead of electrons.
2. The gas sensing characteristic of PECVD NCG towards redox gasses (NO_2, NH_3 and CO) was demonstrated. The results confirmed the initial discovery that the NCG exhibits p-type semiconducting behaviour. The p-type nature of the film could be contributed by the presence of amorphous carbon between the NCG grains, visible on the TEM images.
3. The sensing response of NCG towards humidity was found to be an order of magnitude higher than that of redox gasses. The resistance decreases upon exposure to higher humidity, as opposed to an increase, thus suggesting a different sensing mechanism.
4. After further investigation, it is believed that the humidity sensitivity of NCG is a result of capillary condensation near the grain boundaries, and the effect of Grotthuss mechanism creating a shunt across grain boundaries on the film. The hypothesis was supported by TEM and SEM data showing the granular structure of the NCG film.

7.1 Future work

In this thesis, two possible applications for environmental sensing with NCG were investigated, namely gas sensing for redox species, and humidity sensing. However, due to the robustness of this material, there's a possibility to extend the research into several other directions. Here, some other applications which may be explored with the current results are presented.

7.1.1 Electrochemical sensing

Graphite based sensors for electrochemical sensing have been reported extensively in the literature. [160]–[164]. However, most of the reported materials involve either using graphite powder or bulk graphite. The use of PECVD NCG could potentially allow miniaturization and deposition of graphitic electrodes which are stable and controllable, with known grain size for electrochemical sensing purposes.

7.1.2 Electronic nose application

From the results shown in Chapter 5 and 6, we've shown that NCG responds to redox gasses and relative humidity. By combining NCG with other sensing materials, one can create an array of sensors which responds orthogonally to different gasses or chemicals.

Using such an array, it will be possible to train an Artificial Neural Network to recognize different species of gasses based on the pattern it generates on the sensor array. However, further studies would need to be done to investigate other sensing material and possible surface functionalization methods which was not included in this thesis.

7.1.3 Further prototype development

In section 6.4.2, a prototype human breath detection system was presented. The system shows good measurement characteristics, and good recovery in room temperature. Therefore, it could be a good candidate for the development of a smart mask system for breath tracking application with commercialization potential. The material would have to undergo further testing to gauge its robustness when exposed to environmental contaminants such as sweat and saliva.

Appendices

Appendix A Device Map

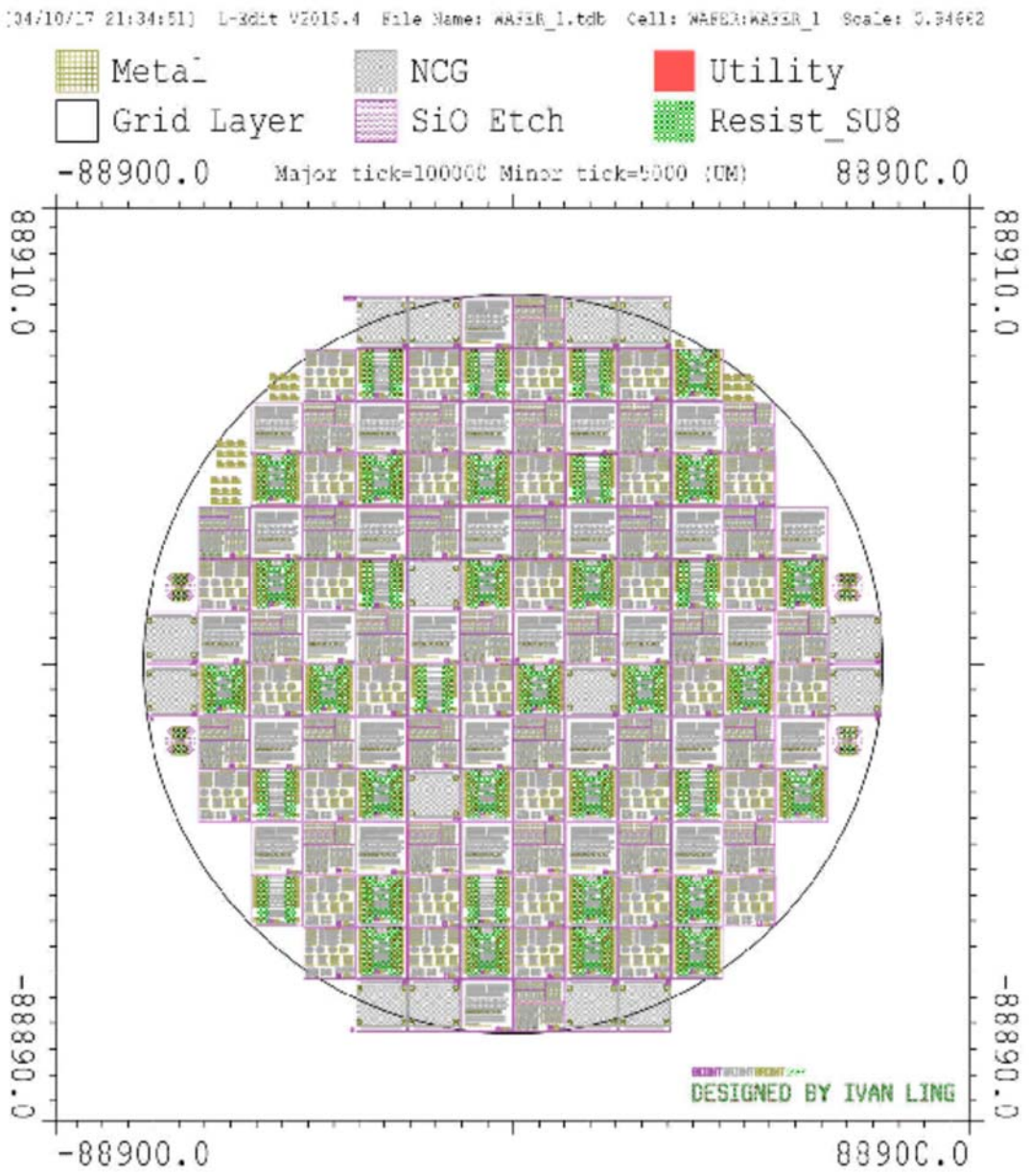

Final Mask layout used for NC-graphite strip fabrication

Appendix B Crystallographic Parameters of Graphite

Here, the crystallographic parameters of graphite are shown.

B.1 Name and Formula

Reference Code: 01-075-1621

Mineral name: Graphite 2H

ICSD Name: Carbon

Empirical formula: C

Chemical formula: C

B.2 Crystallographic Parameters

Crystal system: Hexagonal

a (Å) : 2.47 Alpha(°) = 90

b (Å) : 2.47 Beta(°) = 90

c (Å) : 6.79 Gamma(°) = 120

B.3 XRD Peak List

No.	h	k	l	d [A]	2Theta[deg]	I [%]
1	0	0	2	3.39500	26.228	100.0
2	1	0	0	2.13908	42.214	2.9
3	1	0	1	2.04023	44.365	13.8
4	1	0	2	1.80980	50.381	2.6
5	0	0	4	1.69750	53.974	5.0
6	1	0	3	1.55463	59.404	3.6
7	1	0	4	1.32969	70.804	0.6
8	1	1	0	1.23500	77.177	3.1
9	1	1	2	1.16060	83.167	4.8
10	1	0	5	1.14648	84.425	0.9
11	0	0	6	1.13167	85.793	0.7

Here, the XRD peaks of a graphite sample is presented. The peaks correspond to the interlayer spacing of the graphite sample and can be used to determine the graphitic nature of NCG.

B.4 Stick Pattern

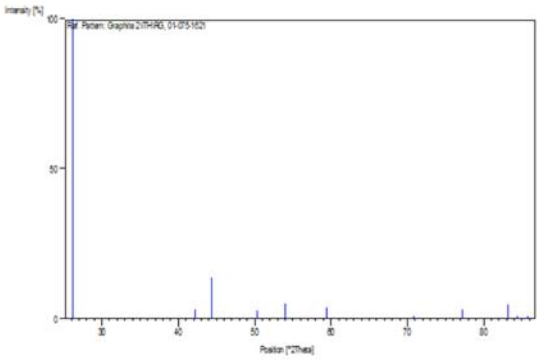

Here the stick pattern of the graphite XRD peaks in B3 is plotted against position.

Adapted from [150]

Appendix C SEM Images of Devices

Here some other fabricated devices with potential to be used in other applications in the future is presented.

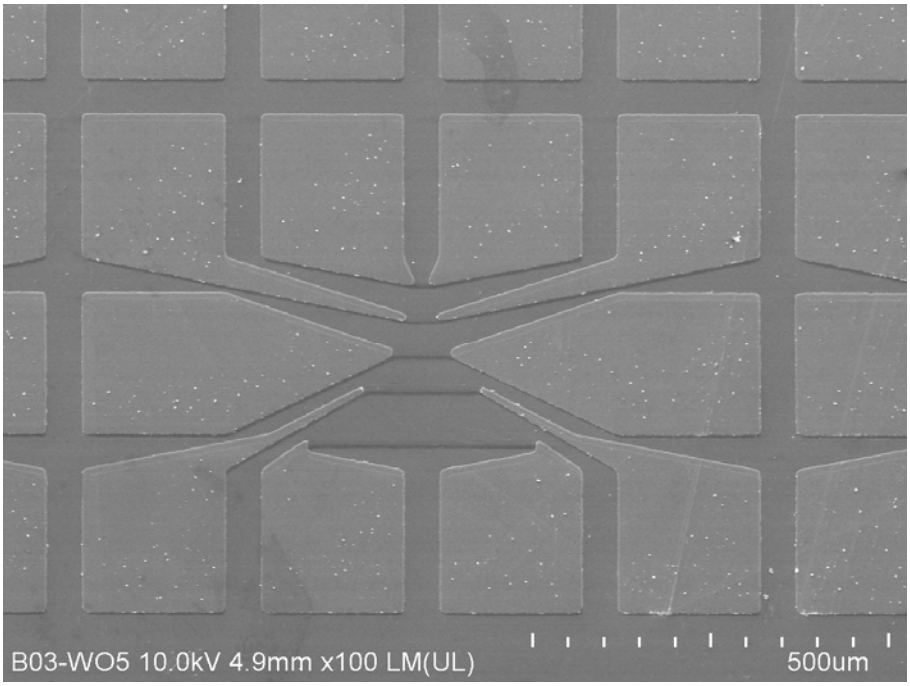

Thinner NCG strips with much smaller cross sectional area to maximize the effective interaction area for gas sensing.

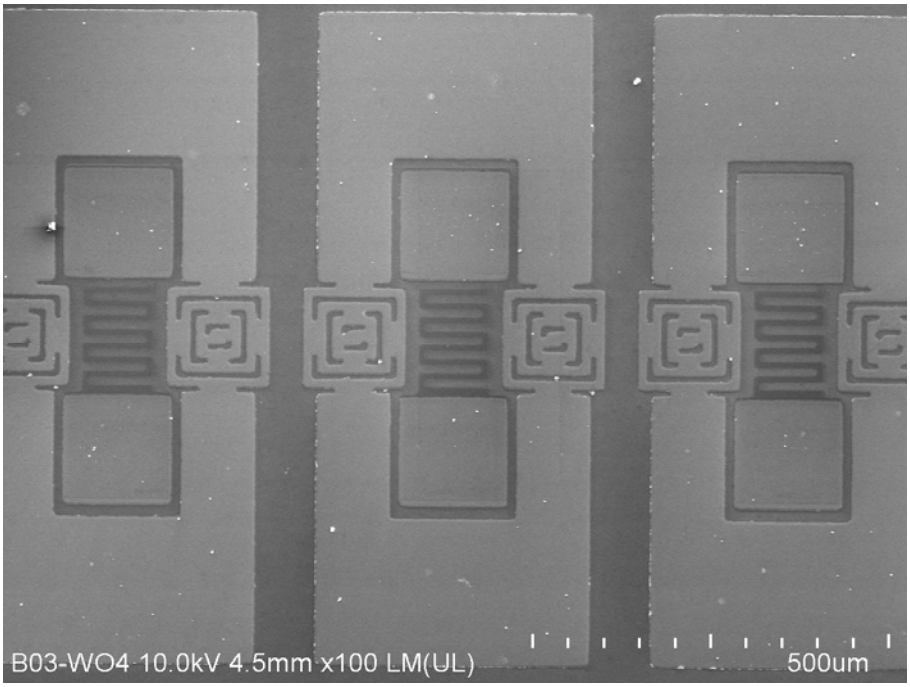

Meandered NCG sensor with integrated heater

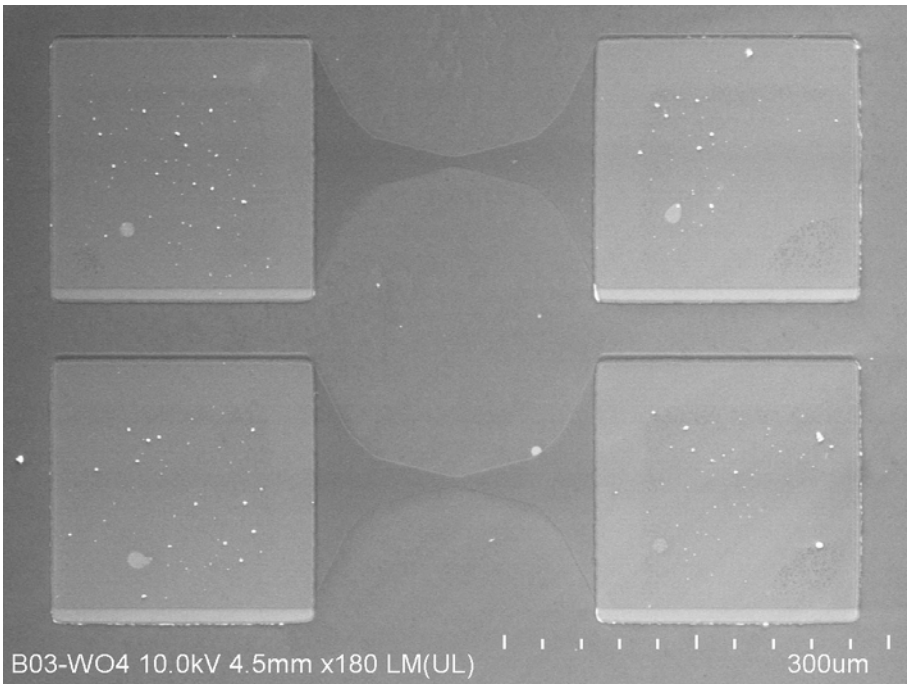

Tapered NCG strip with a thin neck for possible self-heating sensor.

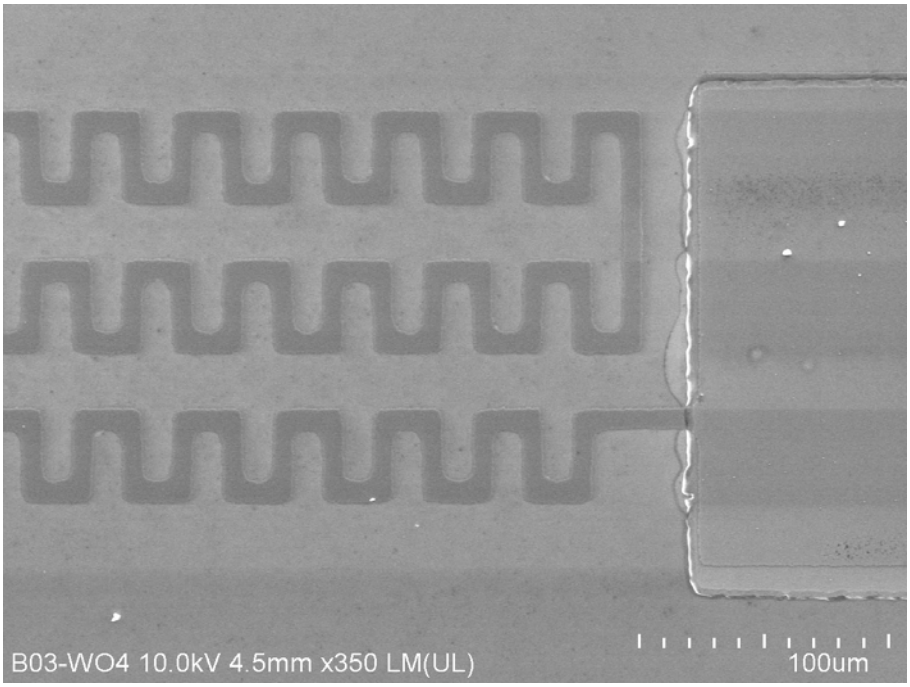

10 um x 1 mm meandering sensor

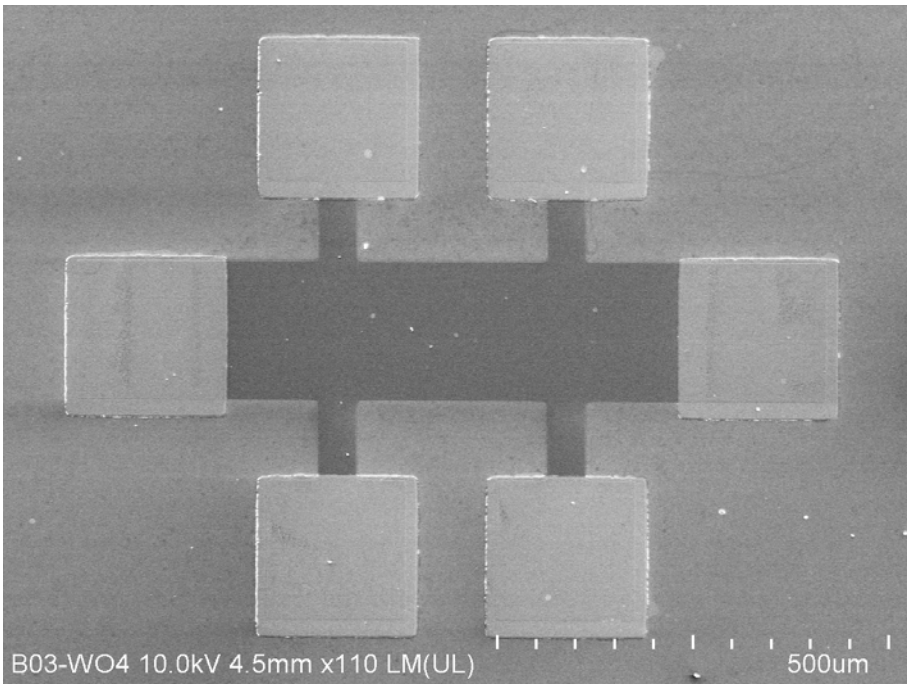

NCG Hall-bar device

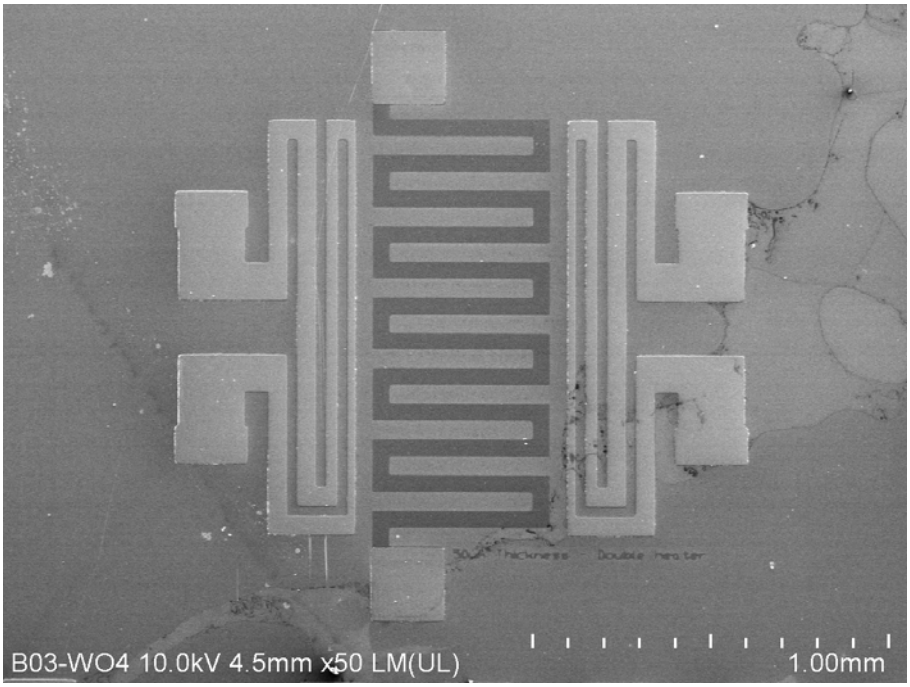

Meandered NCG sensor with heating pads.

List of References

[1] G. T. Miller and D. Hackett, “Photochemical and Industrial Smog,” in *Living in the Environment*, 2011, pp. 465–471.

[2] E. Commission, “Air Quality Standards,” *European Commission - Environment*, 2017. [Online]. Available: http://ec.europa.eu/environment/air/quality/standards.htm.

[3] WHO, “Health Aspects of Air Pollution with Particulate Matter , Ozone and Nitrogen Dioxide,” *Rep. a WHO Work. Gr. Bonn, Ger. 13–15 January 2003*, no. January, p. 98, 2003.

[4] “Global air pollution map produced by Envisat’s SCIAMACHY,” *ENVISAT*, 2004. [Online]. Available: http://www.esa.int/Our_Activities/Observing_the_Earth/Envisat/Global_air_pollution_map_produced_by_Envisat_s_SCIAMACHY.

[5] J.W. Han, B. Kim, J. Li, and M. Meyyappan, “A carbon nanotube based ammonia sensor on cellulose paper,” *RSC Adv.*, vol. 4, no. 2, p. 549, 2014.

[6] J. W. Han, J. L. Beomseok Kim, and M. Meyyappan, “Carbon Nanotube Based Humidity Sensor on Cellulose Paper,” *J. od Phys. Chem. C*, no. OCTOBER 2012, pp. 22094–22097, 2012.

[7] J. T. W. Yeow and J. P. M. She, “Carbon nanotube-enhanced capillary condensation for a capacitive humidity sensor,” *Nanotechnology*, vol. 17, no. 21, pp. 5441–5448, 2006.

[8] V. I. Popov, D. V Nikolaev, V. B. Timofeev, S. A. Smagulova, and I. V Antonova, “Graphene-based humidity sensors : the origin of alternating resistance change,” 2017.

[9] D. Zhang, J. Tong, and B. Xia, “Humidity-sensing properties of chemically reduced graphene oxide/polymer nanocomposite film sensor based on layer-by-layer nano self-assembly,” *Sensors Actuators, B Chem.*, vol. 197, pp. 66–72, 2014.

[10] M. V. S. Chandrashekhar, J. Lu, M. G. Spencer, M. Qazi, and G. Koley, “Large area nanocrystalline graphite films on SiC for gas sensing applications,” *Proc. IEEE Sensors*, pp. 558–561, 2007.

[11] D. Noll, U. Schwalke, and T. U. Darmstadt, “Feasibility study of in-situ grown nanocrystalline graphene for humidity sensing,” pp. 2–5, 2017.

[12] F. Ricciardella *et al.*, “Effects of graphene defects on gas sensing properties towards NO_2 detection,” *Nanoscale*, vol. 9, no. 18, pp. 6085–6093, 2017.

[13] M. E. Schmidt, C. Xu, M. Cooke, H. Mizuta, and H. M. H. Chong, “Metal-free plasma-enhanced chemical vapor deposition of large area nanocrystalline graphene,” *Mater. Res. Express*, vol. 1, no. 2, p. 025031, 2014.

[14] S. J. Fishlock *et al.*, “Micromachined nanocrystalline graphite membranes for gas separation,” *Carbon N. Y.*, vol. 138, no. June, pp. 125–133, 2018.

[15] S. Carquigny, J.-B. Sanchez, F. Berger, B. Lakard, and F. Lallemand, “Ammonia gas sensor based on electrosynthesized polypyrrole films.,” *Talanta*, vol. 78, no. 1, pp. 199–206, 2009.

[16] Q. Ameer and S. B. Adeloju, “Polypyrrole-based electronic noses for environmental and industrial analysis,” *Sensors Actuators, B Chem.*, vol. 106, no. 2, pp. 541–552, 2005.

[17] H. K. Jun *et al.*, “Electrical properties of polypyrrole gas sensors fabricated under various pretreatment conditions,” *Sensors Actuators, B Chem.*, vol. 96, no. 3, pp. 576–581, 2003.

[18] J. B. Chang *et al.*, “Printable polythiophene gas sensor array for low-cost electronic noses,” *J. Appl. Phys.*, vol. 100, no. 1, 2006.

[19] F. Liao, M. F. Toney, and V. Subramanian, “Thickness changes in polythiophene gas sensors exposed to vapor,” *Sensors Actuators, B Chem.*, vol. 148, no. 1, pp. 74–80, 2010.

[20] H. Malkeshi and H. Milani Moghaddam, “Ammonia gas-sensing based on polythiophene film prepared through electrophoretic deposition method,” *J. Polym. Res.*, vol. 23, no. 6, 2016.

[21] P. Bhattacharyya, P. K. Basu, H. Saha, and S. Basu, “Fast response methane sensor using nanocrystalline zinc oxide thin films derived by sol-gel method,” *Sensors Actuators, B Chem.*, vol. 124, no. 1, pp. 62–67, 2007.

[22] J. S. Suehle, R. E. Cavicchi, M. Gaitan, and S. Semancik, “Tin oxide gas sensor

fabricated using CMOS micro-hotplates and\nin-situ processing," *IEEE Electron Device Lett.*, vol. 14, no. 3, pp. 118–120, 1993.

[23] N. Yamazoe, G. Sakai, and K. Shimanoe, "Oxide semiconductor gas sensors," *Catal. Surv. from Asia*, vol. 7, no. 1, pp. 63–75, 2003.

[24] A. Qureshi, W. P. Kang, J. L. Davidson, and Y. Gurbuz, "Review on carbon-derived, solid-state, micro and nano sensors for electrochemical sensing applications," *Diam. Relat. Mater.*, vol. 18, no. 12, pp. 1401–1420, 2009.

[25] H. Y. Jeong *et al.*, "Flexible room-temperature NO2 gas sensors based on carbon nanotubes/reduced graphene hybrid films," *Appl. Phys. Lett.*, vol. 96, no. 21, pp. 2012–2015, 2010.

[26] Figaro Engineering Inc, "Operating Principle of Catalytic Sensors." [Online]. Available: https://www.figaro.co.jp/en/technicalinfo/principle/catalytic-type.html.

[27] G. Korotcenkov, "Metal oxides for solid-state gas sensors: What determines our choice?," *Mater. Sci. Eng. B Solid-State Mater. Adv. Technol.*, vol. 139, no. 1, pp. 1–23, 2007.

[28] N. Yamazoe, "Toward innovations of gas sensor technology," *Sensors Actuators, B Chem.*, vol. 108, no. 1-2 SPEC. ISS., pp. 2–14, 2005.

[29] T. Seiyama, N. Yamazoe, and H. Arai, "Humidity sensors*," vol. 4, pp. 86–96, 1983.

[30] H. Farahani, R. Wagiran, and M. N. Hamidon, *Humidity sensors principle, mechanism, and fabrication technologies: A comprehensive review*, vol. 14, no. 5. 2014.

[31] W. De Lin, H. M. Chang, and R. J. Wu, "Applied novel sensing material graphene/polypyrrole for humidity sensor," *Sensors Actuators, B Chem.*, vol. 181, pp. 326–331, 2013.

[32] S. W. Lee *et al.*, "Sorption/desorption hysteresis of thin-film humidity sensors based on graphene oxide and its derivative," *Sensors Actuators, B Chem.*, vol. 237, pp. 575–580, 2016.

[33] O. Markovitch, H. Chen, S. Izvekov, F. Paesani, G. A. Voth, and N. Agmon, "Special pair dance and partner selection: Elementary steps in proton transport in liquid water," *J. Phys. Chem. B*, vol. 112, no. 31, pp. 9456–9466, 2008.

[34] T. Miyake and M. Rolandi, “Grotthuss mechanisms: From proton transport in proton wires to bioprotonic devices,” *J. Phys. Condens. Matter*, vol. 28, no. 2, pp. 0–18, 2015.

[35] N. Agmon, S. Y. Goldberg, and D. Huppert, “Salt effect on transient proton transfer to solvent and microscopic proton mobility,” *J. Mol. Liq.*, vol. 64, no. 1–2, pp. 161–195, 1995.

[36] E. Traversa, G. Gnappi, A. Montenero, and G. Gusmano, “Ceramic thin films by sol-gel processing as novel materials for integrated humidity sensors,” *Sensors Actuators B Chem.*, vol. 31, no. 1–2, pp. 59–70, 1996.

[37] H. Zhao *et al.*, “Organic-inorganic hybrid materials based on mesoporous silica derivatives for humidity sensing,” *Sensors Actuators, B Chem.*, vol. 248, pp. 803–811, 2017.

[38] G. Lu, N. Miura, and N. Yamazoe, “High-Temperature NO or NO2 Sensor Using Stabilized Zirconia and Tungsten Oxide Electrode,” *Ionics (Kiel).*, vol. 4, pp. 16–24, 1998.

[39] R. H. Bari and S. B. Patil, “Improved NO 2 sensing performance of nanostructured Zn doped SnO 2 thin films,” *Int. J. TechnoChem Res.*, vol. 01, no. 02, pp. 86–96, 2015.

[40] E. Comini, G. Faglia, G. Sberveglieri, Z. Pan, and Z. L. Wang, “Stable and highly sensitive gas sensors based on semiconducting oxide nanobelts,” *Appl. Phys. Lett.*, vol. 81, no. 10, pp. 1869–1871, 2002.

[41] P. Chou, H. Chen, I. Liu, C. Chen, and J. Liou, “Nitrogen Oxide (NO 2) Gas Sensing Performance of,” *IEEE Sens. J.*, vol. 15, no. 7, pp. 3759–3763, 2015.

[42] J. A. Dirksen, K. Duval, and T. A. Ring, “NiO thin-film formaldehyde gas sensor,” *Sensors Actuators, B Chem.*, vol. 80, no. 2, pp. 106–115, 2001.

[43] A. M. Ruiz, G. Sakai, A. Cornet, K. Shimanoe, J. R. Morante, and N. Yamazoe, “Cr-doped TiO2 gas sensor for exhaust NO2 monitoring,” *Sensors Actuators, B Chem.*, vol. 93, no. 1–3, pp. 509–518, 2003.

[44] C. Fisica, U. Milane, and V. Golgi, “Thick Film ZnO Resistive Gas Sensors,” vol. 136, no. 7, pp. 9–12, 1989.

[45] W. Benecke and A. Meckes, “A smart gas sensing microsystem,” *Ind. Electron. 1998. Proceedings. ISIE ’98. IEEE Int. Symp.*, vol. 1, pp. 263–266 vol.1, 1998.

[46] K. Song, Q. Wang, Q. Liu, H. Zhang, and Y. Cheng, “A wireless electronic nose system using a Fe2O3 gas sensing array and least squares support vector regression,” *Sensors*, vol. 11, no. 1, pp. 485–505, 2011.

[47] V. Jelicic, M. Magno, G. Paci, D. Brunelli, and L. Benini, “Design, characterization and management of a wireless sensor network for smart gas monitoring,” *2011 4th IEEE Int. Work. Adv. Sensors Interfaces*, vol. 4, pp. 115–120, 2011.

[48] F. Hossein-Babaei, M. Keshmiri, M. Kakavand, and T. Troczynski, “A resistive gas sensor based on undoped p-type anatase,” *Sensors Actuators, B Chem.*, vol. 110, no. 1, pp. 28–35, 2005.

[49] C. H. Kwon *et al.*, “Thick-film zinc-oxide gas sensor for the control of lean air-to-fuel ratio in domestic combustion systems,” *Sensors Actuators B. Chem.*, vol. 25, no. 1–3, pp. 610–613, 1995.

[50] B. Rao, “Zinc oxide semiconductor gas sensor for ethanol vapours,” *Mater. Chem. Phys.*, vol. 64, no. November 1999, pp. 62–65, 2000.

[51] H. Nanto, T. Minami, and S. Takata, “Zinc-oxide thin-film ammonia gas sensors with high sensitivity and excellent selectivity,” *J. Appl. Phys.*, vol. 60, no. 2, pp. 482–484, 1986.

[52] S.-J. S.-P. S.-J. S.-P. Chang *et al.*, “A ZnO nanowire-based humidity sensor,” *Superlattices Microstruct.*, vol. 47, no. 6, pp. 772–778, 2010.

[53] S. H. Wang, T. C. Chou, and C. C. Liu, “Nano-crystalline tungsten oxide NO2 sensor,” *Sensors Actuators, B Chem.*, vol. 94, no. 3, pp. 343–351, 2003.

[54] S. J. Kim, I. S. Hwang, J. K. Choi, and J. H. Lee, “Gas sensing characteristics of WO3 nanoplates prepared by acidification method,” *Thin Solid Films*, vol. 519, no. 6, pp. 2020–2024, 2011.

[55] M. Breedon *et al.*, “Synthesis of nanostructured tungsten oxide thin films: A simple, controllable, inexpensive, aqueous sol-gel method,” *Cryst. Growth Des.*, vol. 10, no. 1, pp. 430–439, 2010.

[56] Y. Qin, M. Hu, and J. Zhang, “Microstructure characterization and NO2-sensing

properties of tungsten oxide nanostructures," *Sensors Actuators, B Chem.*, vol. 150, no. 1, pp. 339–345, 2010.

[57] C. Zhang, M. Debliquy, A. Boudiba, H. Liao, and C. Coddet, "Sensing properties of atmospheric plasma-sprayed WO3 coating for sub-ppm NO2 detection," *Sensors Actuators, B Chem.*, vol. 144, no. 1, pp. 280–288, 2010.

[58] Y. Qin, X. Sun, X. Li, and M. Hu, "Room temperature NO2-sensing properties of Ti-added nonstoichiometric tungsten oxide nanowires," *Sensors Actuators B Chem.*, vol. 162, no. 1, pp. 244–250, 2012.

[59] A. Searl, "A review of the acute and long term impacts of exposure to nitrogen dioxide in the United Kingdom," *Inst. Occup. Med.*, no. December, 2004.

[60] S. Virji, J. Huang, R. B. Kaner, and B. H. Weiller, "Polyaniline nanofiber gas sensors: Examination of response mechanisms," *Nano Lett.*, vol. 4, no. 3, pp. 491–496, 2004.

[61] H. Bai and G. Shi, "Gas Sensors Based on Conducting Polymers," *Sensors*, vol. 7, no. 3, pp. 267–307, 2007.

[62] I. Fratoddi, I. Venditti, C. Cametti, and M. V. Russo, "Chemiresistive polyaniline-based gas sensors: A mini review," *Sensors Actuators, B Chem.*, vol. 220, pp. 534–548, 2015.

[63] D. Nicolas-Debarnot and F. Poncin-Epaillard, "Polyaniline as a new sensitive layer for gas sensors," *Anal. Chim. Acta*, vol. 475, no. 1–2, pp. 1–15, 2003.

[64] A. L. Kukla, Y. M. Shirshov, and S. A. Piletsky, "Ammonia sensors based on sensitive polyaniline films," *Sensors Actuators, B Chem.*, vol. 37, no. 3, pp. 135–140, 1996.

[65] S. Srinives, T. Sarkar, and A. Mulchandani, "Nanothin polyaniline film for highly sensitive chemiresistive gas sensing," *Electroanalysis*, vol. 25, no. 6, pp. 1439–1445, 2013.

[66] M. a Chougule *et al.*, "Polypyrrole Thin Film : Room Temperature Ammonia Gas Sensor NH C H OH," vol. 11, no. 9, pp. 2137–2141, 2011.

[67] P. G. Su, C. T. Lee, and C. Y. Chou, "Flexible NH3 sensors fabricated by in situ self-assembly of polypyrrole," *Talanta*, vol. 80, no. 2, pp. 763–769, 2009.

[68] F. Kong *et al.*, "The preparation and gas sensitivity study of polythiophene/SnO2

composites," *Mater. Sci. Eng. B Solid-State Mater. Adv. Technol.*, vol. 150, no. 1, pp. 6–11, 2008.

[69] F. Schedin *et al.*, "Detection of individual gas molecules adsorbed on graphene," *Nat. Mater.*, vol. 6, no. 9, pp. 652–655, 2007.

[70] H. Kim *et al.*, "Activation energy paths for graphene nucleation and growth on Cu," *ACS Nano*, vol. 6, no. 4, pp. 3614–3623, 2012.

[71] L. A. Jauregui, H. Cao, W. Wu, Q. Yu, and Y. P. Chen, "Electronic properties of grains and grain boundaries in graphene grown by chemical vapor deposition," *Solid State Commun.*, vol. 151, no. 16, pp. 1100–1104, 2011.

[72] N. Mishra, J. Boeckl, N. Motta, and F. Iacopi, "Graphene growth on silicon carbide: A review," *Phys. Status Solidi Appl. Mater. Sci.*, vol. 213, no. 9, pp. 2277–2289, 2016.

[73] L. A. Jauregui, H. Cao, W. Wu, Q. Yu, and Y. P. Chen, "Electronic properties of grains and grain boundaries in graphene grown by chemical vapor deposition," *Solid State Commun.*, vol. 151, no. 16, pp. 1100–1104, 2011.

[74] P. Vancsó *et al.*, "Electronic transport through ordered and disordered graphene grain boundaries," *Carbon N. Y.*, vol. 64, pp. 101–110, 2013.

[75] S. S. Varghese, S. Lonkar, K. K. Singh, S. Swaminathan, and A. Abdala, "Recent advances in graphene based gas sensors," *Sensors Actuators, B Chem.*, vol. 218, pp. 160–183, 2015.

[76] A. Salehi-Khojin *et al.*, "Polycrystalline graphene ribbons as chemiresistors," *Adv. Mater.*, vol. 24, no. 1, pp. 53–57, 2012.

[77] A. K. Geim and K. S. Novoselov, "the Rise of Graphene," pp. 1–14.

[78] J. Sun, M. Muruganathan, and H. Mizuta, "Room temperature detection of individual molecular physisorption using suspended bilayer graphene," no. April, pp. 1–8, 2016.

[79] Y.-H. Zhang *et al.*, "Improving gas sensing properties of graphene by introducing dopants and defects: a first-principles study.," *Nanotechnology*, vol. 20, no. 18, p. 185504, 2009.

[80] H. Terrones, R. Lv, M. Terrones, and M. S. Dresselhaus, "The role of defects and doping in 2D graphene sheets and 1D nanoribbons," *Reports Prog. Phys.*, vol. 75, no.

6, p. 062501, 2012.

[81] H. Liu, Y. Liu, and D. Zhu, “Chemical doping of graphene,” *J. Mater. Chem.*, vol. 21, no. 10, p. 3335, 2011.

[82] G. Ko, H. Y. Kim, J. Ahn, Y. M. Park, K. Y. Lee, and J. Kim, “Graphene-based nitrogen dioxide gas sensors,” *Curr. Appl. Phys.*, vol. 10, no. 4, pp. 1002–1004, 2010.

[83] M. G. Chung *et al.*, “Highly sensitive NO2 gas sensor based on ozone treated graphene,” *Sensors Actuators B Chem.*, vol. 166–167, no. 2, pp. 172–176, 2012.

[84] R. Pearce, T. Iakimov, M. Andersson, L. Hultman, A. L. Spetz, and R. Yakimova, “Epitaxially grown graphene based gas sensors for ultra sensitive NO 2 detection,” *Sensors Actuators, B Chem.*, vol. 155, no. 2, pp. 451–455, 2011.

[85] S. Ijima, “Helical Microtubules of Helical Carbon,” *Nature*, vol. 350, pp. 627–628, 1991.

[86] J. Kong *et al.*, “Nanotube molecular wires as chemical sensors,” *Science (80-.).*, vol. 287, no. 5453, pp. 622–625, 2000.

[87] I. Sayago *et al.*, “Carbon nanotube networks as gas sensors for NO2 detection,” *Talanta*, vol. 77, no. 2, pp. 758–764, 2008.

[88] S. Tans, A. Verschueren, and C. Dekker, “Room-temperature transistor based on a single carbon nanotube,” *Nature*, vol. 672, no. 1989, pp. 669–672, 1998.

[89] J.-W. Han, B. Kim, J. Li, and M. Meyyappan, “A carbon nanotube based ammonia sensor on cellulose paper,” *RSC Adv.*, vol. 4, no. 2, p. 549, 2014.

[90] R. C. Mani *et al.*, “Nanocrystalline graphite for electrochemical sensing,” *J. Electrochem. Soc.*, vol. 152, no. 4, pp. E154–E159, 2005.

[91] A. Serra, A. Buccolieri, E. Filippo, and D. Manno, “Nanographite assembled films for sensitive NO 2 detection,” *Sensors Actuators, B Chem.*, vol. 161, no. 1, pp. 359–365, 2012.

[92] G. Lu, L. E. Ocola, and J. Chen, “Reduced graphene oxide for room-temperature gas sensors.,” *Nanotechnology*, vol. 20, no. 44, p. 445502, 2009.

[93] S. J. Fishlock, D. Grech, J. W. McBride, H. M. H. Chong, and S. H. Pu, “Mechanical characterisation of nanocrystalline graphite using micromechanical structures,”

Microelectron. Eng., vol. 159, pp. 184–189, 2016.

[94] P. G. Collins, “Extreme Oxygen Sensitivity of Electronic Properties Extreme Oxygen Sensitivity of Electronic Properties of Carbon Nanotubes,” *Science (80-.).*, vol. 1801, no. 2000, pp. 1801–1805, 2007.

[95] A. D. Smith *et al.*, “Resistive graphene humidity sensors with rapid and direct electrical readout,” *Nanoscale*, vol. 7, no. 45, pp. 19099–19109, 2015.

[96] M.-C. Chen, C.-L. Hsu, and T.-J. Hsueh, “Fabrication of Humidity Sensor Based on Bilayer Graphene,” *IEEE Electron Device Lett.*, vol. 35, no. 5, pp. 590–592, 2014.

[97] S. Ghosh, R. Ghosh, P. K. Guha, and T. K. Bhattacharyya, “Humidity Sensor Based on High Proton Conductivity of Graphene Oxide,” *IEEE Trans. Nanotechnol.*, vol. 14, no. 5, pp. 931–937, 2015.

[98] D. T. Phan, I. Park, A. R. Park, C. M. Park, and K. J. Jeon, “Black P/graphene hybrid: A fast response humidity sensor with good reversibility and stability,” *Sci. Rep.*, vol. 7, no. 1, pp. 1–7, 2017.

[99] K. P. Yoo, L. T. Lim, N. K. Min, M. J. Lee, C. J. Lee, and C. W. Park, “Novel resistive-type humidity sensor based on multiwall carbon nanotube/polyimide composite films,” *Sensors Actuators, B Chem.*, vol. 145, no. 1, pp. 120–125, 2010.

[100] T. Y. Ling *et al.*, “Sensing performance of Nanocrystalline Graphite Based Humidity Sensors,” *IEEE Sens. J.*, vol. PP, no. c, p. 1, 2019.

[101] H. Sadeghian *et al.*, “Surface contamination-induced resonance frequency shift of cantilevers,” *4th IEEE Int. Conf. Nano/Micro Eng. Mol. Syst. NEMS 2009*, pp. 400–403, 2009.

[102] E. Ollier *et al.*, “NEMS GAS SENSORS FOR BREAKTHROUGH GC MULTIGAS ANALYSIS SYSTEMS CEA , LETI , MINATEC Campus , F-38054 Grenoble FRANCE Univ . Grenoble Alpes , F-38000 Grenoble FRANCE APIX Analytics , F-38054 Grenoble FRANCE,” pp. 1440–1443, 2015.

[103] J. J. Whiting *et al.*, “HIGH-SPEED TWO-DIMENSIONAL GAS CHROMATOGRAPHY USING MICROFABRICATED GC COLUMNS COMBINED WITH NANOELECTROMECHANICAL MASS SENSORS Sandia National Laboratories , Albuquerque , NM , USA Department of Applied Physics ,

California Institute of Technology , Pasa," *Signals*, pp. 1666–1669, 2009.

[104] C.-Y. Lee and G.-B. Lee, "Micromachine-based humidity sensors with integrated temperature sensors for signal drift compensation," *J. Micromechanics Microengineering*, vol. 13, no. 5, p. 620, 2003.

[105] N. Lazarus, S. Bedair, C. Lo, and G. Fedderl, "Lazarus, Lo3 Fedderl," pp. 268–271, 2009.

[106] Z. Huanhuan, Z. Zhan, D. Haifeng, F. Zhen, and G. Peng, "Fabrication and test of MEMS/NEMS based polyimide integrated humidity, temperature and pressure sensor," *Proc. 1st IEEE Int. Conf. Nano Micro Eng. Mol. Syst. 1st IEEE-NEMS*, pp. 788–791, 2006.

[107] H. Ooe, T. Eimori, M. Nomura, H. Nishikawa, K. Fujimoto, and T. Hasegawa, "Low drift MEMS humidity sensor by intermittent heating," *IMFEDK 2015 - 2015 Int. Meet. Futur. Electron Devices, Kansai*, pp. 118–119, 2015.

[108] W. Wen, H. Shitang, L. Shunzhou, L. Minghua, and P. Yong, "Enhanced sensitivity of SAW gas sensor coated molecularly imprinted polymer incorporating high frequency stability oscillator," *Sensors Actuators, B Chem.*, vol. 125, no. 2, pp. 422–427, 2007.

[109] Y. Roh, Y. Lee, and H. Kim, "Development of a SAW microgas sensor for monitoring SO2 gas," *J. Acoust. Soc. Am.*, vol. 108, p. 2599, 2000.

[110] M. Zhang, L. Du, Z. Fang, and Z. Zhao, "A Sensitivity-Enhanced Film Bulk Acoustic Resonator Gas Sensor with an Oscillator Circuit and Its Detection Application," *Micromachines*, vol. 8, no. 1, p. 25, 2017.

[111] D. Chen, Y. Xu, J. Wang, and L. Zhang, "Nerve gas sensor using film bulk acoustic resonator modified with a self-assembled Cu2+/11-mercaptoundecanoic acid bilayer," *Sensors Actuators, B Chem.*, vol. 150, no. 1, pp. 483–486, 2010.

[112] J. Hodgkinson and R. P. Tatam, "Optical gas sensing: a review," *Meas. Sci. Technol.*, vol. 24, no. 1, p. 012004, 2013.

[113] L. S. Rothman *et al.*, "The HITRAN2012 molecular spectroscopic database," *J. Quant. Spectrosc. Radiat. Transf.*, vol. 130, pp. 4–50, 2013.

[114] H. Edner, P. Ragnarson, S. Spännare, and S. Svanberg, "Differential optical

absorption spectroscopy (DOAS) system for urban atmospheric pollution monitoring.," *Appl. Opt.*, vol. 32, no. 3, pp. 327–33, 1993.

[115] G. Somesfalean, J. Alnis, U. Gustafsson, H. Edner, and S. Svanberg, "Long-path monitoring of NO2 with a 635 nm diode laser using frequency-modulation spectroscopy.," *Appl. Opt.*, vol. 44, no. 24, pp. 5148–51, 2005.

[116] F. Xu, Z. Lv, X. Lou, Y. Zhang, and Z. Zhang, "Nitrogen dioxide monitoring using a blue LED.," *Appl. Opt.*, vol. 47, no. 29, pp. 5337–5340, 2008.

[117] Y. Yang, Z. Gao, D. Zhong, and W. Lin, "Detection of nitrogen dioxide using an external modulation diode laser," *Appl. Opt.*, vol. 52, no. 13, pp. 3027–3030, 2013.

[118] J. M. Langridge, S. M. Ball, A. J. L. Shillings, and R. L. Jones, "A broadband absorption spectrometer using light emitting diodes for ultrasensitive, in situ trace gas detection," *Rev. Sci. Instrum.*, vol. 79, no. 12, 2008.

[119] J. Sun, M. E. Schmidt, M. Muruganathan, H. M. H. Chong, and H. Mizuta, "Large-scale nanoelectromechanical switches based on directly deposited nanocrystalline graphene on insulating substrates," *Nanoscale*, vol. 8, no. 12, pp. 6659–6665, 2016.

[120] J. A. Thornton, "The microstructure of sputter-deposited coatings," *J. Vac. Sci. Technol. A Vacuum, Surfaces, Film.*, vol. 4, no. 6, p. 3059, 1986.

[121] J. A. Thornton, "The microstructure of sputter-deposited coatings," *J. Vac. Sci. Technol. A Vacuum, Surfaces, Film.*, vol. 4, no. 6, p. 3059, 1986.

[122] M. Suemitsu, Y. Miyamoto, H. Handa, and A. Konno, "Graphene Formation on a 3C-SiC(111) Thin Film Grown on Si(110) Substrate," *e-Journal Surf. Sci. Nanotechnol.*, vol. 7, no. April, pp. 311–313, 2009.

[123] M. G. Mynbaeva, A. A. Lavrent'ev, and K. D. Mynbaev, "Formation of graphite/sic structures by the thermal decomposition of silicon carbide," *Semiconductors*, vol. 50, no. 1, pp. 138–142, 2016.

[124] T. Ohta, N. C. Bartelt, S. Nie, K. Thürmer, and G. L. Kellogg, "Role of carbon surface diffusion on the growth of epitaxial graphene on SiC," *Phys. Rev. B - Condens. Matter Mater. Phys.*, vol. 81, no. 12, 2010.

[125] S. Goler *et al.*, "Revealing the atomic structure of the buffer layer between SiC(0 0 0 1) and epitaxial graphene," *Carbon N. Y.*, vol. 51, no. 1, pp. 249–254, 2013.

[126] H. Yuji *et al.*, “Mg x Zn 1-x O epitaxial films grown on ZnO substrates by molecular beam epitaxy,” no. 68950, p. 68950D, 2008.

[127] S. K. Jerng *et al.*, “Nanocrystalline graphite growth on sapphire by carbon molecular beam epitaxy,” *J. Phys. Chem. C*, vol. 115, no. 11, pp. 4491–4494, 2011.

[128] T. Schumann *et al.*, “Structural investigation of nanocrystalline graphene grown on (6√ 3 × 6√ 3)R30°-reconstructed SiC surfaces by molecular beam epitaxy,” *New J. Phys.*, vol. 15, no. 0001, pp. 0–16, 2013.

[129] G. Lippert *et al.*, “Molecular beam growth of micrometer-size graphene on mica,” *Carbon N. Y.*, vol. 52, pp. 40–48, 2013.

[130] G. Lippert *et al.*, “Molecular beam growth of micrometer-size graphene on mica,” *Carbon N. Y.*, vol. 52, pp. 40–48, 2013.

[131] U. Wurstbauer *et al.*, “Molecular beam growth of graphene nanocrystals on dielectric substrates,” *Carbon N. Y.*, vol. 50, no. 13, pp. 4822–4829, 2012.

[132] L. Company, B. William, and R. E. Offeman, “Preparation of Graphitic Oxide,” vol. 89, no. 9, p. 1958, 1958.

[133] S. Lee, S. Hun, J. Suk, and S. Hyun, “Large-scale production of high-quality reduced graphene oxide,” *Chem. Eng. J.*, vol. 233, pp. 297–304, 2013.

[134] G. E. McGuire, *Semiconductor Materials and Process Technology Handbook: For Very Large Scale Integration (VLSI) and Ultra Large Scale Integration (ULSI)*. Noyes Publications, 1988.

[135] W. Yang *et al.*, “Growth, characterization, and properties of nanographene,” *Small*, vol. 8, no. 9, pp. 1429–1435, 2012.

[136] V. P. Pham, “Direct Growth of Graphene on Flexible Substrates toward Flexible Electronics: A Promising Perspective,” *Flex. Electron.*, 2018.

[137] S. Hofmann, C. Ducati, J. Robertson, and B. Kleinsorge, “Low-temperature growth of carbon nanotubes by plasma-enhanced chemical vapor deposition,” *Appl. Phys. Lett.*, vol. 83, no. 1, pp. 135–137, 2003.

[138] S. Xing, W. Wu, Y. Wang, J. Bao, and S. S. Pei, “Kinetic study of graphene growth: Temperature perspective on growth rate and film thickness by chemical vapor

deposition," *Chem. Phys. Lett.*, vol. 580, pp. 62–66, 2013.

[139] C. Ducati, I. Alexandrou, M. Chhowalla, G. A. J. Amaratunga, and J. Robertson, "Temperature selective growth of carbon nanotubes by chemical vapor deposition," *J. Appl. Phys.*, vol. 92, no. 6, pp. 3299–3303, 2002.

[140] "The diffusion coefficient of interstitial carbon in silicon," *Semicond. Sci. Technol.*, vol. 2, no. 5, pp. 315–317, 1987.

[141] J. Chu, X. Peng, P. Feng, Y. Sheng, and J. Zhang, "Study of humidity sensors based on nanostructured carbon films produced by physical vapor deposition," *Sensors Actuators, B Chem.*, vol. 178, pp. 508–513, 2013.

[142] J. Han, B. Kim, J. Li, and M. Meyyappan, "RSC Advances A carbon nanotube based ammonia sensor on cellulose paper," pp. 549–553, 2014.

[143] S. N. Magonov, V. Elings, and M. H. Whangbo, "Phase imaging and stiffness in tapping-mode atomic force microscopy," *Surface Science*, vol. 375, no. 2–3. 1997.

[144] M. E. Schmidt, "Plasma enhanced chemical vapor deposition of nanocrystalline graphene and device fabrication development," 2012.

[145] S. Rana *et al.*, "Nano-crystalline graphite for reliability improvement in MEM relay contacts," *Carbon N. Y.*, vol. 133, pp. 193–199, 2018.

[146] A. C. Ferrari and J. Robertson, "Raman spectroscopy of amorphous, nanostructured, diamond-like carbon, and nanodiamond.," *Philos. Trans. A. Math. Phys. Eng. Sci.*, vol. 362, no. 1824, pp. 2477–2512, 2004.

[147] L. Hultman and Z. Czigany, "Interpretation of electron diffraction patterns from amorphous and fullerene-like carbon allotropes," *Ultramicroscopy*, vol. 110, no. 110, pp. 815–819, 2010.

[148] R. Matassa *et al.*, "Characterization of carbon structures produced by graphene self-assembly," *J. Appl. Crystallogr.*, vol. 47, no. 1, pp. 222–227, 2014.

[149] K. Jurkiewicz, M. Pawlyta, and A. Burian, "Structure of Carbon Materials Explored by Local Transmission Electron Microscopy and Global Powder Diffraction Probes," *C*, vol. 4, no. 4, p. 68, 2018.

[150] I. M. Alloy and I. P. Calculated, "Crystallographic parameters Subfiles and Quality

Peak list," vol. 4, pp. 9–10, 2017.

[151] C. Y. Chen, P. H. Chang, K. T. Tsai, and J. H. He, "Electrical and optoelectronic characterization of a ZnO nanowire contacted by focused-ion-beam-deposited Pt," *INEC 2010 - 2010 3rd Int. Nanoelectron. Conf. Proc.*, pp. 1177–1178, 2010.

[152] Z. Zhang *et al.*, "Study on adsorption and desorption of ammonia on graphene," *Nanoscale Res. Lett.*, 2015.

[153] I. Langmuir, "the Adsorption of Gases on Plane Surfaces of," *J. Am. Chem. Soc.*, vol. 40, no. 9, pp. 1361–1403, 1918.

[154] Y. Miyajima, J. M. Shannon, S. J. Henley, V. Stolojan, D. C. Cox, and S. R. P. Silva, "Electrical conduction mechanism in laser deposited amorphous carbon," *Thin Solid Films*, vol. 516, no. 2–4, pp. 257–261, 2007.

[155] M. Ieda, G. Sawa, and S. Kato, "A consideration of Poole-Frenkel effect on electric conduction in insulators," *J. Appl. Phys.*, vol. 42, no. 10, pp. 3737–3740, 1971.

[156] W. Kulisch, C. Popov, E. Lefterova, S. Bliznakov, J. P. Reithmaier, and F. Rossi, "Electrical properties of ultrananocrystalline diamond/amorphous carbon nanocomposite films," *Diam. Relat. Mater.*, vol. 19, no. 5–6, pp. 449–452, 2010.

[157] S. J. Fishlock *et al.*, "Micromachined nanocrystalline graphite membranes for gas separation," *Carbon N. Y.*, vol. 138, no. June, pp. 125–133, 2018.

[158] O. Leenaerts, B. Partoens, and F. M. Peeters, "Adsorption of H2 O, N H3, CO, N O2, and NO on graphene: A first-principles study," *Phys. Rev. B - Condens. Matter Mater. Phys.*, vol. 77, no. 12, pp. 1–6, 2008.

[159] R. Fogelholm and G. Grimvall, "Conducting properties of two-phase materials," *J. Phys. C Solid State Phys.*, vol. 16, no. 6, pp. 1077–1084, 1983.

[160] M. Lu and R. G. Compton, "Voltammetric pH sensor based on an edge plane pyrolytic graphite electrode," *Analyst*, vol. 139, no. 10, pp. 2397–2403, 2014.

[161] F. E. Galdino *et al.*, "Graphite Screen-Printed Electrodes Applied for the Accurate and Reagentless Sensing of pH," *Anal. Chem.*, vol. 87, no. 23, pp. 11666–11672, 2015.

[162] M. Hadi, A. Rouhollahi, and M. Yousefi, "Nanocrystalline graphite-like pyrolytic

carbon film electrode for electrochemical sensing of hydrazine," *Sensors Actuators, B Chem.*, vol. 160, no. 1, pp. 121–128, 2011.

[163] M. Wissler, "Graphite and carbon powders for electrochemical applications," *J. Power Sources*, vol. 156, no. 2, pp. 142–150, 2006.

[164] M. Zhou, Y. Zhai, and S. Dong, "Electrochemical Sensing and Biosensing Platform Based on Chemically Reduced Graphene Oxide Supporting Information (SI)," *Anal. Chem.*, vol. 81, no. 14, pp. 5603–5613, 2009.

Bibliography

S. Franssila, Introduction to Microfabrication, 2nd Ed., Wiley, 2010

D. K. Schroder, Semiconductor Material and Device Characterization, 2nd Ed., Wiley, 1998.

M. J. Madou, Fundamentals of Microfabrication, 2nd Ed., Taylor and Francis, 1997.